This is to certify that the

thesis entitled

The Design and Testing of a Compact Electron Cyclotron Resonant Microwave-Cavity Ion Source

presented by

Leonard Joseph Mahoney

has been accepted towards fulfillment of the requirements for

Master's degree in Elec Engr

Major professor

Date 6/23/89

THE DESIGN AND TESTING
OF A COMPACT ELECTRON CYCLOTRON RESONANT
MICROWAVE-CAVITY ION SOURCE

By

LEONARD JOSEPH MAHONEY

A THESIS

Submitted to
Michigan State University
in partial fulfillment of the requirements
for the degree of

MASTER OF SCIENCE

Department of Electrical Engineering

1989

THE

Many

comp

This

micro

than

dens

area.

2000

diffu

propo

The

that

life

ABSTRACT

THE DESIGN AND TESTING OF A COMPACT ELECTRON CYCLOTRON RESONANT MICROWAVE-CAVITY ION SOURCE

By

LEONARD JOSEPH MAHONEY

Many scientific and industrial activities require a long-life, compact, ion source that can work in both inert and reactive gases. This thesis reviews the design and testing of a compact, ECR microwave-cavity ion source that operates at 2.45 GHz and with less than 200 Watts of input power. The ion source can produce ion current densities in excess of 10mA/cm^2 over a 3.2 cm diameter extraction area. Focused broad-beams currents of 40 mA at energies of 1000 to 2000 eV can be extracted in argon, oxygen and nitrogen. Simple plasma diffusion models are used to understand and predict the scaling properties of the ECR discharge and to predict ion source performance. The study culminates in a refined microwave-cavity ion source design that is simple, compact, reliable, and that has a long working life time.

This Thesis is dedicated to

Edward C. and Dorothy Mahoney

and

Man

C. B

the

Brac

Elec

Mich

ACKNOWLEDGEMENTS

The Author would like to thank Dr. Jes Asmussen Jr. for his council and guidance throughout this study. Additional thanks is given to Dr. Mahmoud Dahimene for his early guidance and encouragement and to Mr. C. Benjamin Boyle, Dr. Stanley Whitehair and Mr. Jeffrey Hopwood for their support and friendship. Special thanks is given to Miss Carol Bracewell for her endearing love and support.

This research was supported in part by grants from Optic Electronics Corporation of Texas and Wavemat Corporation of Plymouth, Michigan.

TABLE OF CONTENTS

LIST OF TABLES viii

LIST OF FIGURES ix

CHAPTER 1 INTRODUCTION

1.1 THE ECR MICROWAVE ION SOURCE 1

1.2 RESEARCH 4

1.3 RESEARCH OBJECTIVES 5

1.4 THESIS OUTLINE 6

CHAPTER 2 EARLY EXPERIMENTS WITH THE FIRST PROTOTYPE COMPACT MICROWAVE-CAVITY ION SOURCE

2.1 INTRODUCTION 7

2.2 COMPACT MICROWAVE-CAVITY ION SOURCE: PROTOTYPE I 8

2.3 GENERAL EXPERIMENTAL SYSTEMS

2.3.1 LOW PRESSURE VACUUM AND GAS FEED SYSTEMS 13

2.3.2 MICROWAVE POWER SYSTEMS 15

2.3.3 LANGMUIR PROBE MEASUREMENTS AND TECHNIQUES

2.3.3.1 LANGMUIR PROBE AND CIRCUIT 17

2.3.3.2 CALCULATION OF ELECTRON DENSITY AND TEMPERATURE WITH LANGMUIR PROBE I-V READINGS 19

2.3.3.3 INTERPRETATION OF LANGMUIR PROBE READINGS ... 23

2.3.4 ION EXTRACTION OPTICS AND ASSEMBLIES

2.3.4.1 DOUBLE-GRID EXTRACTION ASSEMBLY AND CIRCUIT 24

2.3.4.2 SINGLE-GRID EXTRACTION ASSEMBLIES AND CIRCUIT 28

2.4 OPERATION AND PERFORMANCE OF THE COMPACT MICROWAVE-CAVITY ION SOURCE PROTOTYPE

2.4.1 OPERATION OF THE ION SOURCE: PROTOTYPE I 30

2.4.2 LANGMUIR PROBE MEASUREMENTS 38

2.4.3 DOUBLE-GRID BEAM EXTRACTION EXPERIMENTS 47

2.4.4 SINGLE-GRID EXTRACTION 64

2.5 SUMMARY OF THE MICROWAVE-CAVITY ION SOURCE PERFORMANCE: PROTOTYPE I 65

CHAPTER 3 SIMPLE PLASMA DIFFUSION MODELS

3.1 INTRODUCTION 68

3.2 DIFFUSION MODELS

3.2.1 SCHOTTKY AND FREE-FALL DIFFUSION 69

3.2.2 PHYSICAL ASSUMPTIONS 70

3.2.3 SCHOTTKY DIFFUSION MODEL 70

3.2.4 FREE-FALL DIFFUSION 78

3.3 IONIZATION POWER AND DIFFUSION MODELING

3.3.1 INTRODUCTION 83

3.3.2 POWER ABSORPTION 84

3.3.3 POWER LOSS 87

3.3.4 POWER REQUIRED IN A COMPACT ION SOURCE DISCHARGE ... 92

CH

4.

4.

4.

4.

CHAPT

5.

5.

CHAPTER 4 A REFINED COMPACT ECR MICROWAVE-CAVITY ION SOURCE: PROTOTYPE II

4.1 INTRODUCTION 104

4.2 DESIGN OF A REFINED MICROWAVE-CAVITY ION SOURCE: PROTOTYPE II

4.2.1 COMPACT MICROWAVE-CAVITY ION SOURCE 105

4.2.2 MICROWAVE DESIGN ASPECTS

4.2.2.1 MICROWAVE CAVITY DIMENSIONS 110

4.2.2.2 COAXIAL INPUT LINE 118

4.2.2.3 RADIAL CHOKES 118

4.2.3 MAGNET CONFIGURATION 121

4.2.4 QUARTZ CAP AND SEALING 123

4.2.5 COOLING 123

4.2.6 OPERATION OF REFINED ION SOURCE PROTOTYPE 124

4.3 LANGMUIR PROBE EXPERIMENTS 125

4.4 ION BEAM EXTRACTION

4.4.1 FARADAY CUP ARRAY 133

4.4.2 DOUBLE-GRID ION BEAM EXTRACTION EXPERIMENTS WITH PROTOTYPE II 136

4.4.3 DESIGN CONSIDERATIONS FOR EXTRACTION OPTICS 147

CHAPTER 5 SUMMARY AND CONCLUSIONS

5.1 SUMMARY OF ION SOURCE PERFORMANCE 152

5.2 FUTURE RESEARCH 153

LIST OF TABLES

TABLE 2-I. SHORT AND PROBE LENGTHS FOR STANDARD MODES IN COMPACT MICROWAVE ION SOURCE PROTOTYPE 33

TABLE 2-II. SHORT AND PROBE LENGTHS FOR STANDARD MODES IN COMPACT MICROWAVE ION SOURCE PROTOTYPE: IGNITION AND TUNED OPERATION 35

TABLE 4-I. SHORT AND PROBE LENGTHS FOR THE TE_{111} OPERATING MODE IN THE COMPACT MICROWAVE ION SOURCE, PROTOTYPE II ... 126

TABL

TABL

TABL

LIST OF TABLES

TABLE 2-I. SHORT AND PROBE LENGTHS FOR STANDARD MODES IN COMPACT MICROWAVE ION SOURCE PROTOTYPE 33

TABLE 2-II. SHORT AND PROBE LENGTHS FOR STANDARD MODES IN COMPACT MICROWAVE ION SOURCE PROTOTYPE: IGNITION AND TUNED OPERATION 35

TABLE 4-I. SHORT AND PROBE LENGTHS FOR THE TE_{111} OPERATING MODE IN THE COMPACT MICROWAVE ION SOURCE, PROTOTYPE II ... 126

LIST OF FIGURES

Figure 1.1 The ECR microwave-cavity ion source concept.............2

Figure 2.1 Microwave-Cavity Ion Source: Prototype I................10
Figure 2.2 Detail of Microwave-Cavity Ion Source Discharge Region..12
Figure 2.3 Pumping System..14
Figure 2.4 Microwave Power Circuit.................................16
Figure 2.5 Double Langmuir Probe...................................18
Figure 2.6 Position of Double Langmuir Probe.......................18
Figure 2.7 Typical I-V Characteristics and Analysis................20
Figure 2.8 Double-Grid Extraction Optics...........................25
Figure 2.9 Double-Grid Extraction Circuit..........................27
Figure 2.10 Silicon-Grid Extraction Optics.........................29
Figure 2.11 Screen-Grid Extraction Optics..........................31
Figure 2.12 Electromagnetic Fields of the TE_{111} Mode................36
Figure 2.13 Vacuum Pressure versus Flow for Argon..................39
Figure 2.14 Electron Density versus Discharge Pressure - No Magnets..41
Figure 2.15 Four-Pole Samarium-Cobalt Magnet Configuration.........42
Figure 2.16 Electron Density versus Discharge Pressure - With and Without Magnets..............................44
Figure 2.17 Electron Density versus Discharge Pressure for Two Discharge Heights.................................45

Figure 2.18 Electron Density versus Discharge Pressure for Various Input Powers....................................46
Figure 2.19 Total Beam Current versus Power for Argon - Four-Pole Magnet Configuration..........................49
Figure 2.20 Total Beam Current versus Power for Oxygen - Four-Pole Magnet Configuration..........................50
Figure 2.21 Total Beam Current versus Extraction Potential for Argon - Four-Pole Magnet Configuration..................51
Figure 2.22 Total Beam Current versus Extraction Potential for Oxygen - Four-Pole Magnet Configuration.................52
Figure 2.23 Total Beam Current versus Argon Input Flow - Four-Pole Magnet Configuration..........................53
Figure 2.24 Total Beam Current versus Oxygen Input Flow - Four-Pole Magnet Configuration..........................54
Figure 2.25 ECR Zones for a Ten-Pole Neodymium-Iron-Boron Magnet Configuration...................................56
Figure 2.26 Total Beam Current versus Power for Argon - Ten-Pole Magnet Configuration...........................57
Figure 2.27 Total Beam Current versus Extraction Potential for Argon - Ten-Pole Magnet Configuration..................58
Figure 2.28 Total Beam Current versus Argon Input Flow - Ten-Pole Magnet Configuration...........................59
Figure 2.29 Total Beam Current versus Oxygen Input Flow - Ten-Pole Magnet Configuration...........................60
Figure 2.30 Total Beam Current versus Power for Nitrogen - Ten-Pole Magnet Configuration...........................61
Figure 2.31 Total Beam Current versus Nitrogen Input Flow - Ten-Pole Magnet Configuration...........................62
Figure 2.32 Power Cost versus Input Power for Nitrogen - Ten-Pole Magnet Configuration...........................66

Figu
Figu
Figu
Figu
Figu
Figu
Figu
Figu
Figu
Figu
Figur
Figur
Figur
Figur
Figur
Figur-
Figur-
Figur-

Figure 3.1 Total Collision Cross-Section versus Electron Energy for Argon 76
Figure 3.2 Universal Schottky Diffusion Curve for Argon....77
Figure 3.3 Universal Free-Fall Diffusion Curve for Argon....81
Figure 3.4 Superposition of Schottky and Free-Fall Diffusion Curves....82
Figure 3.5 Energy Transport Paths in a Discharge....85
Figure 3.6 Ionization Power versus Pressure for Schottky Diffusion....93
Figure 3.7 Ionization Power versus Pressure for Free-Fall Diffusion....94
Figure 3.8 Ionization Power Density versus Pressure for Schottky Diffusion....95
Figure 3.9 Ionization Power Density versus Pressure for Free-Fall Diffusion....96
Figure 3.10 Ionization Power versus Pressure for a 2.5 cm Diameter x 6 cm High Discharge....97
Figure 3.11 Electron Temperature versus Pressure for a 2.5 cm Diameter x 6 cm High Discharge....98
Figure 3.12 Ionization Power versus Discharge Height for Free-Fall Diffusion....101
Figure 3.13 Ionization Power versus Discharge Height for Schottky Diffusion....102
Figure 3.14 Ionization Power Density versus Discharge Height for Free-Fall Diffusion....103

Figure 4.1 ECR Microwave-cavity Ion Source: Prototype II, Side View 106
Figure 4.2 ECR Microwave-cavity Ion Source: Prototype II, Top View....106
Figure 4.3 Prototype II, Detail of the Discharge Region....108

ig
ig
igu
igu
igu
igu
igu
igu
igu
igu
igu
igur
igur
igur
igur
igur
igur
igure
igure
igure
igure
igure
gure

Figure 4.4 Stainless Steel Base Plate with Eight Magnets..........111
Figure 4.5 Brass Cap for Magnets, Silicone O-ring, and Quartz Cap..........112
Figure 4.6 Base Plate Assembly..........113
Figure 4.7 Brass Cavity, Input Probe/Antenna, and Sliding Short...114
Figure 4.8 Microwave-cavity Assembly..........115
Figure 4.9 Assembly of the Microwave-cavity Ion Source: Prototype II..........116
Figure 4.10 Theoretical Cavity Length versus Cavity Radius for the TE_{111} Mode at 2.45 GHz..........117
Figure 4.11 Modeling of the Radial Choke on the Coaxial Transmission Line..........120
Figure 4.12 Orientation of the Static Magnetic Field with the Microwave Input Probe..........122
Figure 4.13 Electron Density versus Discharge Pressure for Argon...128
Figure 4.14 Electron Density versus Power for Various Argon Gas Flows..........129
Figure 4.15 Free-fall Diffusion Curve for Prototypes I and II......131
Figure 4.16 Schottky and Free-fall Diffusion Curves for Ion Source Prototypes I and II..........132
Figure 4.17 Sixteen Channel Faraday Cup Array..........134
Figure 4.18 Faraday Cup Circuit and Profile Monitoring System......135
Figure 4.19 Total Beam Current versus Input Power for Argon........137
Figure 4.20 Total Beam Current versus Extraction Potential for Argon..........138
Figure 4.21 Total Beam Current versus Argon Input Gas Flow.........139
Figure 4.22 Ion Beam Current Density Profiles for Argon............140
Figure 4.23 Total Beam Current versus Extraction Potential for Oxygen..........142
Figure 4.24 Beam Current Density Profiles for Oxygen...............143
Figure 4.25 Total Beam Current versus Oxygen Input Gas Flow........144
Figure 4.26 Total Beam Current versus Power for Oxygen............145

Fig

Fig

Fig

Figure 4.27 Beam Current Density Profiles for Oxygen
with Two Acceleration Potentials.......................146

Figure 4.28 Total Beam Current versus Power for Nitrogen...........148

Figure 4.29 Total beam Current versus Nitrogen Input Gas Flow......149

1.1

micr

inte

Uni

tech

prop

show

req

nsi

isc

icr

rod

mt

E

cm

int

CHAPTER I

INTRODUCTION

1.1 THE ECR MICROWAVE ION SOURCE

The development of electron cyclotron resonant (ECR) microwave-cavity plasma and ion sources has been the subject of intense study for the last five years at Michigan State University.[1-25] Among many applications of this microwave plasma technology is the generation of broad ion beams for electric space propulsion[4,8] and for materials processing.[12-14,20-29] Figure 1.1 shows an ECR microwave-cavity ion source. Microwaves at a single frequency are input into a single-mode, resonant cavity structure. Inside the cavity is a quartz-contained, disk-shaped, low-pressure discharge which is excited by the high electric fields of the microwaves. A series of permanent magnets alternating in polarity produce a multicusp magnetic field in the discharge region. The combination of microwaves and static magnetic fields produce regions of ECR heating within the discharge. It is these ECR regions that promote efficient power coupling to the electron sub-gas and help maintain a well-ionized discharge at low pressures.

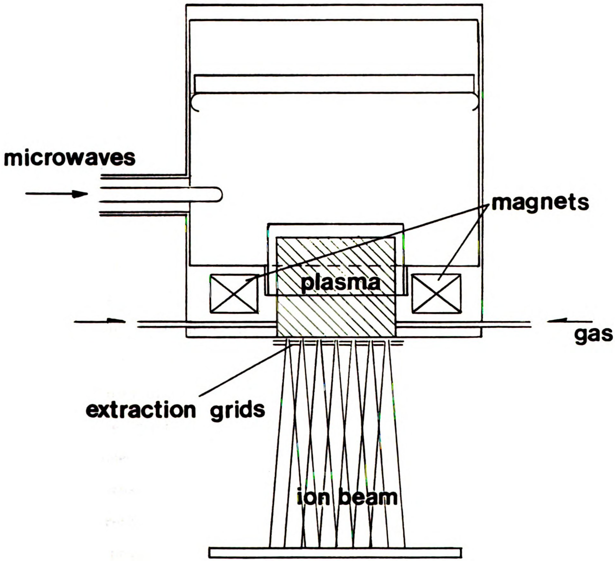

Figure 1.1 The ECR microwave-cavity ion source concept.

di

de

ele

EC

has

and

bro

ion

mic

and

sou

inve

plas

extr

leve

com

diam

dev

des

curr

ion

bear

conv

With the addition of extraction grids at the base of the discharge, the microwave discharge becomes a broad-beam ion source, a device that has a number of applications in materials processing, electric space propulsion, and fusion heating. The advantage of the ECR microwave-cavity ion source is that it has no electrodes and thus has a long lifetime in inert and reactive gases. In many scientific and industrial applications, such as surface modification and broad-beam sputtering, an efficient, compact, long-life, electrodeless ion source is highly desirable.

This thesis describes the design and testing of a compact, ECR microwave-cavity ion source. The studies focus on reducing the size and improving the efficiency of a basic ECR microwave plasma ion source which has been the subject of many other recent investigations.[11,14,23,24] The intention is to demonstrate that this plasma source design can be adapted to single- and multiple-grid ion extraction optics and can generate broad ion beams with moderate levels of microwave input power.

A first ion source prototype demonstrates that an efficient compact discharge of 5 cm in diameter can be used to produce a 3.2 cm diameter ion beam.[19] A second prototype is developed to improve device operation and to further compact the ion source design. Both designs are successful in producing argon, oxygen, and nitrogen ion current densities in excess of 10 mA/cm^2 at the base of the discharge. ion beams are extracted with ion acceleration optics. Extracted ion beam densities meet or exceed beam current densities generated by conventional DC ion sources of the same scale.

st

po

dis

dis

sim

pu

tha

Thi

and

scie

scie

1.2

ove

yea

dire

Elec

des

M.

Rog

Whi

In addition to experimental work, discharge diffusion models are studied to investigate charged-particle distribution, ionization power, and general scaling properties of cylindrically-shaped discharges. Although many assumptions are made to simplify the discharge model, a comparison of experimental data with these simplified diffusion models yields information for ion source design purposes.

This thesis reviews the experimental and theoretical investigations that have resulted in a compact, efficient, and simple ion source. This device can be re-configured and applied to a number of industrial and scientific activities. Parts of this work have been published in scientific journals,[19,22] and presented at several international scientific conferences.[15,17,18,20,22]

1.2 RESEARCH

The research presented in this thesis was performed by the author over a period of one and one half years as an undergraduate and two years as a graduate student at Michigan State University under the direction of Dr. Jes Asmussen, Professor in the Department of Electrical Engineering in the College of Engineering. The studies and designs presented herein build upon research work carried out by Dr. M. Dahimene,[2,9-11] Dr. T. Roppel,[28,29] J. Root,[1,3-5] Dr. J. Rogers,[30] Dr. R. Mallavarpu,[31] Dr. R. Fredericks,[32] and Dr. S. Whitehair.[33]

1.

de

ma

pr

de

in-

to

pr

etc

cor

per

and

1.4.

C

pre

use

revi

for

are

Ion

to o

futu

1.3 RESEARCH OBJECTIVES

There are three objectives to this thesis. The first is to determine if a compact, 5 cm diameter discharge can be easily maintained with modest amounts of input power, < 200 Watts, and can produce high beam current densities. The second objective is to design a long-life, compact, microwave-cavity ion source which is inexpensive, reliable, and simple to operate. The third objective is to investigate and develop theoretical diffusion models which can predict the behavior (i.e. density, charged-particle distribution, etc.), of ECR microwave-cavity ion sources of varying scale. In consideration of these objectives a number of experiments are performed including Langmuir probe measurements of electron density and temperature, beam extraction, and beam profile measurements.

1.4. THESIS OUTLINE

Chapter II of this thesis reviews the design and testing of a preliminary prototype ion source including sub-systems and experiments used to study its performance as a broad beam ion source. Chapter III reviews the development of Schottky and Free-Fall diffusion theories for a disk-shaped, low-pressure discharge. Universal diffusion curves are described and tested against measured electron temperatures. Ionization power is investigated and used to estimate power required to operate the ion source and establish general scaling guidelines for future designs. Chapter IV reviews the design of a second prototype ior

su

ion source and its performance. Chapter V concludes the thesis with a summary of the work and recommendations for future study.

CHAPTER 2

EARLY EXPERIMENTS WITH THE FIRST PROTOTYPE COMPACT MICROWAVE-CAVITY ION SOURCE

2.1 INTRODUCTION

In early experiments by Dahimene,[9] a 30 mA, 1000 V, 3.2 cm diameter, argon ion beam was extracted from an ECR microwave-cavity ion source. The microwave power required to achieve this was 250 Watts. A figure of merit used to evaluate the performance of ion sources is the power cost factor. For microwave ion sources this is

$$\text{Power Cost} = \frac{\text{Microwave Power into Ion Source}}{\text{Beam Amperes Delivered}} \quad . \qquad (2.1)$$

In Dahimene's 9.4 cm diameter, 1 mTorr discharge, this cost was 8333 Watts/Beam Ampere. In certain applications, such as broad-beam sputtering, an argon or oxygen beam current greater than 40 mA from a 3.2 cm diameter extraction grid is desired. A significant amount of microwave power is required and thus high power and costly magnetron supplies are necessary to drive such ion sources. It is desirable to reduce the power cost factor, reduce the total system weight and size, and to simplify the operation of the technology.

One of the reasons for the high power cost reported by Dahimene is

that a
plasma
base o
by eit
or by
thesis
diamete
power

This
microw
densiti
with ex
probe e
ion bea
Compare
increase
extractio
available
less than
diameter
improvem

2.2 CC

The b
microwa

that a 3.2 cm diameter beam was being extracted from a 9.4 cm diameter plasma. Only 10% of the area available for beam extraction at the base of the plasma disk was used. Power cost can possibly be improved by either extracting a broad beam from the entire bottom of the plasma or by scaling down the discharge diameter to nearly 3.2 cm. In this thesis the latter approach is taken. Scaling down the discharge diameter will reduce the discharge volume, increase the discharge power density and hopefully reduce the power cost.

This chapter reviews the early development of a compact, low power, microwave-cavity ion source capable of high beam current densities.[19] The basic design of this prototype is described along with experimental systems used to operate the ion source. Langmuir probe electron density and temperature measurements and experimental ion beam extraction measurements are presented and discussed. Compared with Dahimene's ion source performance, the results show an increase in ion beam current density drawn from the 3.2 cm diameter extraction grid and a decrease in power cost. Ion current densities available for beam extraction exceed 10 mA/cm^2 and are achieved with less than 200 Watts of total microwave power. With the discharge diameter reduced to 5 cm, these experimental results demonstrate improvements in power cost, efficiency, and beam-current density.

2.2 COMPACT MICROWAVE-CAVITY ION SOURCE: PROTOTYPE I

The basic design approach of the first compact prototype microwave-cavity ion source has been described in a several earlier investi

17.8 cm

stainle

The di

orifice

GHz is

a coaxi

coax be

is DC i

the opp

of the

geometr

stock (

moving

microwa

from a

Impo

and dis

reduced

diameter

to reduc

surface

the micr

stainless

the bot

plate by

cap and

investigations.[1-5,7-11] The apparatus is shown in Figure 2.1. A 17.8 cm (7 in) brass cylinder (1), brass sliding short (2), and stainless steel base plate (3) form the conducting microwave cavity. The disk plasma is contained in a quartz chamber seated above an orifice in the stainless steel base plate. Microwave power at 2.45 GHz is coupled into this cavity or applicator through an input port by a coaxial probe (4). Within the cavity, the inner conductor of the coax becomes an electric antenna (5). The outer conductor and shell is DC isolated from the microwave power supply by a radial choke at the opposite end of the coaxial probe (Section 4.2.2.3). The length of the probe and the short are adjustable so that the cavity may be geometrically tuned to a resonant cavity mode. Silver plated finger stock (6) provides electrical contact between the brass cylinder and moving assemblies to prevent or attenuate any possible leakage of microwave radiation. During operation the discharge can be viewed from a screened port (7) in the side of the brass cylinder.

Important changes from earlier designs[1-5,7-11] are the base plate and discharge dimensions. The thickness of the base plate has been reduced to 1.5 cm, and the orifice has been reduced to 4.1 cm inside diameter. The base plate thickness has been made as thin as possible to reduce the weight and size of the apparatus and to keep most of the surface of the discharge exposed to the high electric fields within the microwave cavity. The base plate is machined from non-magnetic stainless steel and is cooled with a copper water line (9) soldered to the bottom of the plate. The brass cylinder is secured to the base plate by four machine screws (8) allowing easy access to the quartz cap and magnets. The discharge region is similar to the apparatus

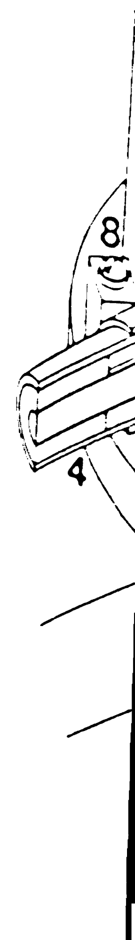
8
4

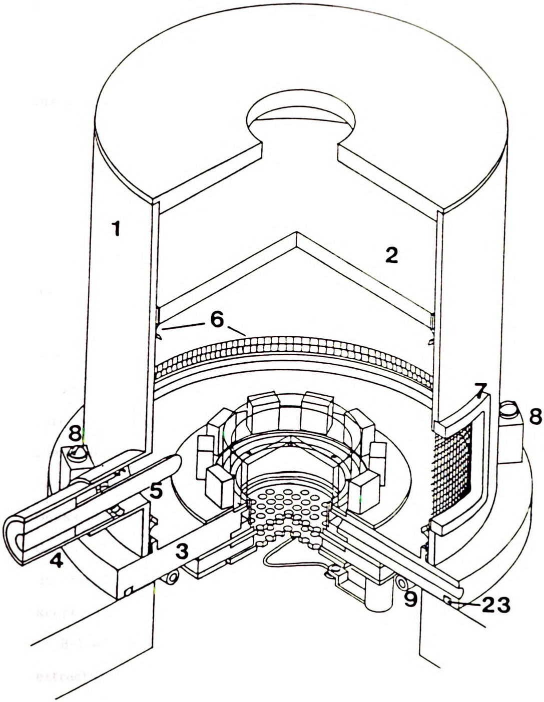

Figure 2.1 Microwave-Cavity Ion Source: Prototype I

usec

mag

disc

not

beer

cost

insic

rubt

used

throu

chan

symm

gas t

the d

throu

The

rare e

samari

neodym

Gauss a

Gauss.

discharg

keeper

Below

extracti

assembl

separate

used by Root and later Dahimene[3-11] where permanent samarium cobalt magnets were openly situated around and atop the quartz contained discharge. Although the dimensions of the cavity shell used here have not been changed from the earlier designs, the discharge diameter has been reduced from 9.4 cm to 4.9 cm to address the concern of power cost previously mentioned. In the detail of Figure 2.2, the 4.9 cm inside diameter, fused quartz cap (11) is set above the orifice on a rubber silicone vacuum seal (10). Different length quartz caps can be used to vary the discharge height from 2 cm to 5 cm. Gas is fed through the base plate from a radial channel (12) into an annular channel (13) and then into the discharge region by eight symmetrically-set pin holes (14). The quartz cap confines the working gas to a volume where incident microwave fields ignite and maintain the discharge. The quartz chamber is cooled with forced air blown through the screened viewing window.

The disk-shaped discharge is surrounded by various arrangements of rare earth magnets (15) made of either neodymium-iron-boron or samarium-cobalt. Each magnet is 1.3 x 1.3 x .5 cm. The neodymium-iron-boron magnets have a pole-face field strength of 3500 Gauss and the samarium-cobalt magnets have a field strength of 2500 Gauss. The magnets may be positioned symmetrically about the discharge in a number of multipole configurations on a soft iron keeper (16).

Below the discharge, screens, perforated plates, probes, or extraction optics may be mounted onto the base plate. Mounted assemblies will be discussed in later sections of this chapter as separate experimental configurations. Figure 2.2 shows the double

Figure 2

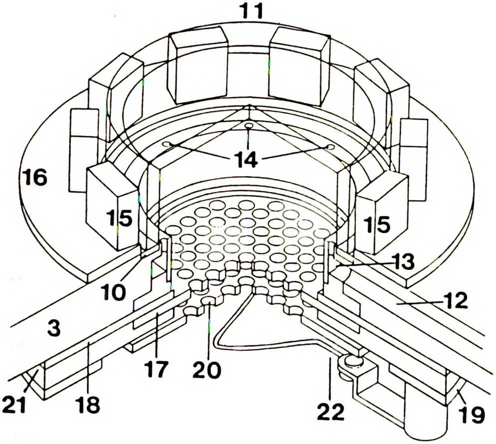

Figure 2.2 Detail of the Microwave-Cavity Ion Source Discharge Region

grid

extra

sits

syste

quar

2.3 G

2.3.1

Fi

studi

45.7

bell

exper

10 in

mecha

press

P_{bj}, i

(7) lo

Ga

remote

and o

the ga

the ion

grid assembly (17 - 22) used in high-voltage (1 - 2 kVolt) ion beam extraction (Section 2.3.4.1). The entire ion source with assemblies sits on an O-ring (23) and a Plexiglas DC block atop the vacuum system. The external pressure due to the vacuum is used to seat the quartz cap and base plate in position.

2.3 GENERAL EXPERIMENTAL SYSTEMS

2.3.1 LOW-PRESSURE VACUUM AND GAS FEED SYSTEMS

Figure 2.3 shows the vacuum and gas feed systems used in these studies. The ion source (1) and DC isolation block (2) sit atop a 45.7 cm x 45.7 cm cylindrical quartz bell jar (3). The transparent bell jar allows the ion beam and other phenomena to be observed during experimentation. The vacuum environment is continually evacuated by a 10 inch diffusion pump with a water cooled trap (4) and an assisting mechanical roughing pump (5). The pumping system has a base, no-flow, pressure of 2×10^{-3} mTorr. The bell jar or environmental pressure, P_{bj}, is monitored by an ionization gauge (6) and thermocouple gauge (7) located near the mid-section of the vacuum chamber.

Gas is fed to the ion source by a Tylan Flow Controller (8) with a remote manual control unit. Flows range from 0 to 50 sccm for nitrogen and oxygen and 0 to 70 sccm for argon. A quartz tube (9) is placed in the gas feed line just before the ion source to electrically isolate the ion source from the grounded gas feed line.

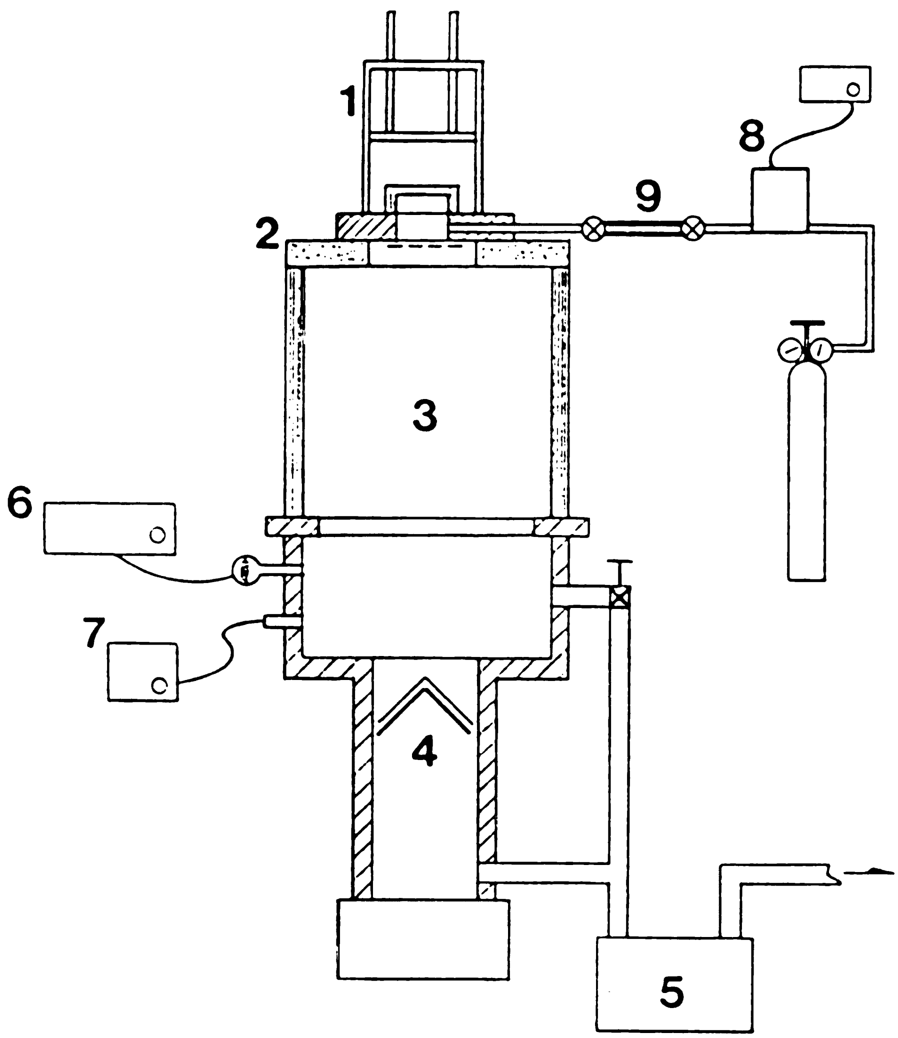

Figure 2.3 Vacuum and Pumping System

In

from

disch

or ot

is ca

where

partic

or gr

tempe

pressu

temper

measu

assume

2.3.2 M

The

microwa

wavegu

coaxial

2.46 GHz

In these studies a perforated plate separates the discharge volume from the vacuum system creating a pressure difference between the discharge and the vacuum chamber. To account for the effects of grids or other gas flow strictures, the discharge pressure, P_d in Pascals, is calculated as[34]

$$P_d = \frac{q(2\pi kM)^{1/2}}{A} \cdot \sqrt{T_d} + P_{bj} \cdot \sqrt{\frac{T_d}{T_{bj}}} \qquad (2.2)$$

where q is the gas flow rate in particles per second, M is the gas particle mass in kilograms, A is the open hole area in m^2 for a screen or grid separating the discharge from the vacuum, T_d is the temperature of the discharge in Kelvin, P_{bj} is the vacuum bell jar pressure measured by the ion gauge in Pascals, and T_{bj} is the bell jar temperature assumed to be 300 K. Because of the difficulty in measuring T_d, the experimental discharge discharge temperature is assumed to be 370 K throughout this thesis.

2.3.2 MICROWAVE POWER SYSTEM

The microwave system shown in Figure 2.4 consists of a Holiday microwave power supply, three-port circulator, matched dummy load, waveguide, cross waveguide directional couplers, power meters and coaxial cable. The Holiday supply is capable of delivering a 2.45 to 2.46 GHz signal with less than a 100 kHz band width between power

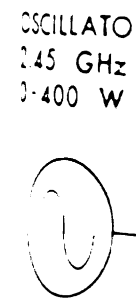

OSCILLATO
2.45 GHz
0-400 W

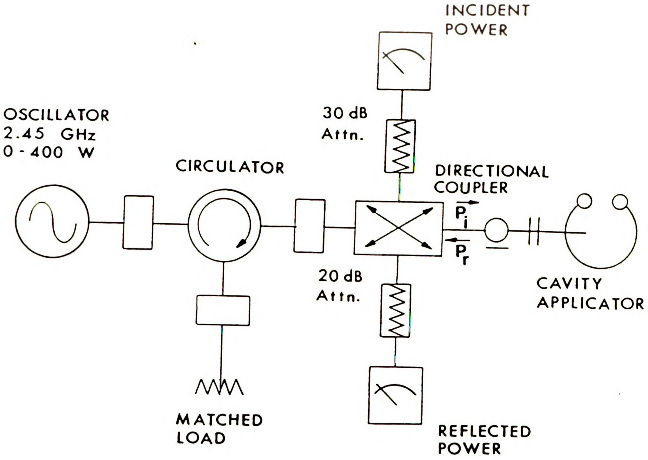

Figure 2.4 Microwave Power Circuit

levels

input p

power,

total po

dischar

Power r

microwa

2.3.3 LA

2.3.3.1

Lang

a discha

tempera

and plas

method

Other d

(36) and

The

wires in

have eq

perturbi

levels of 50 to 400 Watts. The total input power, P_t, coupled to the input probe and cavity, is equal to the difference between incident power, P_i, and reflected power, P_r, read from the power meters. This total power is then distributed between the power absorbed by the discharge, P_a, and power lost to the cavity walls, P_b.

$$P_t = P_i - P_r = P_a + P_b \tag{2.3}$$

Power readings are calibrated to include loss of power in the microwave circuit.

2.3.3 LANGMUIR PROBE AND MEASUREMENTS AND TECHNIQUES

2.3.3.1 LANGMUIR PROBE AND CIRCUIT

Langmuir probe measurements are a standard tool for characterizing a discharge. Measured values of electron density and electron temperature may be used to predict the ion flux for beam extraction and plasma diffusion applications. The double-floating Langmuir probe method used in this Thesis was first used by Johnson and Malter.[35] Other discussions on the probe technique may be found in references (36) and (37).

The electric probe shown in Figure 2.5 consists of two tungsten wires insulated by Pyrex tubing. The collecting tips of the probe have equal area and have been made small to avoid significantly perturbing the discharge. A perforated plate and assembly holds the

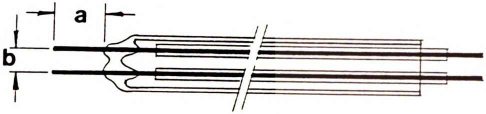

Probe Dimensions:	
tungsten radius	.012 cm
tungsten length (a)	.34 cm
probe spacing (b)	.25 cm

Figure 2.5 Double Langmuir Probe

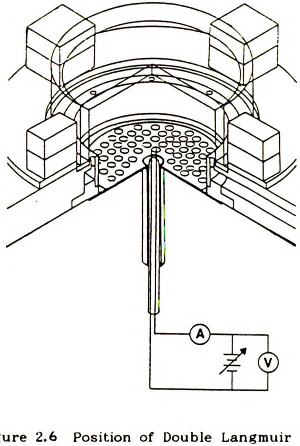

Figure 2.6 Position of Double Langmuir Probe

prol

micr

the

The

2.6.

2.3.3

A t

given

voltage

logarit

sources

Sinc

must be

In Equa

and i_{e1}

total ele

define I

probe in position at the bottom center of the discharge where microwave fields and static magnetic fields are assumed to be zero in the presence of a discharge and thus do not effect probe measurements. The experimental set up and electric circuit are also shown in Figure 2.6.

2.3.3.2 CALCULATION OF ELECTRON DENSITY AND TEMPERATURE WITH LANGMUIR PROBE I-V READINGS

A typical double-floating Langmuir probe I-V characteristic is given in Figure 2.7 along with a schematic showing probe currents and voltages. The electron temperature and density are found by a logarithmic plot method which has been discussed extensively by other sources.[9,35,36] The basic derivation is quickly reviewed here.

Since the probes are floating, the sum of current to each probe must be zero.

$$i_{i1} + i_{i2} - i_{e1} - i_{e2} = 0 \tag{2.4}$$

In Equation (2.4), i_{i1} and i_{i2} are the ion currents to probes 1 and 2 and i_{e1} and i_{e2} are the electron currents to probes 1 and 2. The total electron and ion currents can be set equal to each other to define I_p.

$$I_p = i_{i1} + i_{i2} = i_{e1} + i_{e2} \tag{2.5}$$

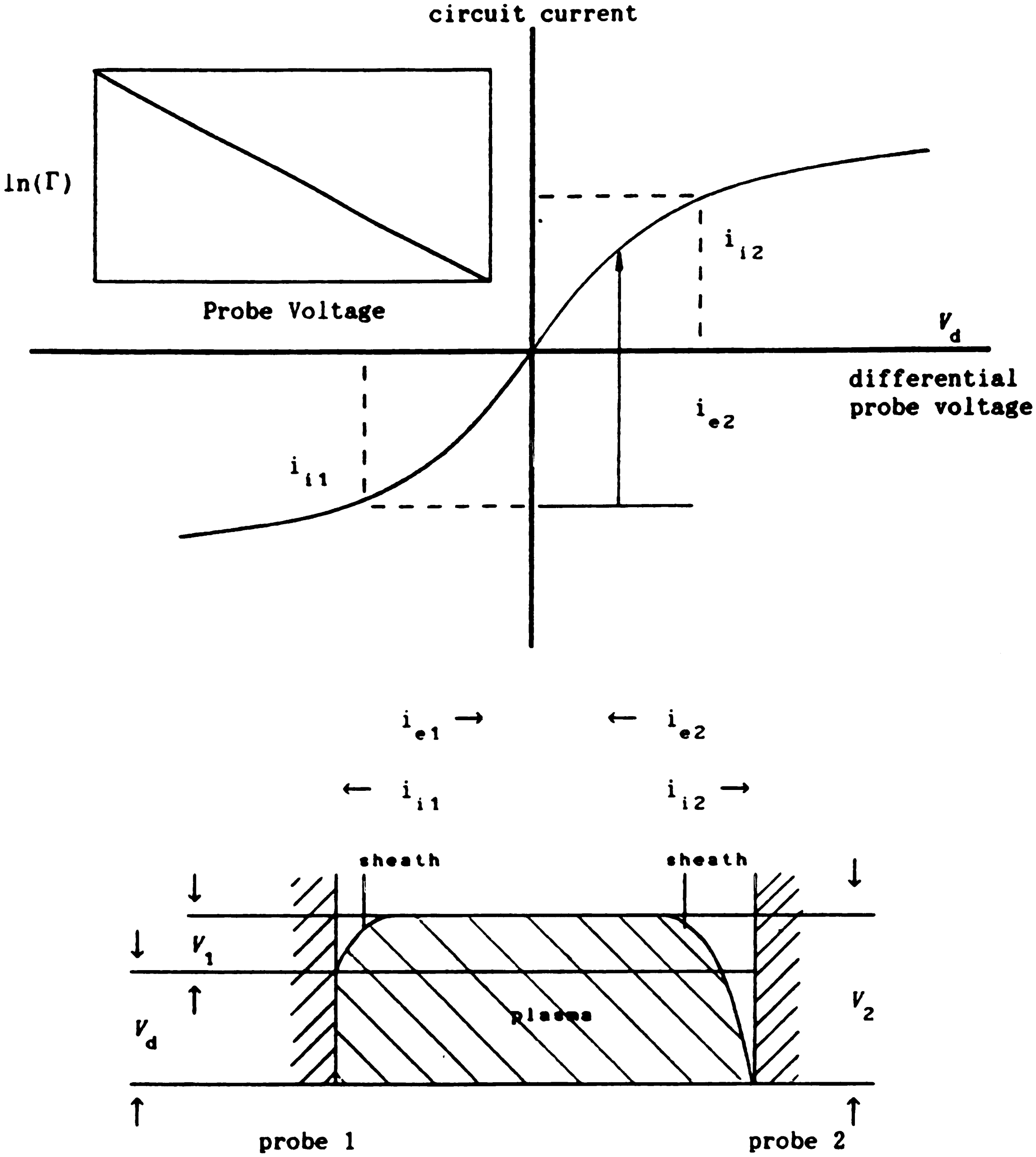

Probes with fairly large negative voltage

Figure 2.7 Typical I-V Characteristics and Analysis

The

Bolt

whe

prob

vari

plas

$= V_d$

I

wher

Takin

T_e is

assum

The

ion cu

The electron currents to each probe may be written in terms of the Boltzman relation. I_p becomes

$$I_p = I_{01}\, e^{(-eV_1/kT_e)} + I_{02}\, e^{(-eV_2/kT_e)} \qquad (2.6)$$

where V_1 and V_2 are the voltages on the probes and I_{01} and I_{02} are the probe currents when V_1 and V_2 are zero. If there is no local variation in the plasma potential, i.e. if the conditions of the plasma do not vary in the region between the two probes, then $(V_1 - V_2) = V_d$, the applied voltage on the double probe.

I_p can be divided by i_{e2} to get

$$\frac{I_p}{i_{e2}} = \Gamma + 1 \qquad (2.7)$$

where

$$\Gamma = \left(\frac{I_{01} e^{(-eV_1/kT_e)}}{I_{02} e^{(-eV_2/kT_e)}} \right) \qquad (2.8)$$

Taking the natural log of (2.8) and rearranging, it can be shown that T_e is proportional to the slope of the plot of $\ln(\Gamma)$ versus V_d assuming equivalent probes.

The knees of the double probe I-V characteristics mark the point of ion current saturation. (See Figure 2.7.) In this thesis the Bohm sheath

From

where

particl

Express

for J_i

The

selectin

ion dens

where A

thicknes

radius.

this met

sheath criterion[37] is used to determine electron and ion densities. From the criterion this ion current flux to a surface is[36,38]

$$J_i = 0.61\ e\ n_i \left(\frac{kT_e}{M_i}\right)^{1/2} \quad . \tag{2.9a}$$

where e is the electron charge in Coulombs, n_i is the ion density in particles/m^3 and M_i is the ion mass in Kg, and T_e is in degrees K. Expressed in terms of T_e and n_i for argon, Equation (2.9a) is

$$J_i = 1.41 \times 10^{-19} \cdot n_i \cdot T_e^{1/2} \tag{2.9b}$$

for J_i in mA/cm^2.

The knee of the curve marks the ion saturation limit. Thus selecting I_p at the knee of the I-V curve and assuming electron and ion density to be equal within the discharge,

$$n_i = n_e = \frac{I_p}{0.61\ e\ A_p} \left(\frac{M_i}{kT_e}\right)^{1/2} \tag{2.10}$$

where A_p is the probe area. This calculation assumes that the thickness of the plasma sheath is small in comparison to the probe radius. There is no need to know plasma potential to calculate T_e as this method uses floating probes. Unlike the analysis of Johnson and

Mal

is

coll

or

data

I-V

are

vers

ion

2.3.3

C

meas

made

elect

ener

this

high

elect

Maxw

tempe

So

secon

assum

Malter,[35] the Bohm sheath criterion has been used here so that there is no need to make any correction in the probe radius for an effective collection area involving the plasma sheath.[35,36]

In practice a series of I-V characteristic points are taken by hand or computer. Because of the smooth transition throughout the I-V data, estimated points for I_p are selected just below the knees on the I-V plot (Figure 2.7). Ln(Γ) versus V_d is then plotted. New points are taken moving closer to the vicinity of the knees until ln(Γ) versus V_d is as linear as possible. After the optimal knee points for ion current saturation have been selected, T_e and n_e are calculated.

2.3.3.3 INTERPRETATION OF LANGMUIR PROBE READINGS

Care should be exercised in the interpretation of Langmuir probe measurements. A number of assumptions and approximation have been made which make the theory inexact. The first is assuming that the electron energy distribution is Maxwellian. Measurements of electron energy distributions in ECR microwave plasmas by J. Hopwood[39] show this to be a false assumption. The double probe method samples the high energy end of the electron energy distribution from which the electron temperature is mathematically calculated. If there is no Maxwellian electron energy distribution then there is no true temperature and density measurements are not accurate.

Some other assumptions include perfectly absorbing, (i.e no secondary electron emission), and equal-area probes. It is also assumed that the plasma sheath about the probes is collisionless and is

rea

ion

orb

in

the

dis

fro

pur

sat

The

cha

ope

2.3.4

2.3.4

H

extra

The

Dahin

also

extrac

thick

is small compared to the probe radii. This last assumption is reasonable for low-pressure plasmas with densities above $5x10^{11}$ ions/cm^3. At lower densities, however, the sheath becomes large and orbital motion of ions about the probe may effect measurements.[36]

It is difficult to correct for the non-ideal circumstances involved in Langmuir probe measurements. In general it is difficult to rewrite the Langmuir probe theory for an arbitrary electron energy distribution or to make corrections for secondary electron emission from the probe.[36,38] Error analysis is nearly impossible, even if pursued statistically, because of the uncertainty in locating ion saturation points on the I-V curve and the inexactness of the theory. The probe measurements provide good order-of-magnitude estimations of charged particle density and may be used to predict the ion source's operating characteristics.

2.3.4 ION EXTRACTION OPTICS AND ASSEMBLIES

2.3.4.1 DOUBLE-GRID EXTRACTION ASSEMBLY AND CIRCUIT

High energy beam extraction is carried out by two flat, graphite extraction grids supplied by Optic Electronics Corporation of Texas. The grids and extraction assembly, which were also used by Dahimene,[9] are shown in Figure 2.8a. (Note: the grid assembly is also depicted in Figure 2.2). Figure 2.8b shows the details of an extraction hole. The first grid (17), the screen grid, is about .2 mm thick (d) and has 120, 2 mm diameter holes (a) with 2.4 cm

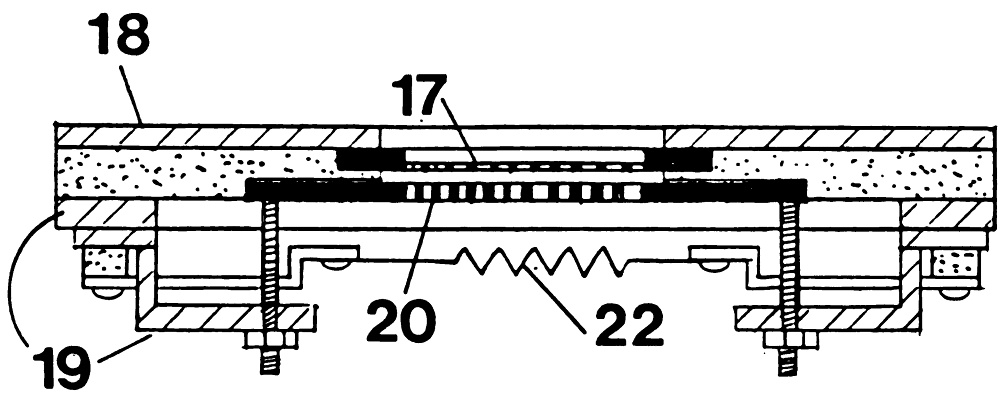

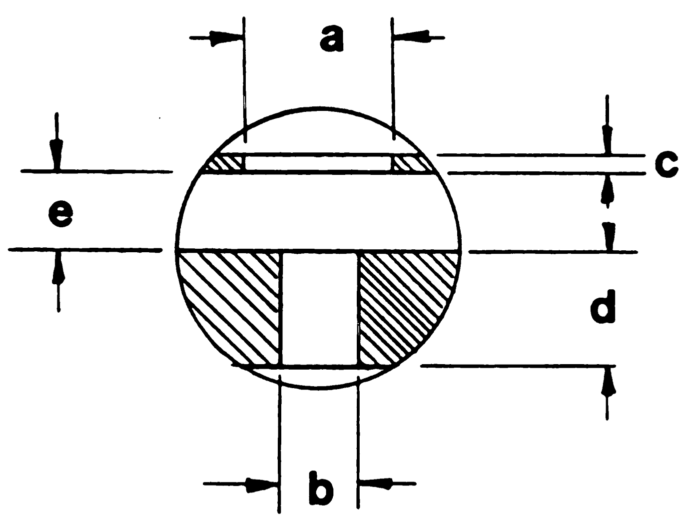

Figure 2.8 Double-Grid Extration Optics

cen

gri

ext

is

pyr

mou

scr

allo

piec

scre

late

opti

extr

i.e.

diam

T

of a

by

as t

The

radia

curr

curr

center-to-center spacing. The second grid (20), the acceleration grid, is 1.59 mm thick (c) and has 1.6 mm diameter holes (b). The extraction grid separation (e) used in the experiments of this thesis is 1 mm. Both grids are machined from 1/16 inch, high-density pyrolitic-graphite.

The screen grid is fixed by three screws to a stainless steel mounting plate (18). The second grid is supported by three adjustable screw posts mounted on a stainless steel ring (19). The screw posts allow the grid separation to be easily adjusted. The two mounting pieces are separated by mica sheets (21) and are held together with screws and teflon washers for electric isolation. They can also be laterally adjusted to facilitate the alignment of the extraction optics. The extraction diameter is 3.2 cm in diameter, and the total extraction area is 8.04 cm^2 of which 3.77 cm^2 is open to extraction, i.e. 47% transparency. The entire extraction assembly is 5 inches in diameter.

The high-voltage DC extraction circuit shown in Figure 2.9 consists of a positive voltage, V_s, and negative voltage, V_g, supply separated by ground. In the circuit the entire cavity is placed at high voltage as the screen grid is in directl contact with the cavity base plate. The microwave supply is isolated from the extraction circuit by the DC radial choke. (See Section 4.2.2.3). During extraction the ion beam current is read as the difference between positive and negative supply currents,

$$I_b = I_s^+ - I_a^- . \qquad (2.11)$$

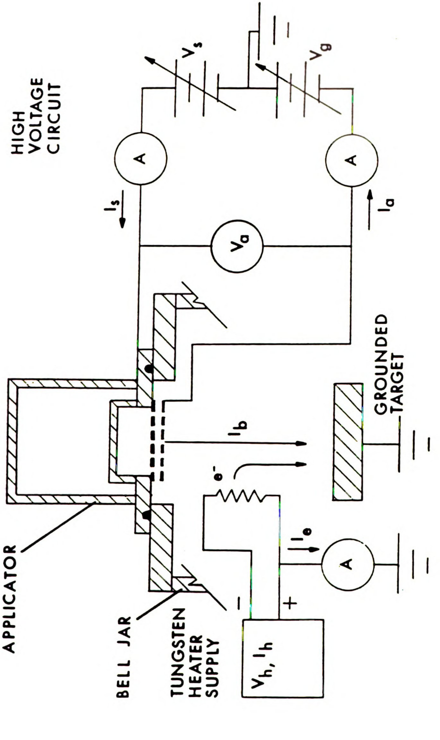

Figure 2.9 Double-Grid Extraction Circuit

ne

he

be

th

in

ta

ch

cu

ra

de

sp

vo

eV

pr

2.3

us

op

an

tr

Electron emission from a heated tungsten filament (22) is used to neutralize the ion beam. The emission current, I_e, on the filament heater is adjusted to equal I_b in order to electrically neutralize the beam and keep it well collimated. V_g is set negative to insure that the emitted electrons do not pass through the grids and cause errors in the beam current readings. A deep-throated Faraday cup or grounded target is placed down stream to collect the ion beam, to observe charge exchange degradation of the beam, and to verify the beam current magnitude read on the extraction circuit ammeters.

In these experiments the extraction voltage,

$$V_s + V_g, \tag{2.12}$$

ranged from 1000 Volts to 1600 Volts. This range was dictated by the design of the grids, which have been constructed for material sputtering applications at energies >1000 eV. Although the lower voltages can be applied to the grids, a well-collimated beam below 800 eV cannot be easily extracted from a dense plasma. This is a common problem encountered with double-grid extraction optics.[40]

2.3.4.2 SINGLE-GRID EXTRACTION ASSEMBLIES AND CIRCUIT

In single-grid extraction, a single screen or perforated plane is used to extract ions from the discharge. Two types of single-grid optics have been studied. The first grid, shown in Figure 2.10, is an anisotropically etched 3 inch diameter silicon wafer with 75% transparency. These grids, prepared by Dr. Engemann and Max Keller at

Specifications:

3" diamter silicon wafer [100]
Anisotropically etched
75 % transparency

a = .7 mm
b = .9 mm
c = .19 mm
d = .20 mm

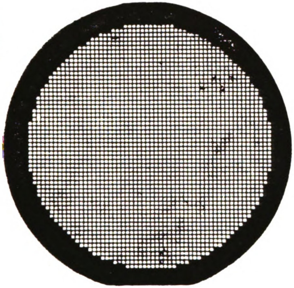

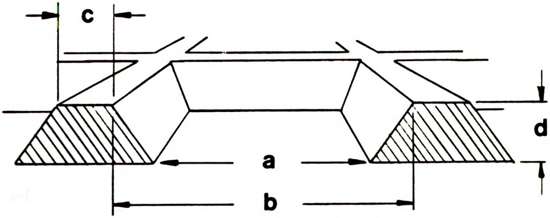

Figure 2.10 Silicon-Grid Extraction Optics

the
for
are
bea
secc
stee
stai
T
but
shee
extra
singl
disch
accele
throu
positi
double
optics
to the

2.4 OP
S

2.4.1 C

In
metho

the University at Wuppertal in West Germany,[41] have been designed for rf discharges[42] with ion densities of 10^{10}ion/cm^3. Because they are manufactured from silicon they are ideal for low energy oxygen ion beams used in micro-electronic silicon semiconductor fabrication. The second grid is a 40% transparent, 25 x 25 lines per inch stainless steel tungsten screen. The screen is stretched and held by a stainless steel assembly as shown in Figure 2.11.

The single-grid extraction assemblies are fixed to the base plate, but are electrically isolated by either mica or Kapton insulating sheets. The extraction circuit is similar to that used in double-grid extraction; the only difference is that there is no screen grid. In single-grid extraction the base plate orifice wall is used to bias the discharge. At the bottom of the discharge volume, ions are accelerated from plasma potential, through the plasma sheath, and then through the single-grid. The plasma sheath is analogous to the positive-potential, shielding boundary of the screen grid used in double-grid extraction. Indeed, the design of single-grid extraction optics strongly depends on the formation of the plasma sheath adjacent to the single accelerating grid.

2.4 OPERATION AND PERFORMANCE OF THE COMPACT MICROWAVE-CAVITY ION SOURCE PROTOTYPE

2.4.1 OPERATION OF THE ION SOURCE: PROTOTYPE I

In this section the experimental systems come together. First the method of operation is presented in detail. This includes igniting

Single-grid: side view. The screen is clamped into place.

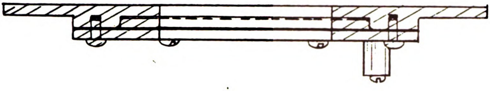

Single-Grid: bottom view.

The tungsten filament is used to neutralize the beam.

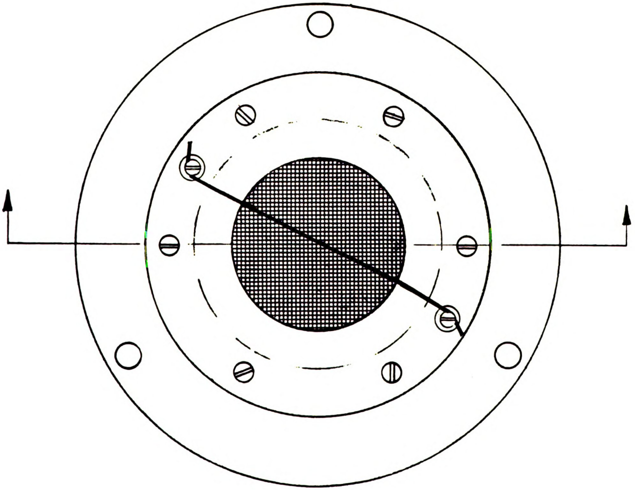

Figure 2.11 Screen-Grid Extraction Optics

the

ion s

heig

powe

cylin

to ti

For a

empt

TE_{lmn}

TM_{lmn}

In (2.1

resona

mth ze

zeros

numero

The

and T

theore

the discharge and tuning the resonant cavity. The microwave-cavity ion source works on the principle of adjusting the internal cavity height, L_s, and input probe length, L_p, in order to couple microwave power into a single resonant cavity mode. For a perfectly conducting cylindrical cavity these modes are specified by well-known solutions to time-harmonic wave equations bounded by a cylindrical geometry. For a selected frequency and fixed radius, the theoretical lengths for empty cylindrical cavity resonant modes are given by the equations

TE_{lmn} modes:

$$L_{s(lmn)} = \frac{\lambda_o}{2n \cdot \left[1 - \left(\frac{x'_{lm} \lambda_o}{(2\pi a)} \right)^2 \right]^{1/2}} \tag{2.13}$$

TM_{lmn} modes:

$$L_{s(lmn)} = \frac{\lambda_o}{2n \cdot \left[1 - \left(\frac{x_{lm} \lambda_o}{(2\pi a)} \right)^2 \right]^{1/2}} \tag{2.14}$$

In (2.13) and (2.14), $L_{s(lmn)}$ is the modal cavity height, λ_o is the resonant wavelength, a is the cavity radius, and x_{lmn} and x'_{lmn} are the mth zeros of the lth order Bessel functions, $J_l(x)$ and $J'_l(x')$. These zeros are tabulated by Harrington[43] and may also be found in numerous mathematic reference books.

The cavity is not a geometrically perfect cylinder, so actual TE and TM lengths are slightly perturbed. Table 2-I lists the theoretical heights for a 17.8 cm diameter cavity and lists the

TABLE

MODE
TE_{111}
TM_{011}
TE_{211}
TE_{011}
TM_{111}
TE_{112}

(*) Mode r

In certa
theoretica
to a rota

TABLE 2-I. SHORT AND PROBE LENGTHS FOR STANDARD MODES IN THE COMPACT MICROWAVE ION SOURCE PROTOTYPE

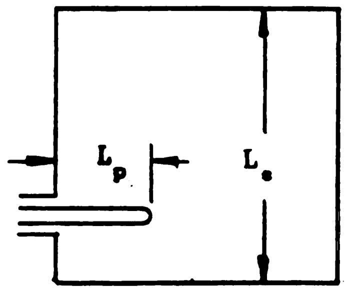

L_s = cavity height L_p = probe length

MODE	THEORETICAL CAVITY HEIGHTS (cm)	EXPERIMENTAL EMPTY CAVITY HEIGHTS (cm), PROBE LENGTHS (cm), AND CAVITY QUALITY
		HEIGHT/LENGTH/QUALITY
TE_{111}	6.69	6.65 / .86 / 662 6.67 / .61 / 790
TM_{011}	7.21	7.5 / .55 / 471
TE_{211}	8.24	8.45 / .76 / 278 8.60 / .10 / 1366
TE_{011}	11.27	(*)
TM_{111}	11.27	(*)
TE_{112}	13.39	13.49 / .10 / 471
		13.52 / .10 / 557

(*) Mode not identified

In certain cases two experimental modes related to a single theoretical modes are identified. This may be due to degeneracy or to a rotational variation in the excited mode.

e

s

e

of

po

Sc

th

ma

Ce

pe

init

req

has

ener

brea

thes

for c

thedi

TE_{11}

Th

estab

when

and n

source

to abo

pressu

experimental internal cavity short and input probe lengths for the ion source cavity with no plasma, quartz cap, or magnets. The experimental modes are found by a standard microwave circuit technique of frequency-sweeping the cavity about 2.45 GHz and identifying positions where power reflected out of the cavity becomes zero.[30] Some modes cannot be clearly identified because of the perturbation of the input probe. Table 2-II shows the effects of placing a ten-pole magnet configuration (shown in Figure 2.1) within the cavity. Certain modes can no longer be easily identified or are strongly perturbed.

The identification of these empty cavity modes is important for the initial excitation of the discharge. Strong electric fields are required to break down the working gas. The resonant microwave-cavity has a high quality factor, Q, associated with stored electromagnetic energy. Many simple gases (hydrogen, helium, argon, etc.) easily break down if sufficient input power and gas flow are supplied. In these low-pressure experiments the TE_{111} and TE_{211} modes are preferred for operation as the electric fields are tangential to the top of thedischarge volume. See Figure 2.12 for the field patterns of the TE_{111} mode.

The discharge of the ion source prototype is ignited by establishing the proper gas pressure and then applying microwave power when the cavity is tuned to a resonant condition. For argon, oxygen, and nitrogen, 50 to 70 sccm of gas is initially introduced to the ion source when there are no magnets within the cavity. This corresponds to about 42 mTorr discharge pressure, P_d, and about 1 mTorr vacuum pressure, P_{bj}, assuming that a 50% transparent grid or screen

TABI

MOD

TE
TM
TE
TE
TM
TE

(*)

TABLE 2-II. SHORT AND PROBE LENGTHS FOR STANDARD MODES IN THE COMPACT MICROWAVE ION SOURCE PROTOTYPE: IGNITION AND TUNED OPERATION

MODE	IGNITION POINT EXPERIMENTAL HEIGHTS (cm) AND PROBE LENGTHS (cm): 4 POLE MAGNETIC FIELD	MATCHED CAVITY OPERATING POINT EXPERIMENTAL HEIGHTS (cm) AND PROBE LENGTHS (cm): 4 POLE MAGNETIC FIELD
	HEIGHT/LENGTH	HEIGHT/LENGTH
TE_{111}	6.68 / 1.01	7.01 / 1.03
TM_{011}	no ignition point	8.35 / 1.11
TE_{211}	9.12 / 1.50	10.85 / 2.6
TE_{011}	(*)	(*)
TM_{111}	(*)	(*)
TE_{112}	discharge difficult to ignite, mode not studied	

(*) Mode not identified

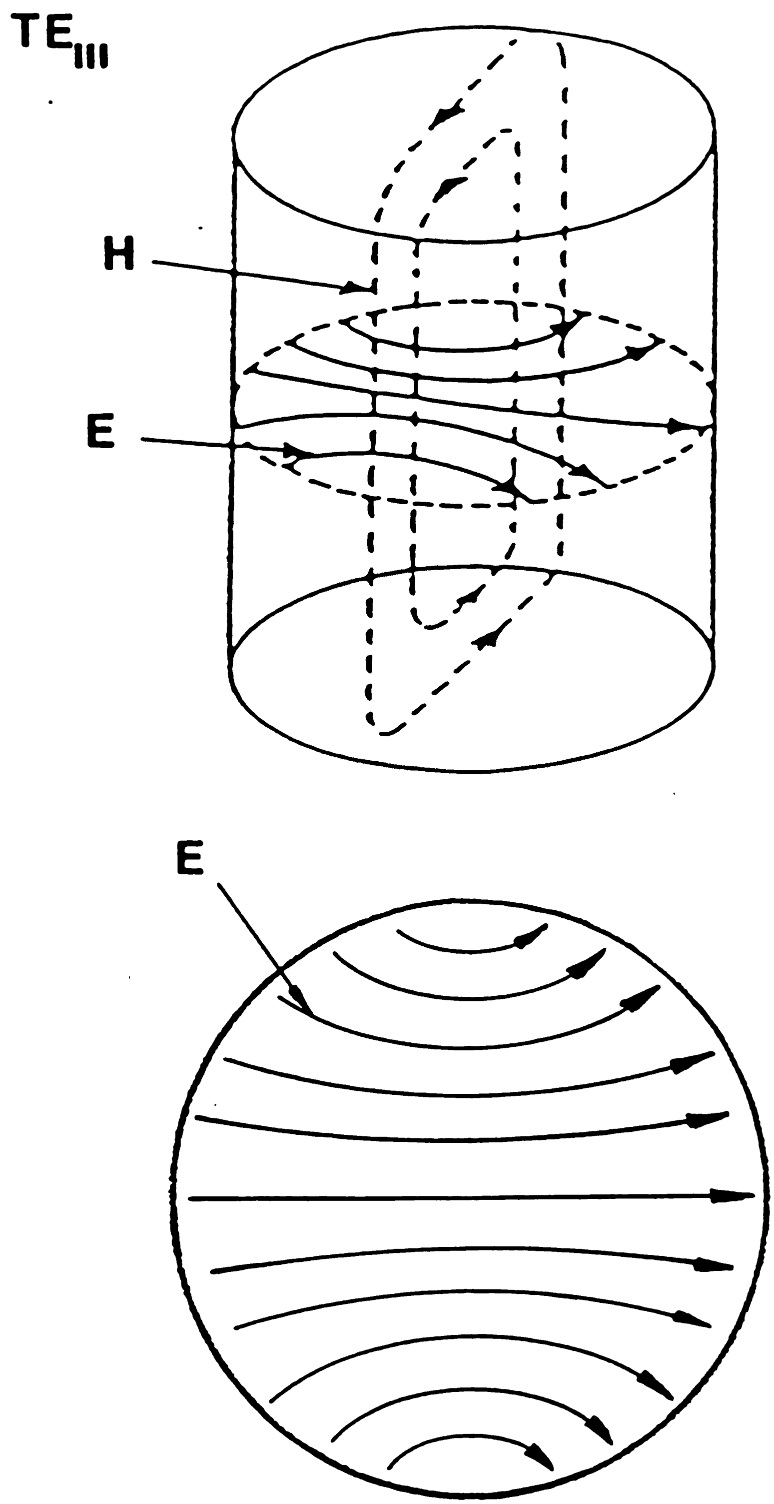

Figure 2.12 Electromagnetic Fields of the TE_{111} Mode

sepa
adju
incr
oscil
the
gase
and/
G
low
with
field
The
the
When
the
The
to th
TE_{11}
only
large
as m
about
patte
power
to ma
power

separates the two regions. The cavity short and probe length are then adjusted until the TE_{111} mode is located. The input power is increased to 50 Watts or until the bandwidth on the microwave oscillator becomes sharp. At this point the strong electric fields of the resonant cavity can easily break down the gas. More difficult gases such as oxygen may require initial excitation with a Tesla coil and/or input power above 100 Watts.

Gases break down more easily in ECR static microwave fields. At low flows and pressures argon, oxygen, and nitrogen can be broken down with moderate input gas flows of 10 to 20 sccm. The strong electric fields applied with the ECR zones generate highly energetic electrons. The magnetic field also contains many of these electrons and increases the avalanching, ionizing processes that result in discharge ignition. When a discharge is first ignited, it becomes a large perturbation in the cavity. The resonant mode is disturbed and reflected power rises. The cavity short and input probe must be retuned, to match the cavity to the microwave circuit and reduce the reflected power. For the TE_{111} mode in this microwave ion source, retuning typically requires only 5 to 7 mm short and probe variation. See Table 2-II. With the large plasma perturbation in the cavity, the cavity Q may decrease by as much as an order of magnitude. Electric field probe measurements about the cavity wall[39] have shown that the characteristic modal pattern of the distributed electric fields is retained. As flow and power conditions are changed, the applicator is continuously retuned to maintain a good microwave circuit load match and maintain efficient power coupling.

The
mod
bea

2.4.2

T
were
extra
heati
appr
sugg
avail
the g
Ga
ion s
speci
1.78x1

Equat
the g

The TE_{111}, TM_{011}, and TE_{112} modes were tested in the applicator. The TE_{111} performed better during operation than all other tested modes. This mode is used exclusively throughout Langmuir probe and beam extraction experiments.

2.4.2 LANGMUIR PROBE MEASUREMENTS

The Langmuir probe circuit and theory discussed in section 2.3.3 were used to measure argon ion densities and to predict the extractable beam current densities. These measurements show that ECR heating is necessary to operate the ion source at discharge pressures appropriate for beam extraction, 1 to 5 mTorr. The measurements suggest that an ion current density in excess of 10 mA/cm^2 is available for extraction at the bottom of the discharge, adjacent to the grid extraction plane.

Gas flow and discharge pressure specify the operating point of the ion source. To correlate flow and pressure, Equation (2.2) is specialized for the open hole area of the Langmuir probe grid, 1.78×10^{-4} m^2, and a discharge temperature of 370 K.

$$P_d\ (\mathrm{Torr}) = \left[8.71\times10^{4} \cdot q \ + 1.11 \cdot P_{bj}(\mathrm{Torr}) \right] \qquad (2.13)$$

Equation (2.13) is plotted in Figure 2.13 for experimental values of the gas flow, q, in sccm, and the bell jar pressure, P_{bj}.

Discharge Pressure in Torr

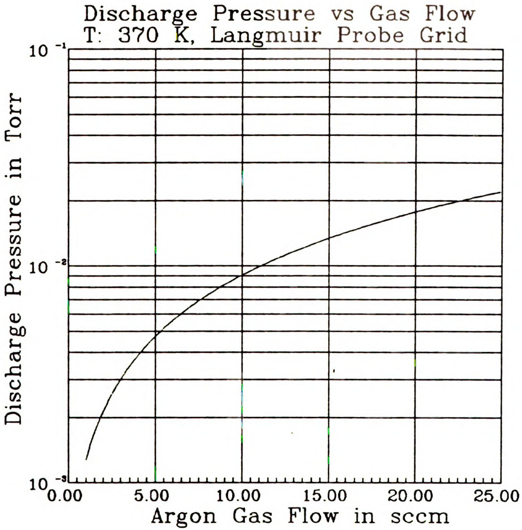

Fig 2.13 Vacuum Pressure versus Flow for Argon

T

volu

cap

is de

volu

Thus

while

Th

With

susta

rate

condi

Tunin

be ma

most

ECR

press

Fi

confi

not b

disch

was c

Watts

The performance of the ion source changes with discharge height or volume. The discharge height is defined as the height of the quartz cap plus the 1.5 cm thickness of the base plate. The discharge volume is defined as the sum of the quartz cap volume and base plate orifice volume.

$$V_d = \left[6.0 \cdot \pi \cdot (\text{quartz cap height}) + 19.8\right] \ \text{cm}^3 \qquad (2.14)$$

Thus a 3.0 cm quartz cap will hold a 4.5 cm high, 76 cm^3 discharge while a 1.0 cm quartz cap will hold a 2.5 cm high, 37 cm^3 discharge.

The ion source was initially operated with no permanent magnets. With only 150 Watts of incident power the discharge was difficult to sustain at pressures below 10 mTorr, corresponding to an argon flow rate of 11 sccm. (See Figure 2.14.) Electron temperatures for this conditions ranged from 40,000 K at 70 mTorr to 70,000 K at 10 mTorr. Tuning was difficult at lower pressures and the discharge could only be maintained with a substantial increase in microwave power. Since most ion beam extraction is carried out at pressures below 5 mTorr, ECR heating had to be introduced to improve microwave coupling at low pressures.

Figure 2.15 shows the four-pole samarium-cobalt permanent magnet configuration used in early experiments. The magnet arrangement may not be optimal, but in early experiments it was sufficient to keep the discharge stable at low pressures and moderate powers. The ion source was operated in the TE_{111} mode exclusively with powers varying from 90 Watts to 140 Watts. Langmuir probe electron density measurements are

Electron Density (10^{12}/cm^3)

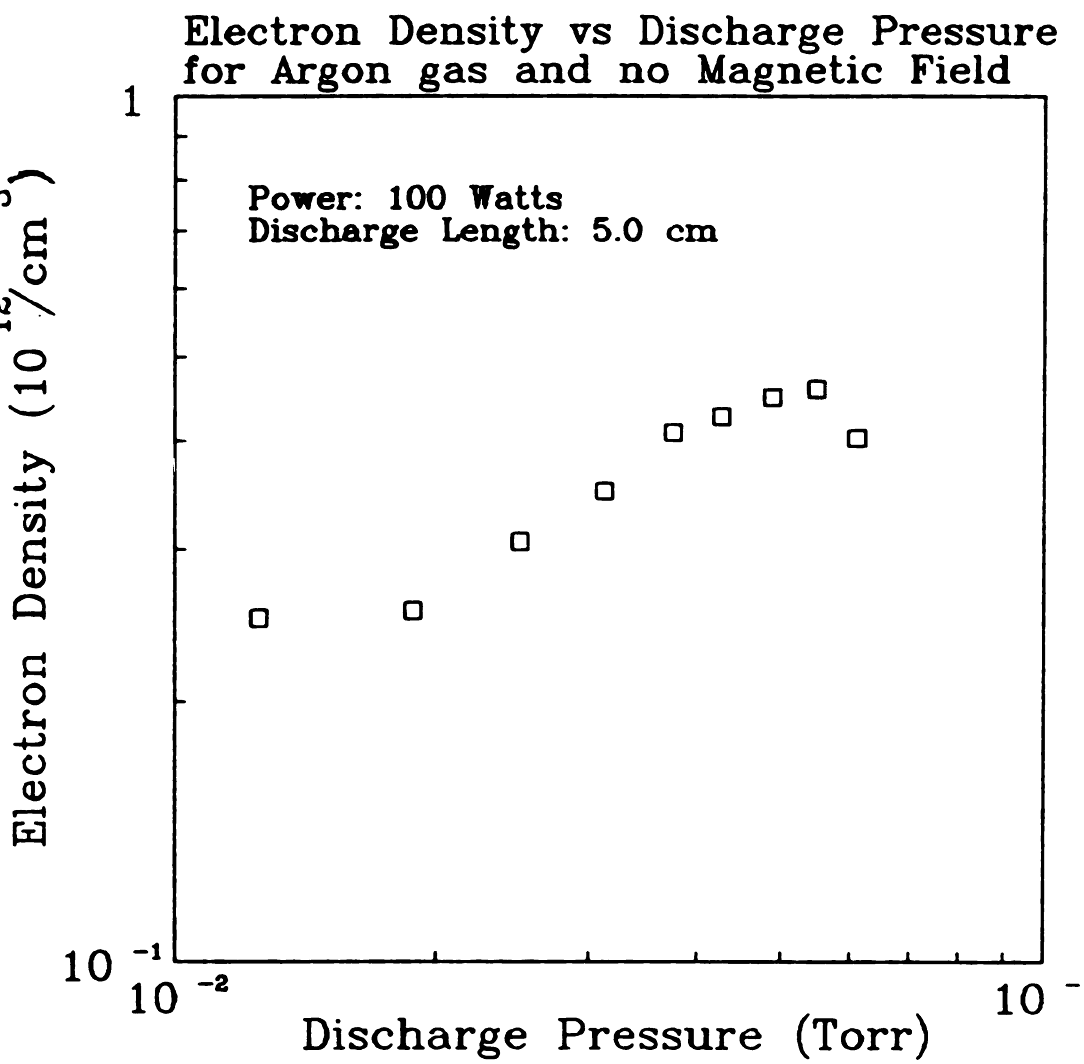

Figure 2.14 Electron Density versus Discharge Pressure–
No Magnets

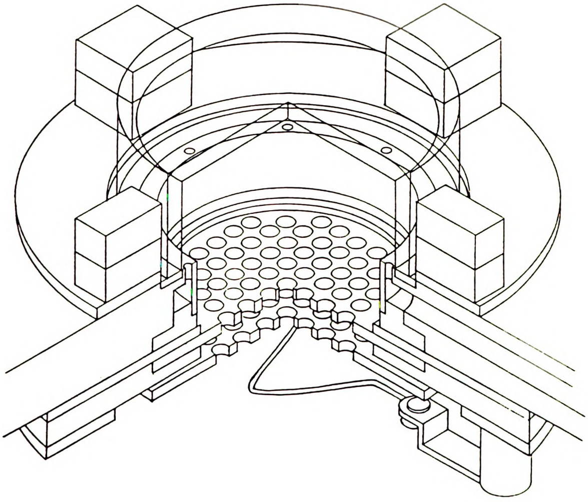

Figure 2.15 Four-Pole Samarium-Cobalt Magnet Configuration

given in Figures 2.16 through 2.18 for variations in pressure, power and discharge height.

Figure 2.16 demonstrates that the four-pole samarium-cobalt permanent magnet configuration can be used to sustain the plasma at discharge pressures acceptable for ion beam extraction. Figure 2.17 shows ion density in two different size discharges, one with a 1.0 cmquartz cap and 38 cm^3 volume, the other with a 3.5 cm quartz cap and a 85 cm^3 volume. Strikingly the smaller volume discharge has lower densities even though the power density is larger in the 38 cm^3 volume than in the 85 cm^3 volume. Intuitively one might expect that for a fixed power, the electron density would necessarily increase as discharge height or volume is decreased; electron density rises with the average discharge power density. However, Figure 2.17 suggests that there is an optimal discharge height.

The explanation for the above observation lies in the balance between volume ionization and the diffusion loss of charged-particles to the containing surface walls. As the height of a fixed radius discharge decreases, the surface-to-volume ratio decreases, and ionization power required to maintain the discharge at a particular density also decreases. As the discharge height is further decreased, the surface-to-volume ratio, and the required ionization power, will reach a minimum and then begin to rise. Thus this minimum marks the lowest required ionization power and the lowest surface recombination loss. This optimal height can be predicted by low-pressure discharge diffusion theories which are covered in Chapter 3.

Figure 2.18 shows charged-particle density for a number of fixed powers and pressures below 10 mTorr. Densities range from $2x10^{11}$ to

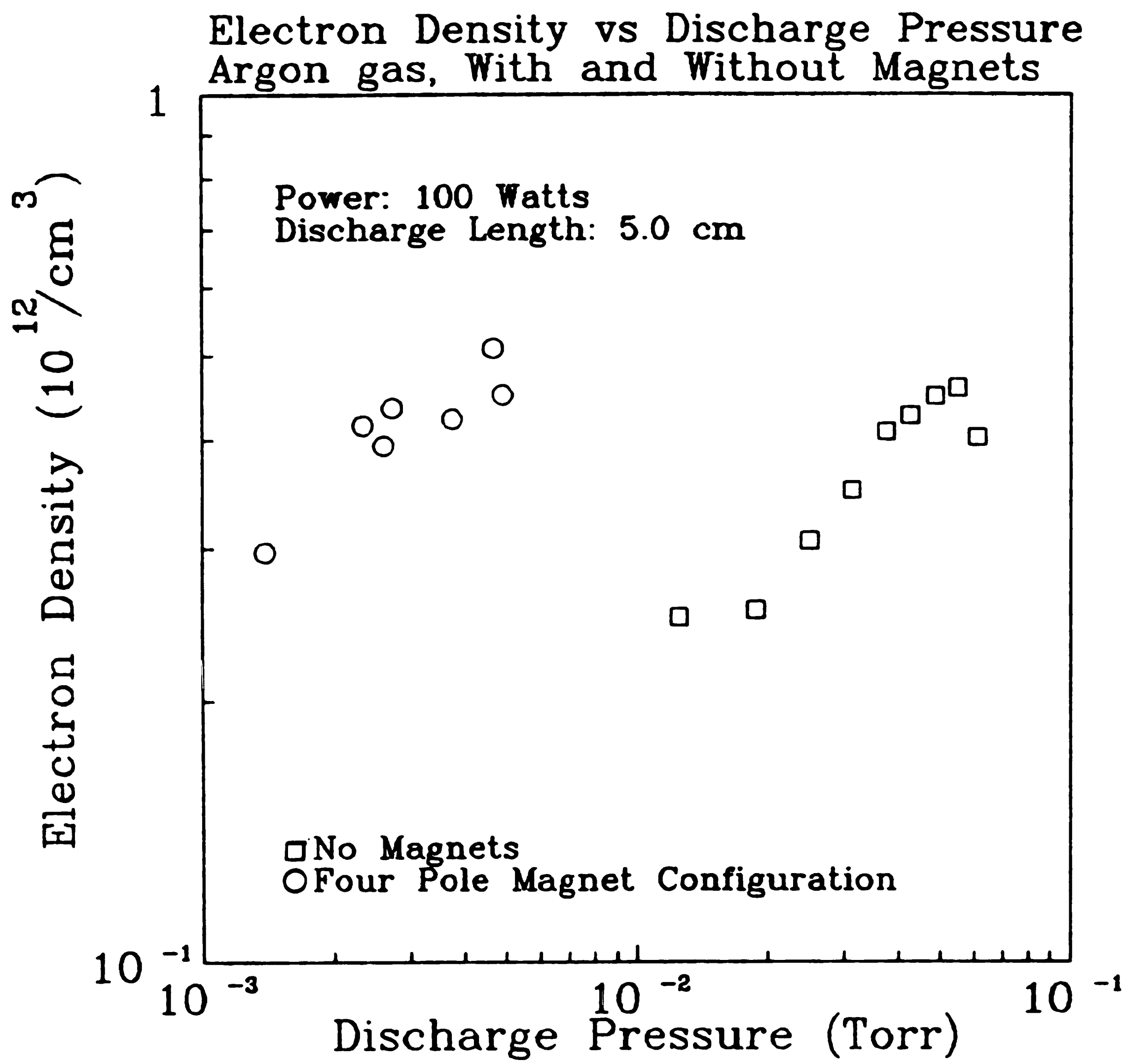

Figure 2.16 Electron Density versus Discharge Pressure - With and Without Magnets

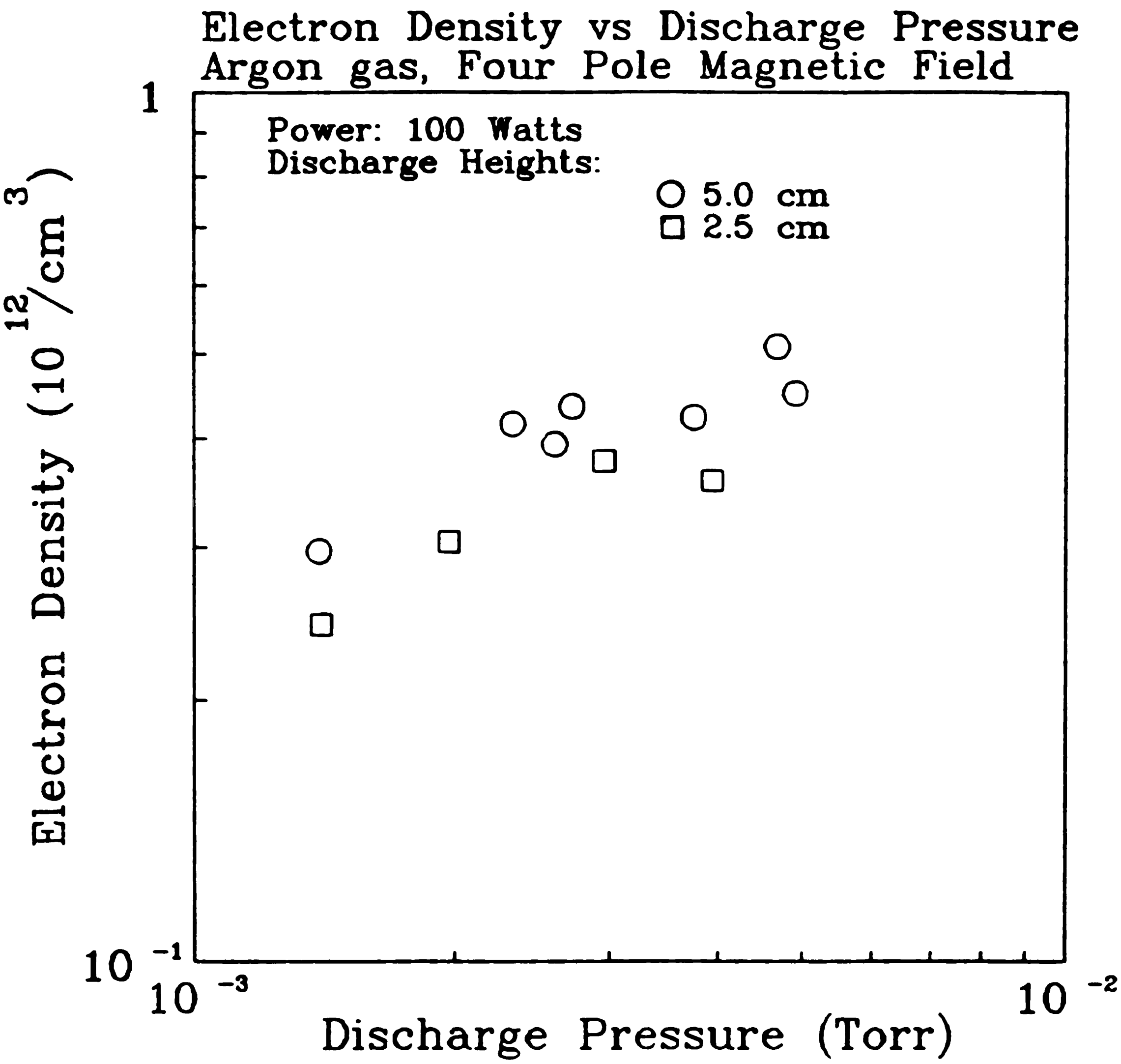

Figure 2.17 Eelctron Density versus Discharge Pressure for Two Discharge Heights

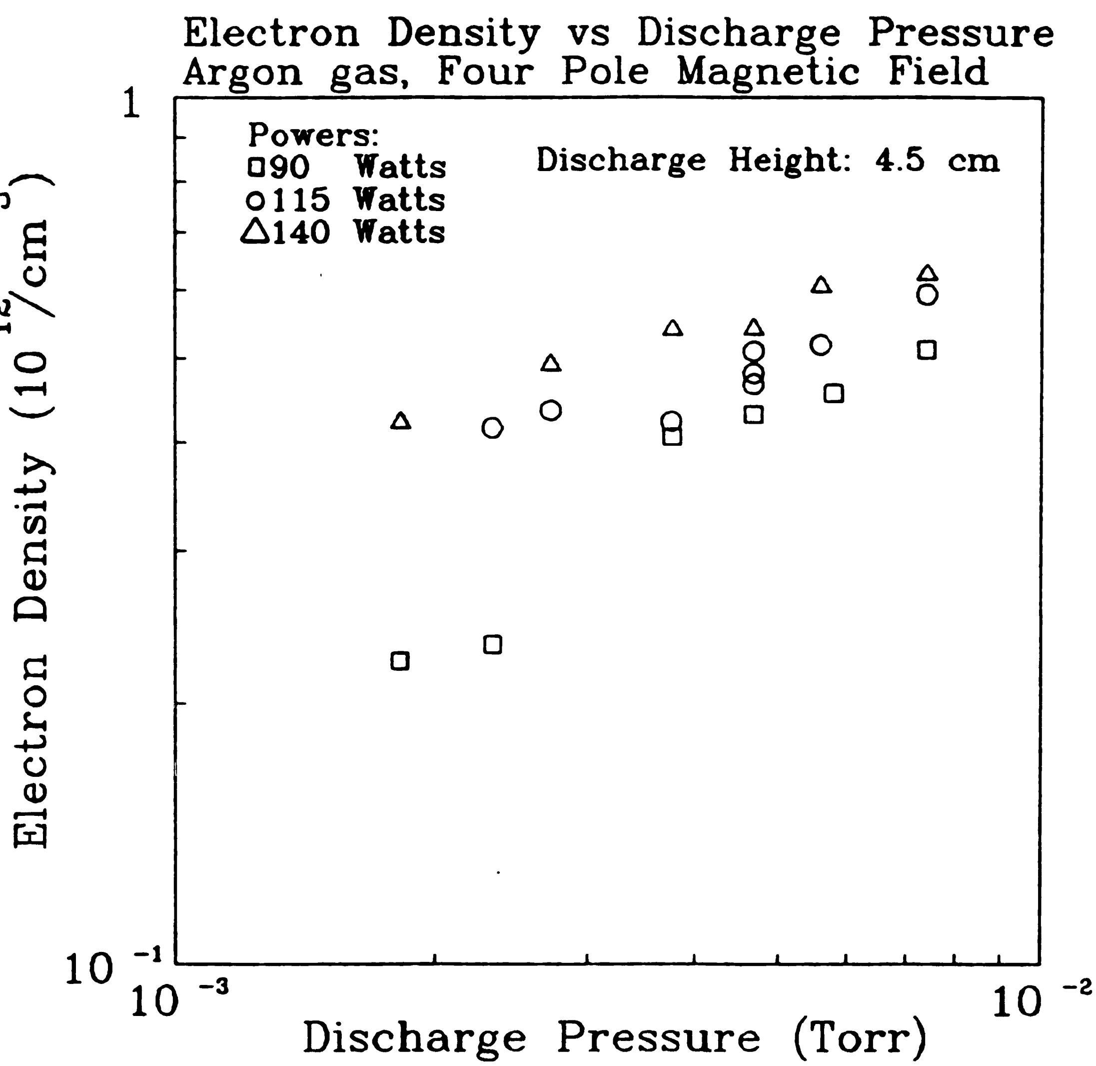

Figure 2.18 Electron Density versus Discharge Pressure
for Various Input Powers

$6x10^{11}/cm^3$ and electron temperatures from 80,000 to 50,000 K. The results are quite promising. Assuming uniform density, Equation (2.9b) may be used to predict the extractable ion current density at the bottom of the discharge. From the data shown in Figure 2.18, the extractable ion current density at the screen grid is about 5 to 20 mA/cm^2.

The Langmuir probe data may be used to find a rough estimate of the power placed into ionization. As will be shown in Chapter 3, the discharge may be modeled by Free-Fall diffusion which assumes that after generation every ion falls through a collisionless discharge to the containing walls. At the walls ions combine with electrons imparting their recombination energy to the wall. Thus in Free-Fall diffusion the recombination power at the discharge boundary is equal to the power put into ionization within in the discharge volume.

In Figure 2.18 density measurements range from $4x10^{11}$ to $6x10^{11}$ $ions/cm^3$ for 140 Watts of input power. Electron temperatures average 55,000 K. Assuming uniform density and temperature, Equation (2.9b) gives an ion current density of 13 to 20 mA/cm^2 to the discharge boundary. The ionization/recombination power is 20 to 31 Watts: the product of the ionization energy for argon, 15.7 eV, and the surface area of the 4.5 cm high discharge, 98 cm^2. By this calculation, less than 25% of the input microwave power goes into ionization.

2.4.3 DOUBLE-GRID BEAM EXTRACTION EXPERIMENTS

Beam extraction was conducted using in argon and oxygen at powers of 70 to 150 Watts and at flows of 1 to 5 sccm. This corresponds to vacuum pressures, P_{bj}, of $2x10^{-2}$ to $7x10^{-2}$ mTorr. (Note: A beam is being extracted from the discharge volume, so discharge pressure can no longer be calculated by means of Equation (2.9)). Figures 2.19 through 2.24 show the results of beam extraction studies for the four-pole samarium-cobalt magnet configuration used in the Langmuir probe experiments of Section 2.4.2. Figures 2.19 and 2.20 show beam current versus power for argon and oxygen for a constant flow and various extraction potentials. As power was increased the beam current raised steadily, but increasing the power by 50% only increased the total beam current by 15 to 20%.

Beam current versus extraction potential and versus flow are shownin Figures 2.21 through 2.24 for argon and oxygen. Contrary to what might be expected from the Langmuir probe density measurements, the beam current generally decreased with increasing flow and discharge pressure. This may be in part due to poor extraction and focusing quality of the grid optics at higher pressures and to charge exchange processes in the beam. The beam current drop is more likely due to the changing diffusion characteristics of the discharge. As the pressure increases, density increases, but depending on the diffusion characteristics of the discharge, charged-particle flux to the grid may decrease.[9] Thus the ion beam current decreases as it is limited by the ion flux density to the bottom of the discharge volume.

From the Langmuir probe measurements of Section 2.4.3, the ion current density available for beam extraction was 10 mA/cm^2. This assumed free-fall diffusion with uniform charged-particle flux. The current density is multiplied by the open area of the screen grid to

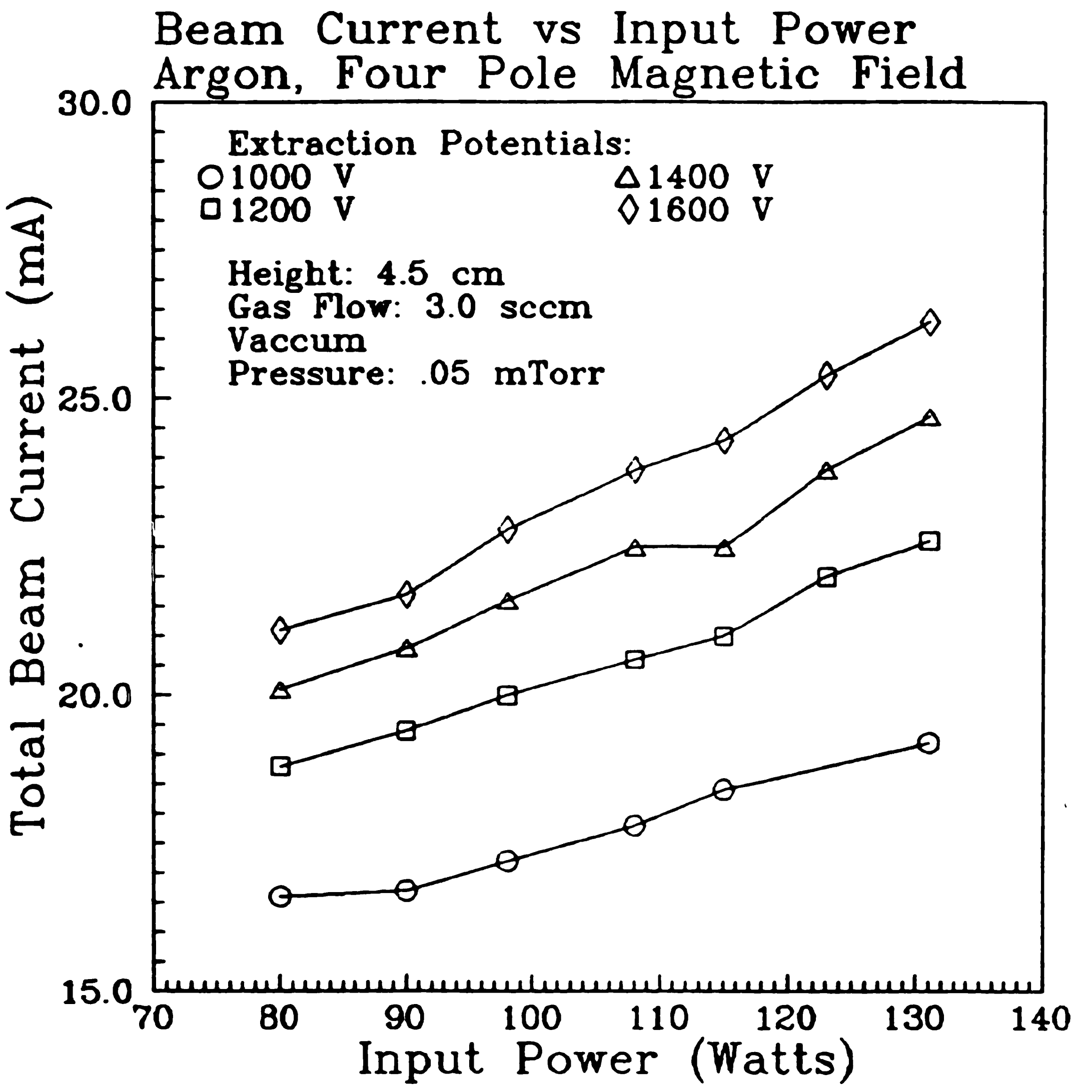

Figure 2.19 Total Beam Current versus Power for Argon - Four-Pole Magnet Configuration

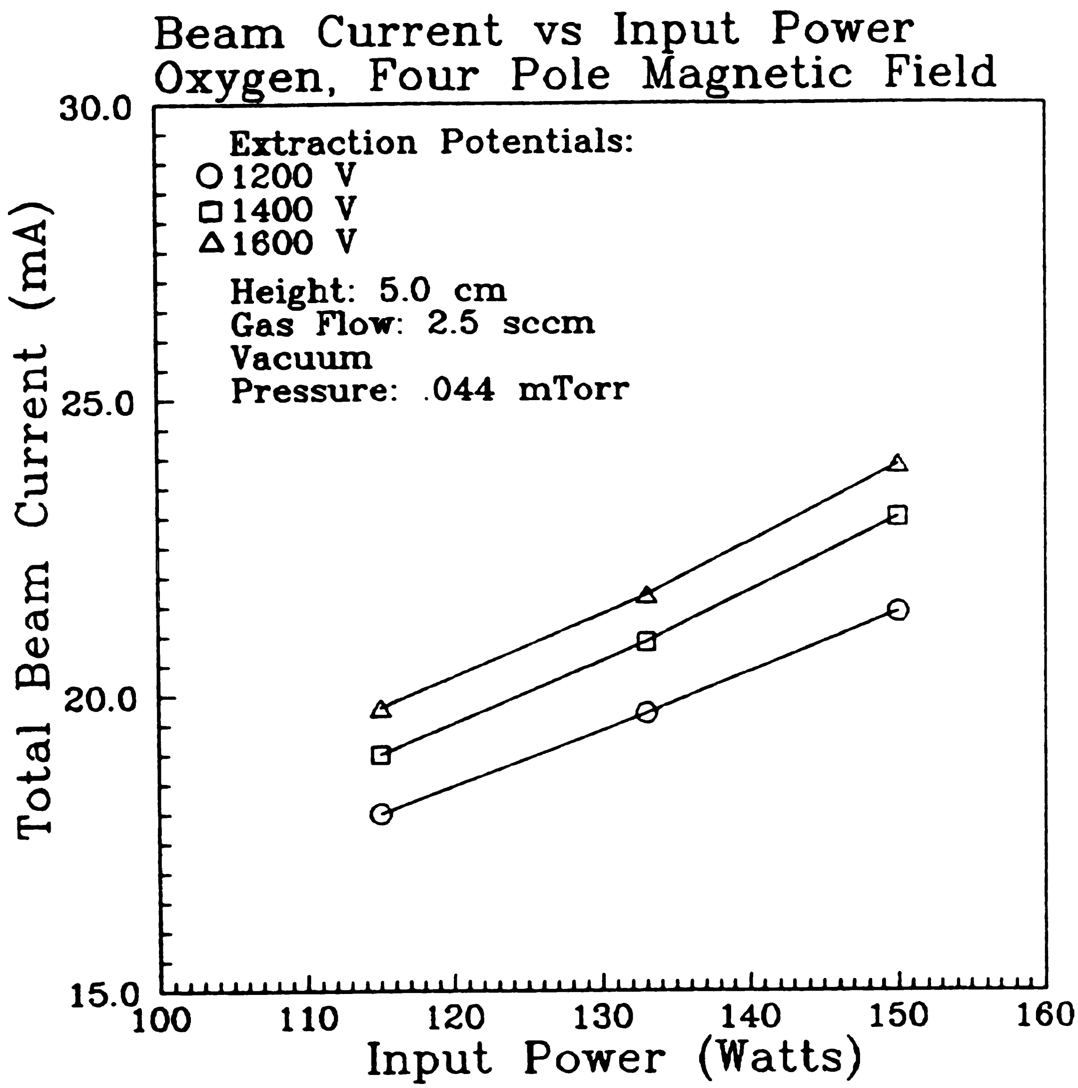

Figure 2.20 Total Beam Current versus Power for Oxygen - Four-Pole Magent Configuration

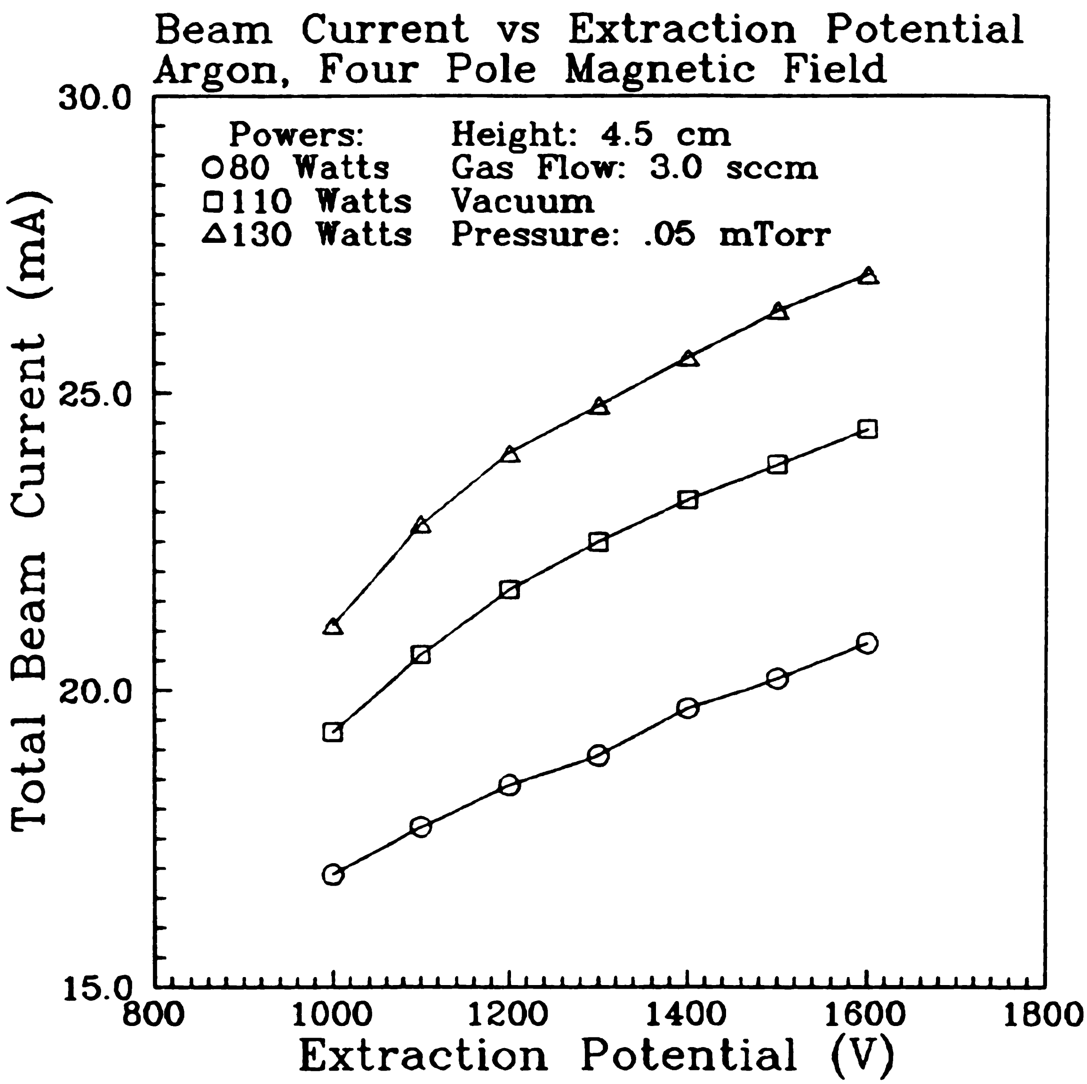

Figure 2.21 Total Beam Current versus Extraction Potential for Argon - Four-Pole Magnet Configuration

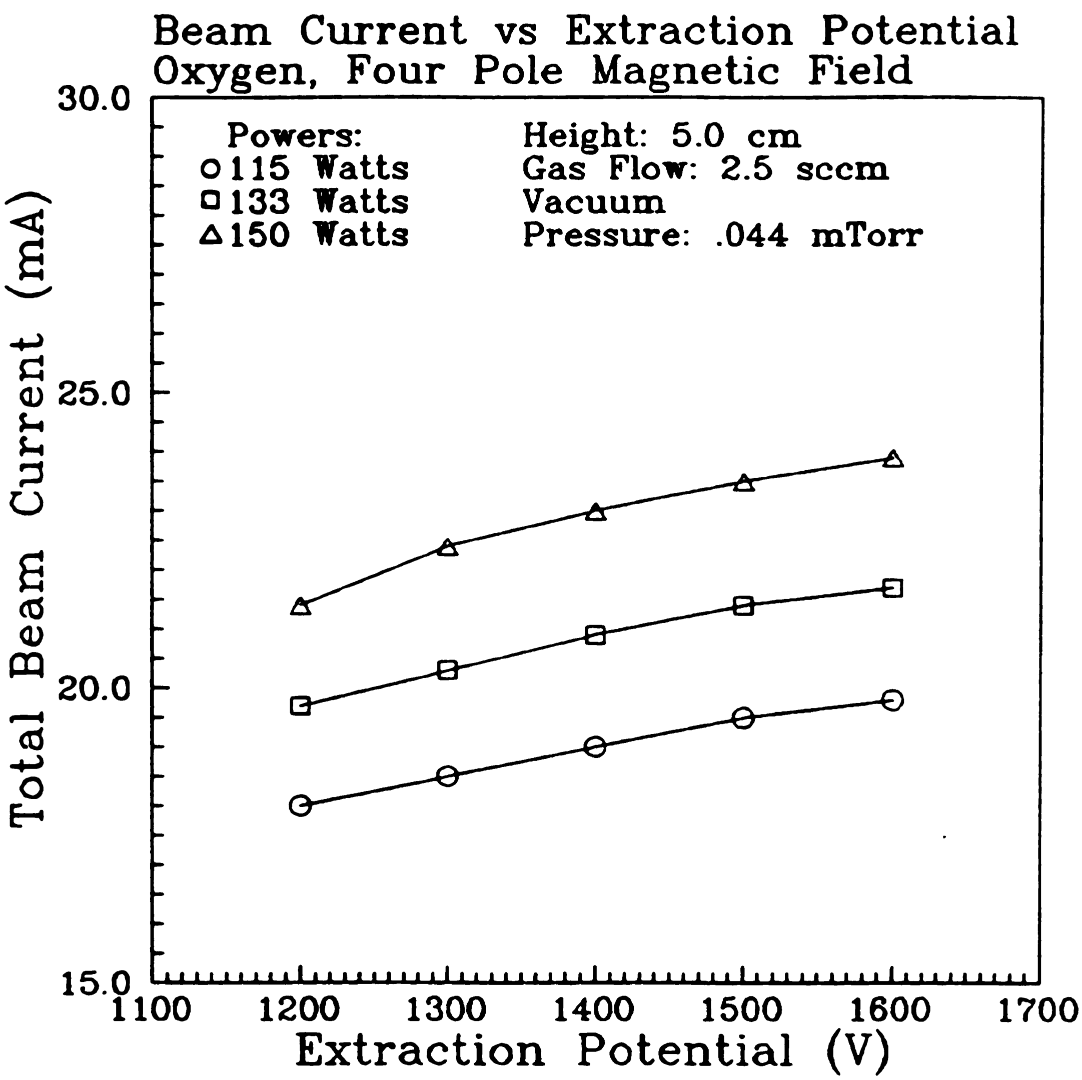

Figure 2.22 Total Beam Current versus Extraction Potential for Oxygen - Four-Pole Magnet Configuration

Total Beam Current (mA)

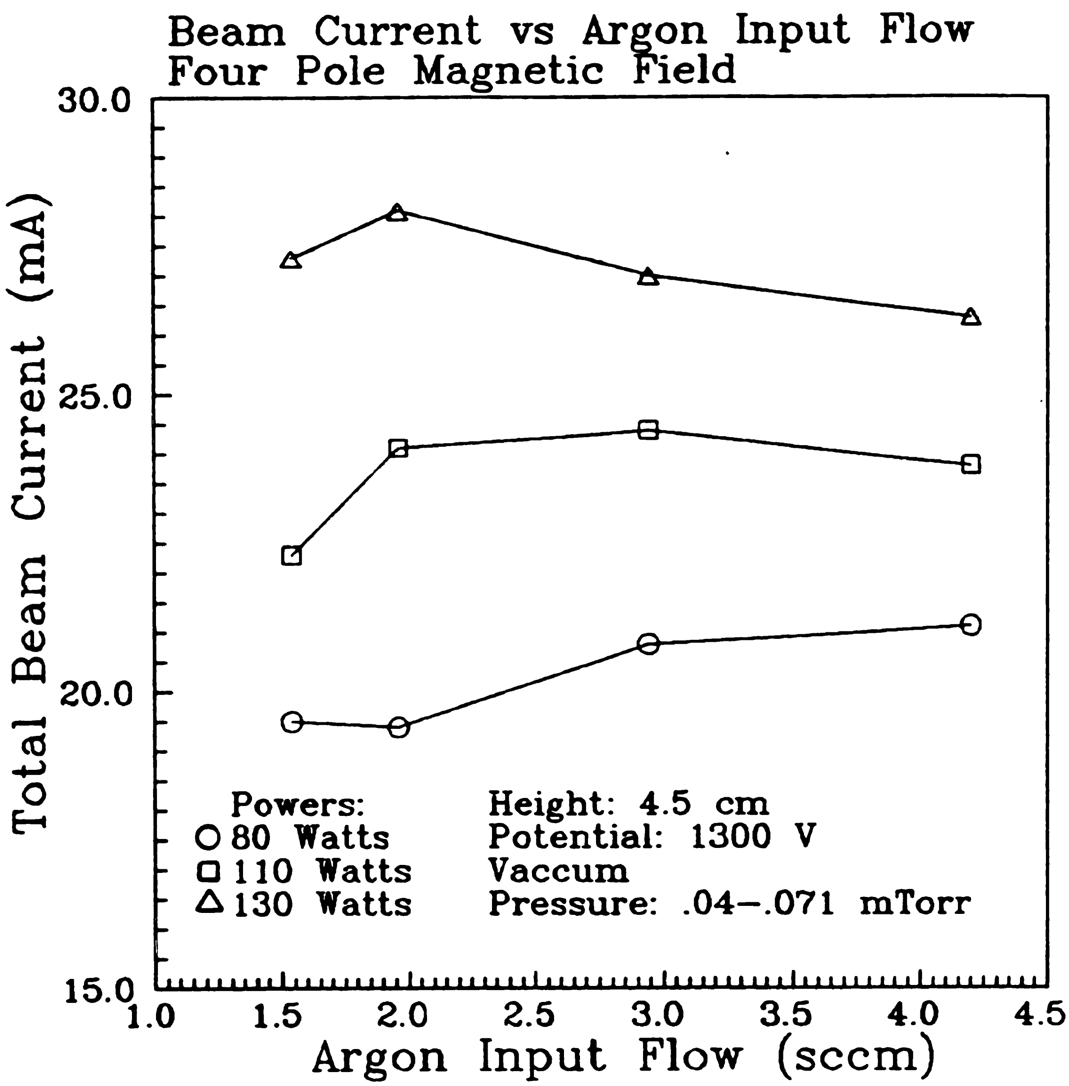

Figuure 2.23 Total Beam Current versus Argon Input Flow – Four–Pole Magnet Configuration

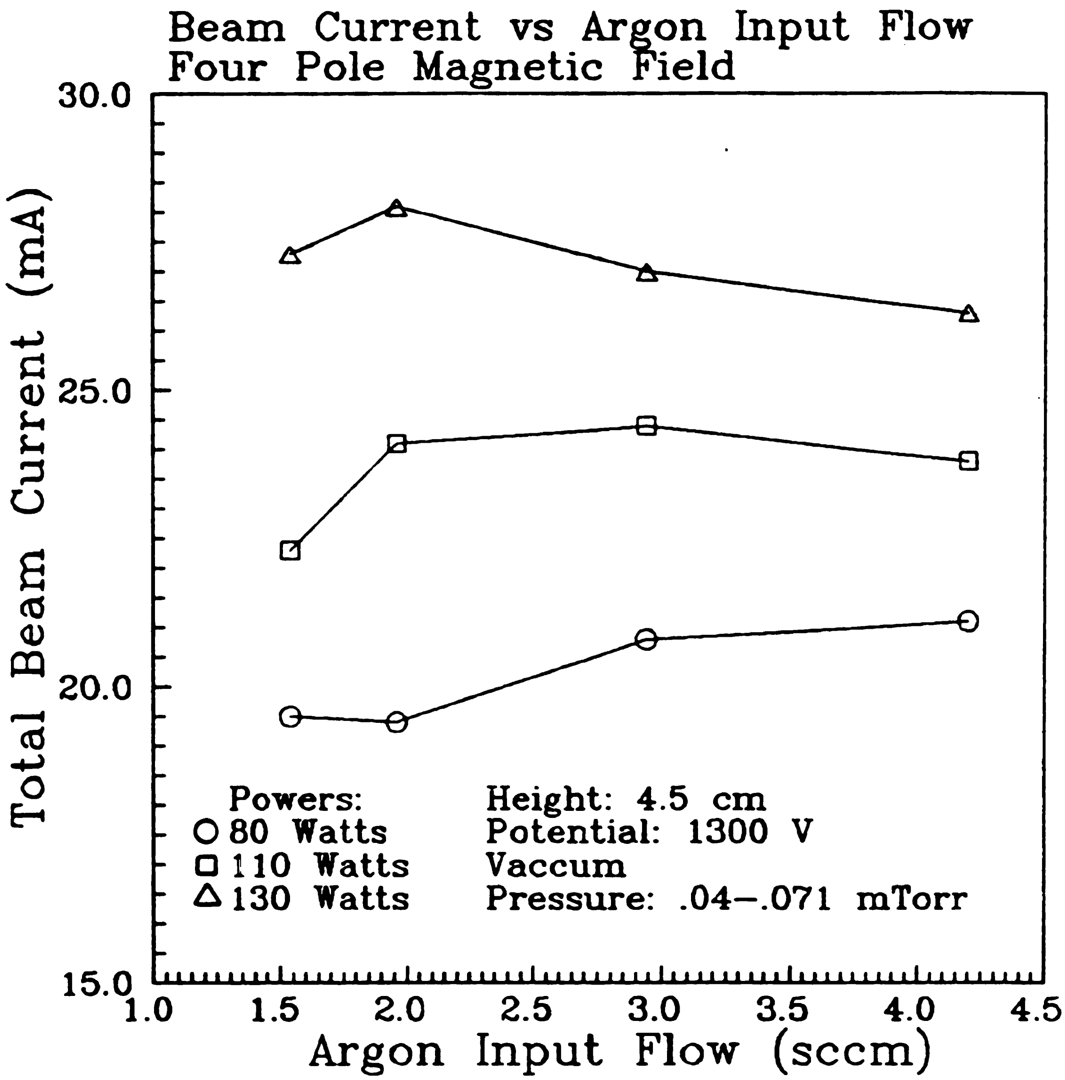

Figuure 2.23 Total Beam Current versus Argon Input Flow - Four-Pole Magnet Configuration

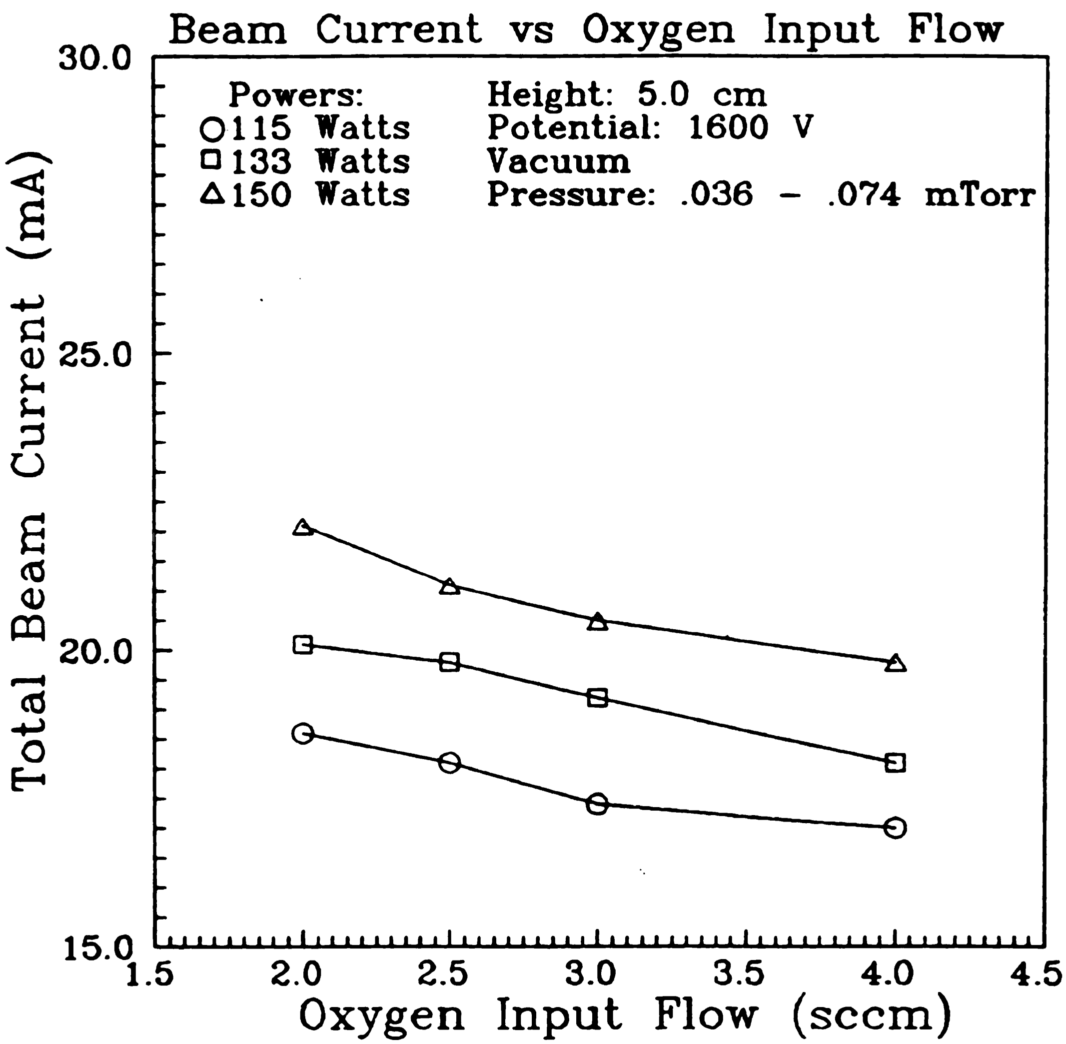

Figure 2.24 Total Beam Current versus Oxygen Input Flow - Four-Pole Magnet Configuration

predict an ion source beam current of 38 mA. This is greater then the actual extracted currents, suggesting that the probe measurements overestimated the charge particle density and/or that the assumptions about free-fall diffusion and ion flux uniformity were inexact. Spatial Langmuir probe measurements could be used to investigate the question of uniformity. Unfortunately this was not done for this early prototype ion source. The low beam currents can also be attributed to poor grid design or alignment.

New permanent magnet configurations were studied with the goal of increasing the discharge density and the beam current. Ten neodymium-iron-boron magnets were used in an alternating-pole configuration about the discharge as previously shown in Figure 2.2. The magnets have the same dimensions as the samarium-cobalt magnets, 1.3 x 1.3 x .5 cm, but have a greater face field strength of 3.5 kGauss. Figure 2.25 shows a B-field plot of the ten magnets measured with a Hall-effect probe. The 875 Gauss ECR zones are a few millimeters within the quartz wall but are occasionally broken between poles faces by the quartz boundary. When these stronger magnets were used in beam extraction studies beam currents were increased by as much as 30%.

Figures 2.26 through 2.31 show beam currents extracted from argon, oxygen and nitrogen discharges with the ten-pole configuration. Figures 2.26 through 2.28 show the the results for argon. Although the power was pushed past 150 Watts to 170 Watts, the current density exceeded 38 mA. Figure 2.29 shows beam current versus argon flow. The profiles of these curves appear erratic in some instances. This behavior can be attributed to two causes. First, the beam current

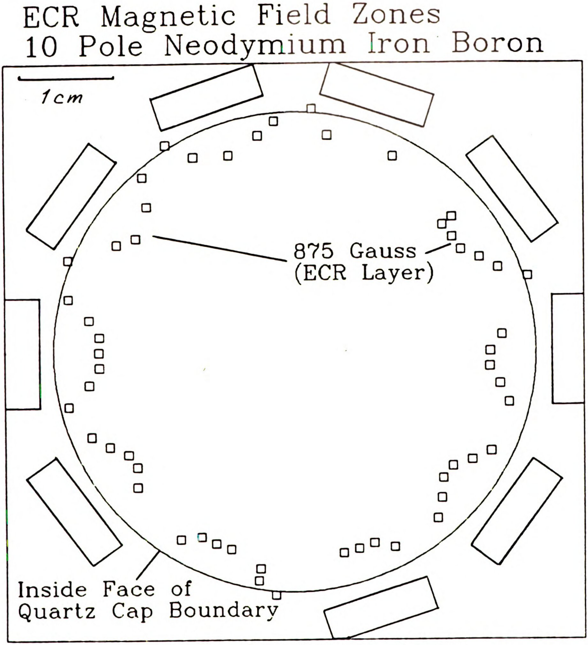

Figure 2.25 ECR Zones for a Ten-Pole Neodymium-Iron-Boron Magnet Configuration

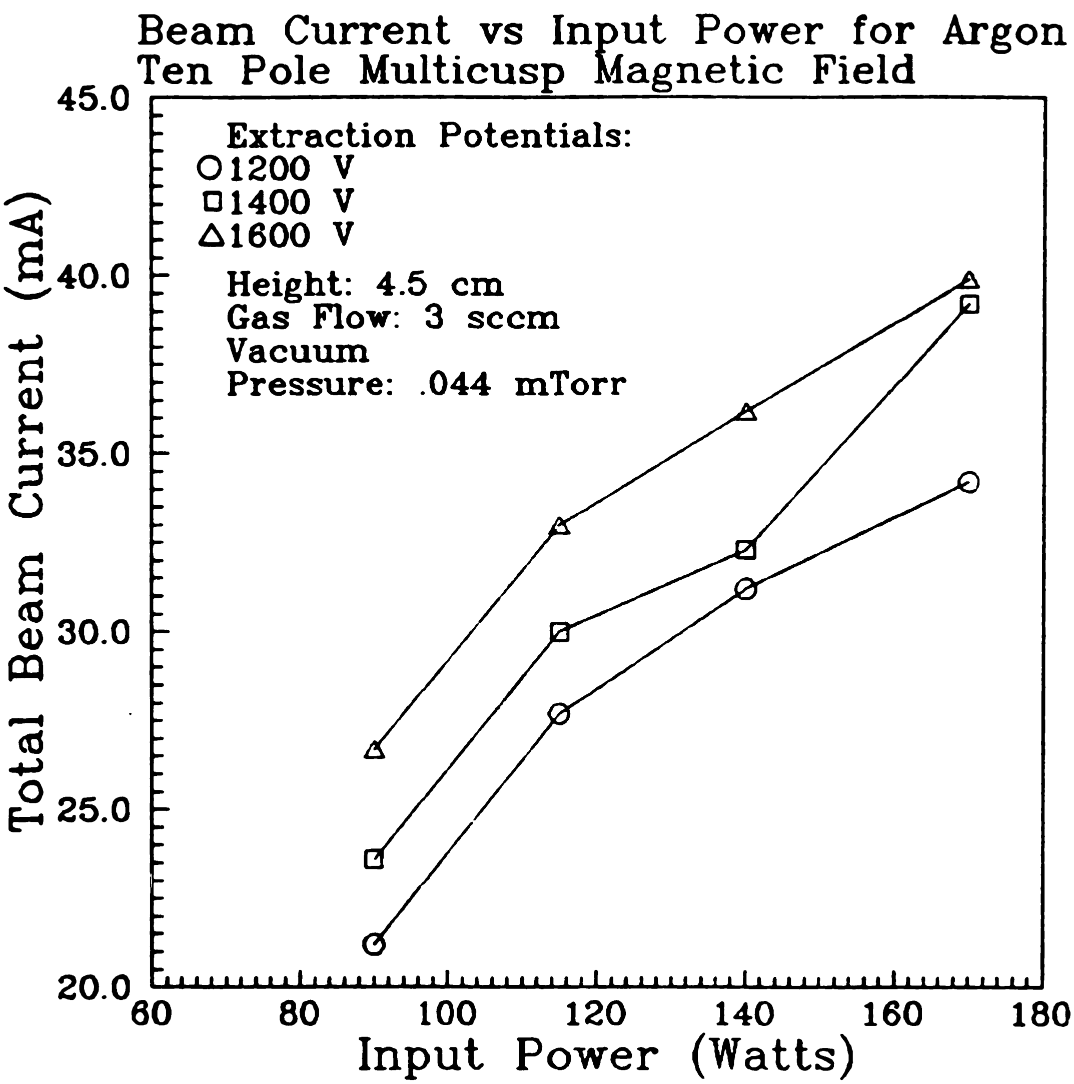

Figure 2.26 Total Beam Current versus Power for Argon - Ten-Pole Magnet Configuration

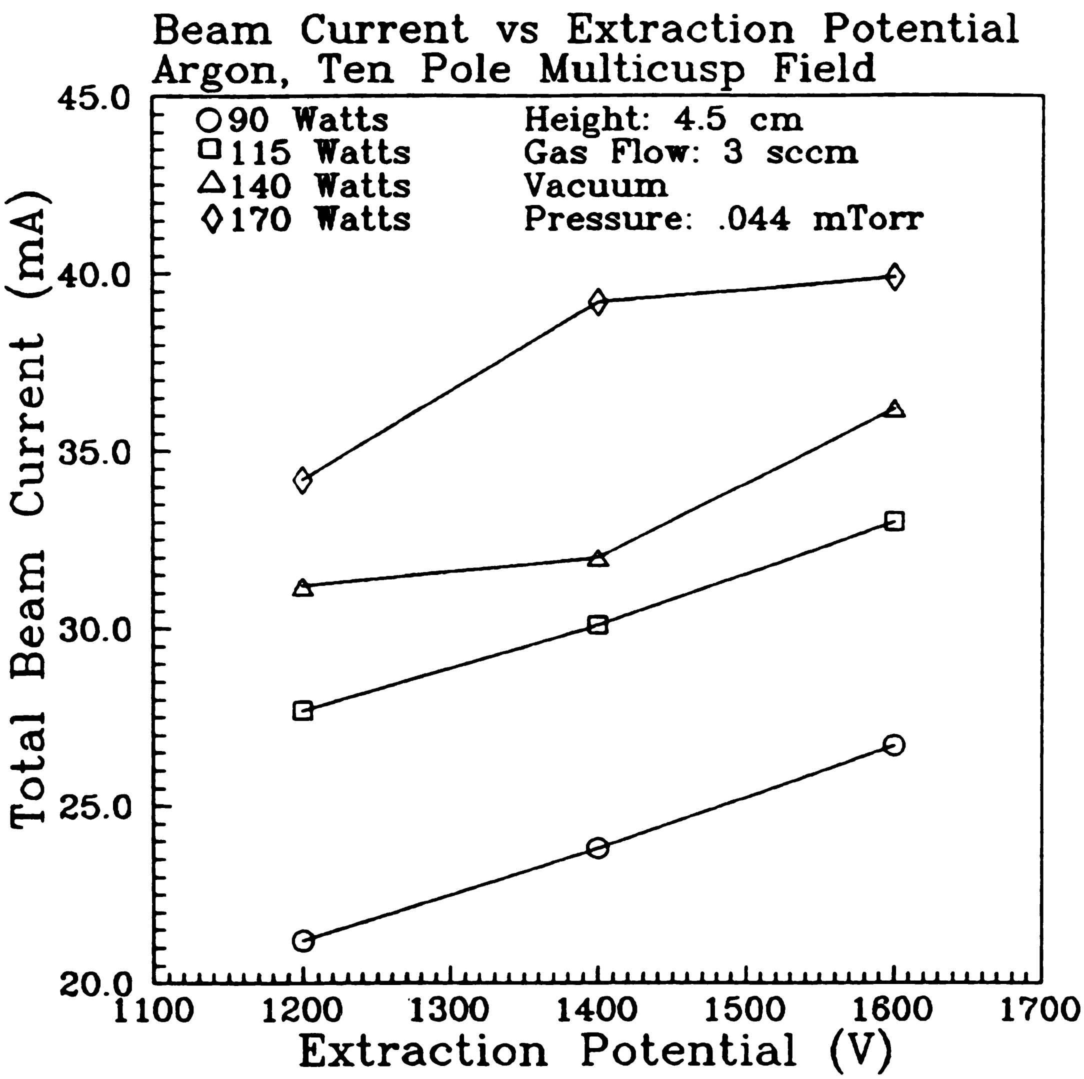

Figure 2.27 Total Beam Current versus Extraction Potential for Argon - Ten-Pole Magnet Configuration

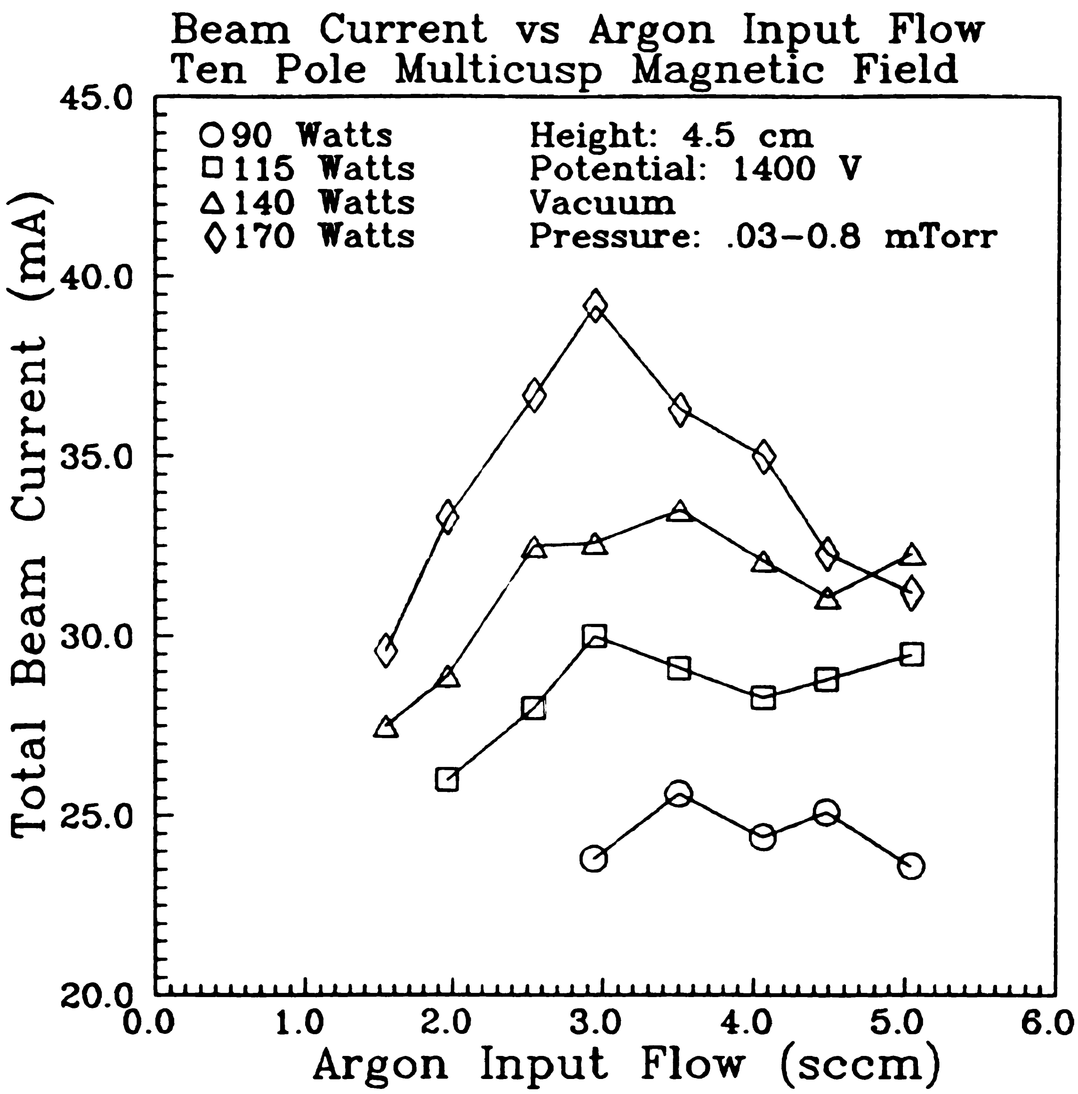

Figure 2.28 Total Beam Current versus Argon Input Flow - Ten-Pole Magnet Configuration

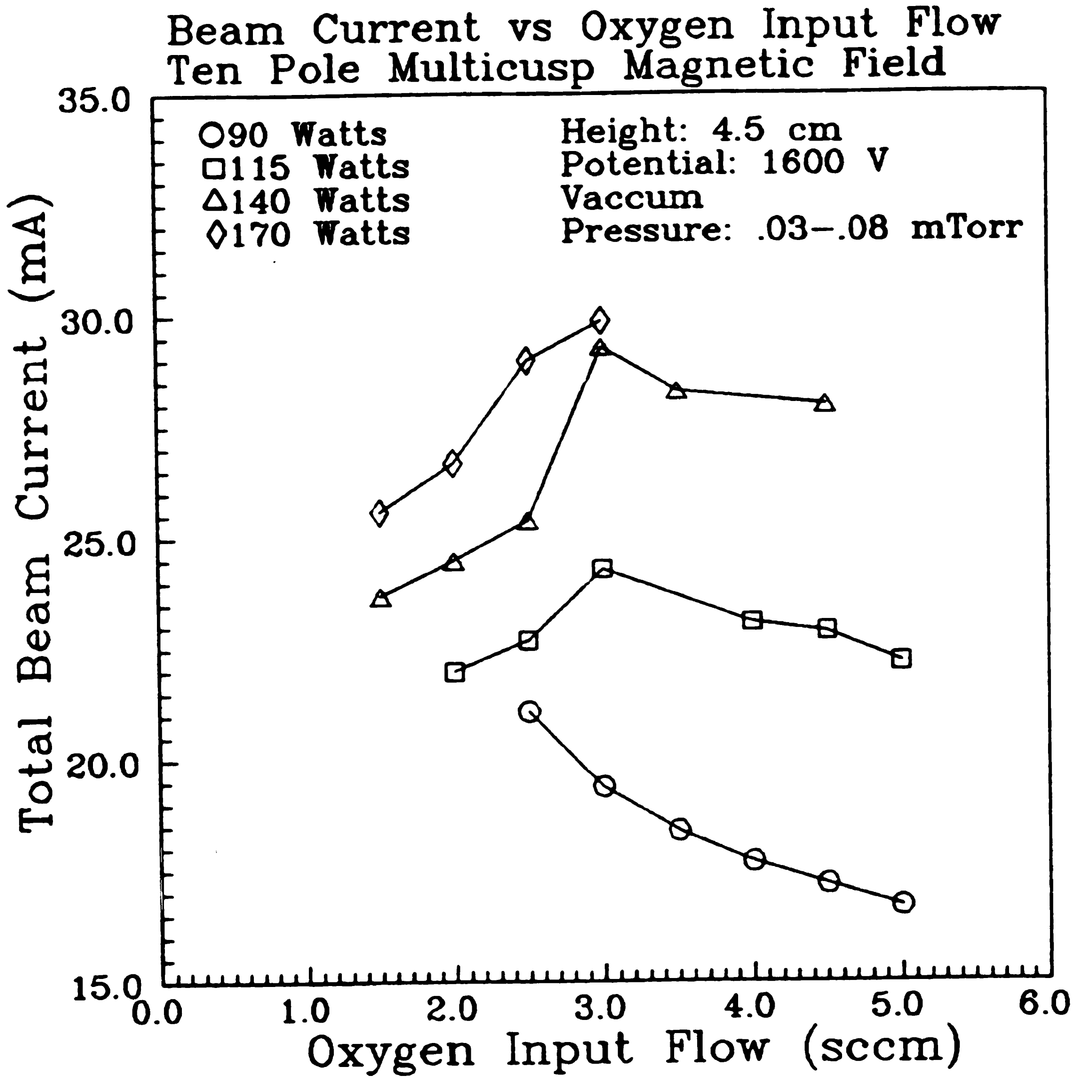

Figure 2.29 Total Beam Current versus Oxygen Input Flow - Ten-Pole Magnet Configuration

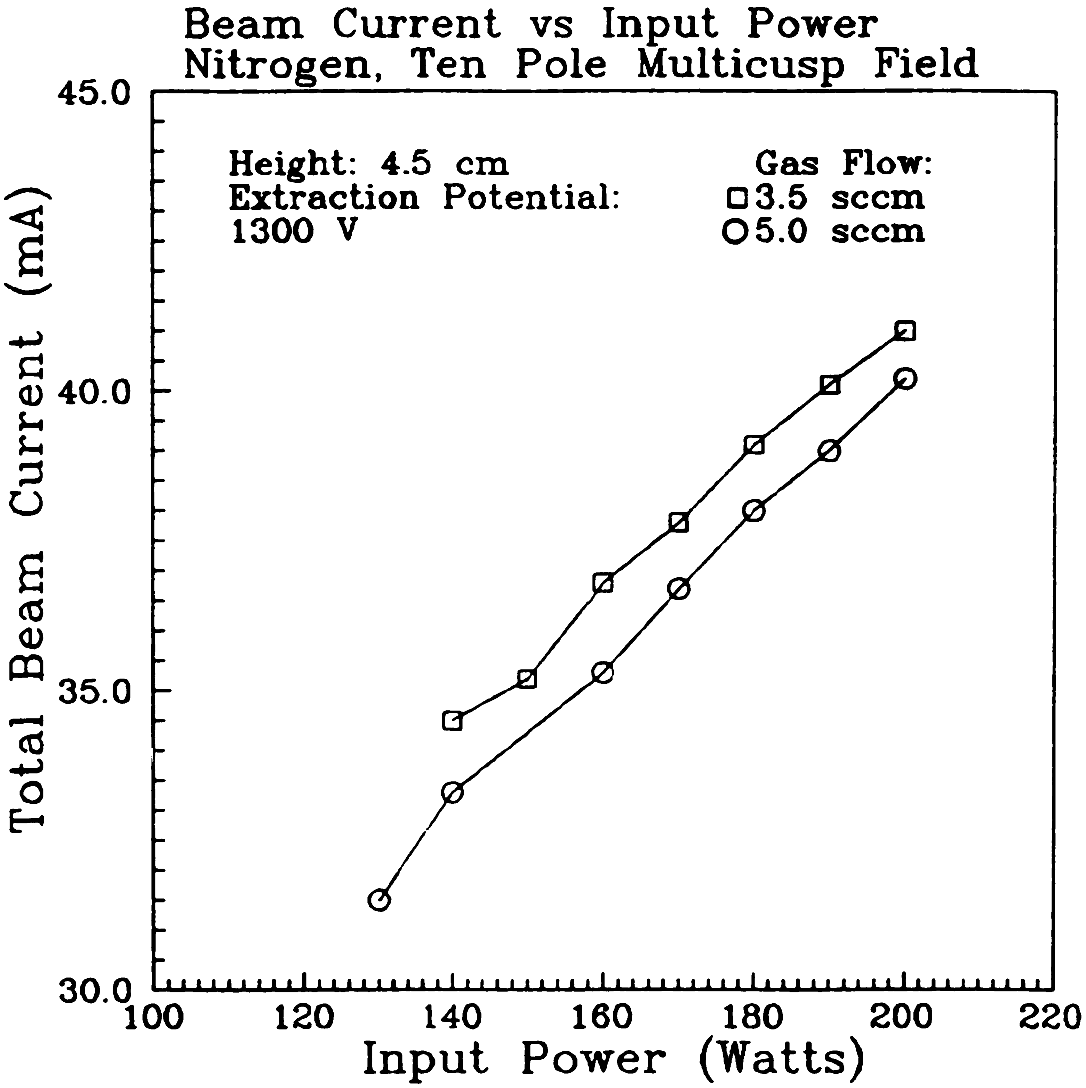

Figure 2.30 Total Beam Current versus Power for Nitrogen - Ten-Pole Magnet Configuration

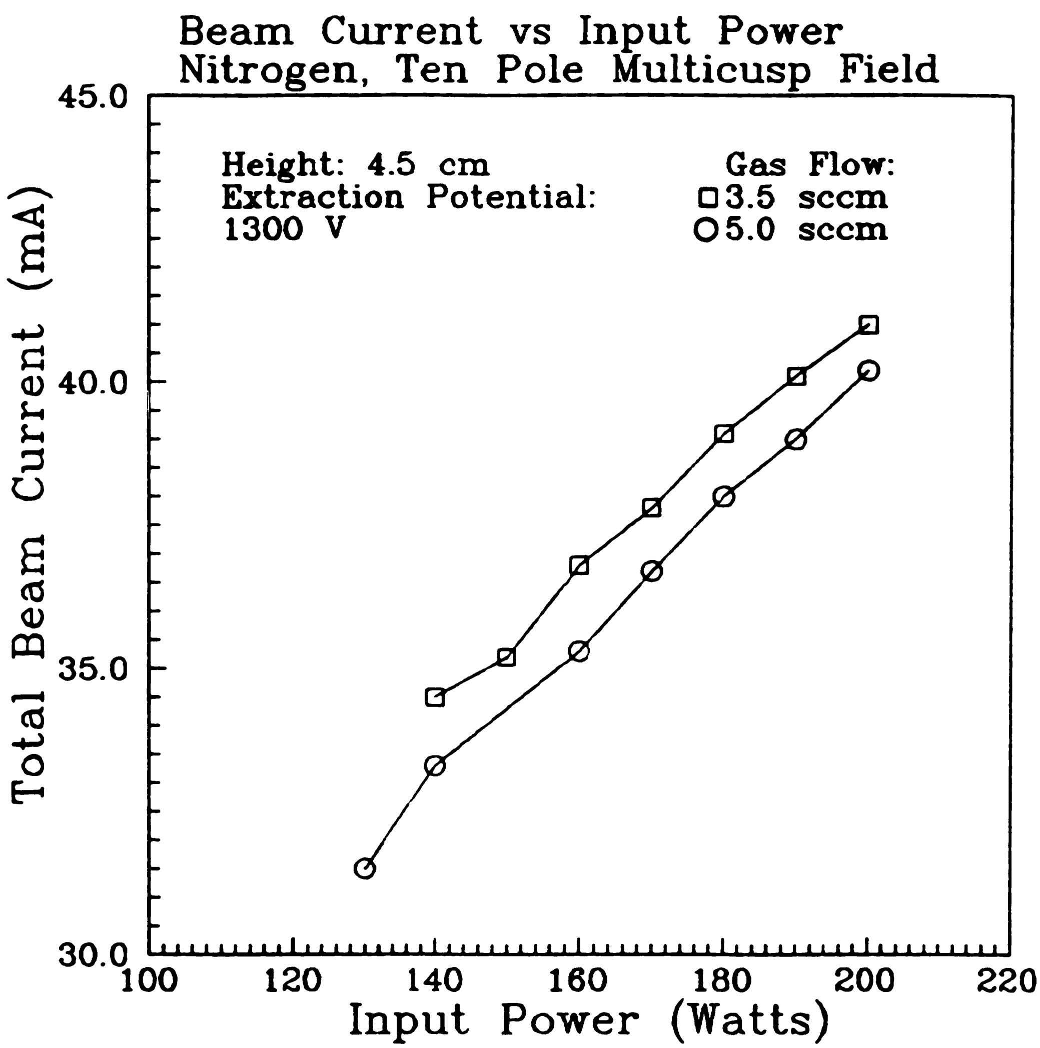

Figure 2.30 Total Beam Current versus Power for Nitrogen - Ten-Pole Magnet Configuration

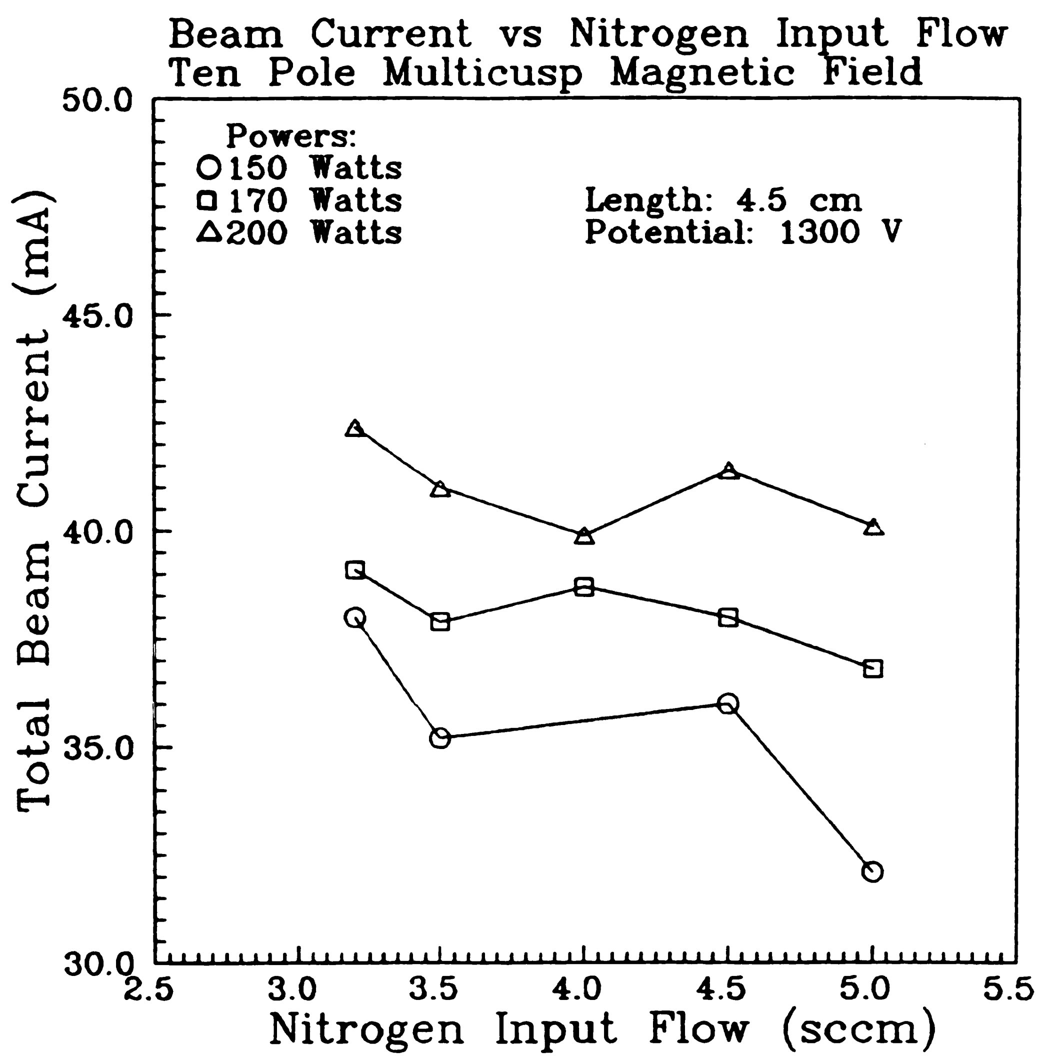

Figure 2.31 Total Beam Current versus Nitrogen Input Flow - Ten-Pole Magnet Configuration

magnitude and focusing is strongly dependent upon small adjustments in the acceleration grid potential (tens of volts). The grids were designed for discharge densities below $10^{11}/cm^3$ and may not be able to accommodate the high ion current densities. Second, it was observed that at low discharge pressures, there appeared to be two zero-reflected-power tuning points attributed to the TE_{111} resonant mode. One of these tuning points produced a less dense discharge, and during experiments it was not uncommon to slip between the two modes while adjusting power, flow or tuning lengths.

Figure 2.29 through 2.31 show extraction data for oxygen and nitrogen. Oxygen beam current densities rose by 30 to 40% with the new magnet configuration. Nitrogen reached beam currents in excess of 40 mA when the power was pressed to 200 W.

Although the neodymium-iron-boron magnets with the ten-pole configuration produced high beam current densities, their placement within the cavity near the hot quartz wall posed some difficulties. The Curie point of the neodymium-iron-boron magnets is around 100 °C and the intense heat of the quartz wall thermally damaged the magnets until essential portions of the ECR zone were lost. As the static magnetic field deteriorated, ion densities dropped and consistent experimental results were difficult to obtain beyond a few hours of operation.

In addition to magnet heating, the open magnet configuration itself produces an unfavorable perturbation in the cavity and reduces the cavity quality, Q. The magnets also form a conducting wall around the discharge that in effect shields it from the microwaves. The neodymium-iron-boron magnets are favored for their strength, but if they are used in future ion source designs, they must be thermally protected from the discharge and placed outside of the resonant cavity volume.

2.4.4 SINGLE-GRID EXTRACTION

Single-grid extraction at 50 to 100 Volts was attempted with the ten-pole neodymium-iron-boron magnet configuration. The silicon grid and screen grid optics discussed in section 2.3.4.2 were both fitted to the ion source. Ion beam current densities measured by a Faraday cup 5 cm below the silicon grid optics were very low, a few micro-amps/cm^2. Visually there was no shaft of illumination indicative of excitation associated with an extracted beam. The same observations were made for a 25 x 25 lines per inch, 40 % transparent stainless steel screen grid.

It is apparent that a broad beam could not be extracted with the silicon grid or screen grid optics. Both single-grid optics have open hole apertures which were too wide for the density of this discharge. As the density of a discharge becomes larger, the shielding Debye length and the plasma sheath become smaller, (the plasma sheath may be several Debye lengths). As mentioned in Section 2.3.4.2, extraction from single-grid optics is dependent upon the formation of the plasma sheath next to the grids. Here the sheath distance, .05 to .1 mm, was small compared to the hole size of the extraction optics, .7 to .5 mm, the charged particles diffused through the grids, and ions were not accelerated or focused. The specifications for single-grid optics will be dissussed in Chapter 4.

2.5 SUMMARY OF THE MICROWAVE-CAVITY ION SOURCE PERFORMANCE: PROTOTYPE I

At the outset of this chapter, one of the intentions was to improve the power cost factor for the 3.2 cm diameter set of extraction grids. See Equation 2.1. Using the beam current versus power data for argon from Figure 2.27, the power cost versus input power has been plotted in Figure 2.32. The power cost ranged from 3600 to 5000 Watts/Beam Amp which was an improvement by a factor of two over Dahimene's application of the same extraction optics. This was expected as the discharge radius and volume was reduced from 9.4 cm to 4.9 cm to more efficiently accommodate the beam extraction area.

A number of changes can be made to improve the experimental prototype. The most important change is to embed the magnets within the base plate assembly and to water cool and air cool the magnets as done in other early microwave-cavity plasma source designs.[9,10,14] The physical size of the ion source can be reduced to decrease the weight and material of the instrument. The cavity shell diameter can be reduced. The input probe can be scaled down to handle just the 200 Watts necessary to drive the discharge. Also the sliding short mechanisms can be simplified and improved.

The operating lifetime of this electrodeless ion source depends on the integrity of three components. The first is the extraction optics

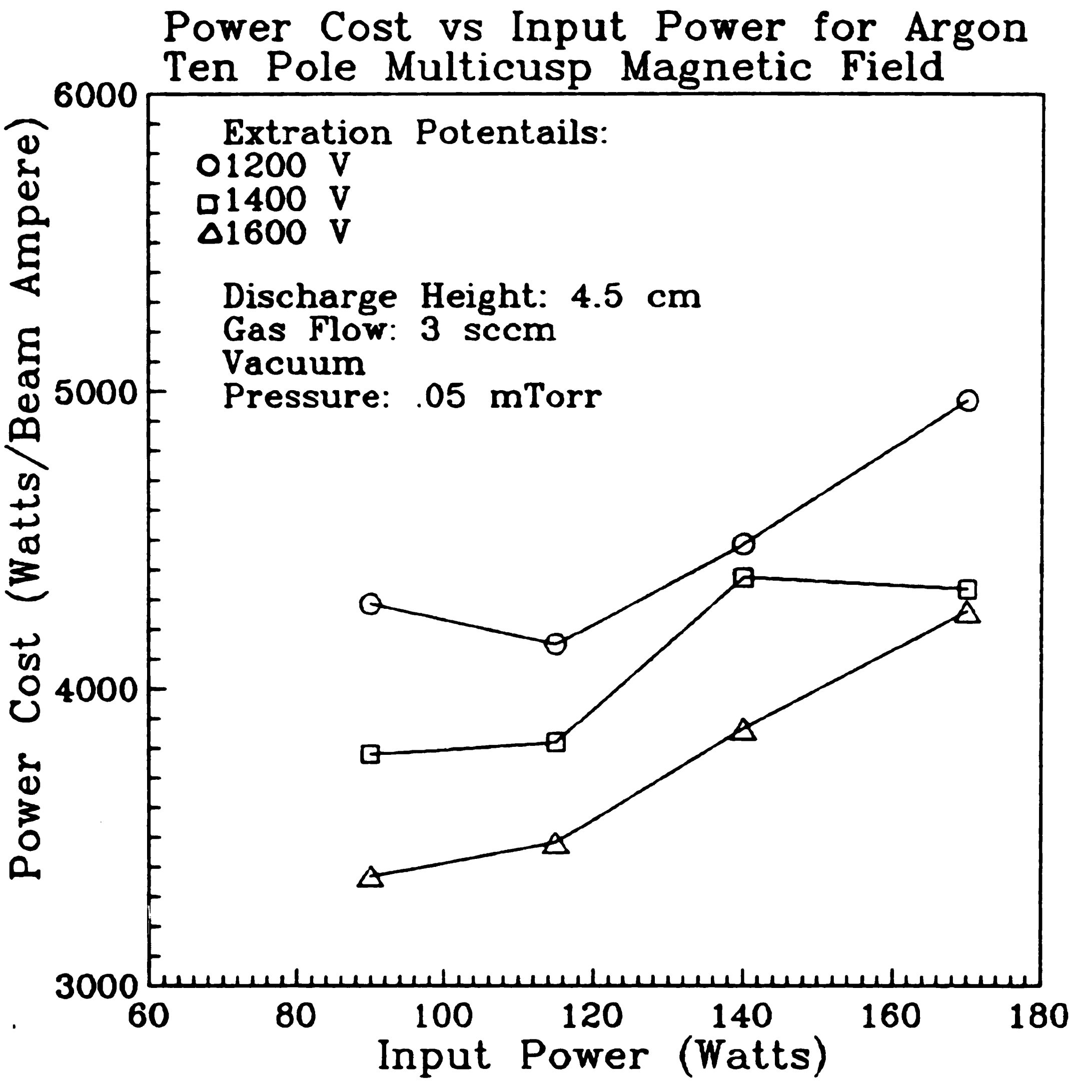

Figure 2.32 Power Cost versus Input Power for Nitrogen - Ten-Pole Magnet Configuration

which are eroded away by accelerated ion bombardment. This is the nature of all electrostatic extraction grids and is a common limitation of all ion sources using grids.[40,44] The second component is the rubber silicone seal which thermally disintegrates at points where it is exposed to the hot discharge and the strong electric fields of the microwaves.[39] Careful redesign of the base plate cooling lines, placement of an O-ring channel, and re-configuration of the quartz cap seating may stop this damage of the vacuum seal. The third component is the heating of permanent magnets. If the latter two problems can be solved by design changes, the working lifetime of the ion source will be limited only by the extraction optics.

As clearly demonstrated in single-grid extraction experiments, single-grid optics must be redesigned to accommodate high ion current densities. Indeed the same should be done for double-grid extraction optics.

As demonstrated by these experiments, a compact, ECR microwave-cavity ion source can produce high ion current densities, $10 mA/cm^2$, with less than 200 Watts of input microwave power. The resulting beam currents from a 3.2 cm diameter, 47% transparent extraction grid are comparable to conventional DC ion source technology.[40,45,46] However the microwave ion source has the advantage in that it uses no electrodes and thereby has a long working lifetime in reactive gases such as Oxygen.

CHAPTER 3
SIMPLE PLASMA DIFFUSION MODELS

3.1 INTRODUCTION

The analysis of simple diffusion models of a plasma body can yield information about the behavior of low-pressure discharges that may in turn help to improve ion source operation and design. In this chapter, two low-pressure diffusion models, Schottky diffusion and free-fall diffusion, are reviewed and applied to the microwave discharge problem. The models are used in conjunction with the plasma power balance equation to predict the amount of power put into ionization processes during steady state operation. It should be emphasized that this analysis is not exact. Many assumptions and simplifications have been made, yet the analysis has merit as it provides basic understanding of charged particle diffusion and density distributions and can be used to roughly predict the amount of microwave power necessary to operate the ion source.

3.2 DIFFUSION MODELS

3.2.1 SCHOTTKY AND FREE-FALL DIFFUSION

At low pressure there are two diffusion models of interest. The first is Schottky diffusion where volume collisions and space-charge effects govern charged-particle diffusion and control the discharge density distribution. The second is free-fall diffusion. In free-fall diffusion volume collisions are negligible. The mean free path of charged particles is greater than the dimensions of the containing vessel, and, after ionization, charged particles move freely through the discharge. The resulting discharge density distribution is uniform. A discharge can be described by either diffusion model depending on the operating pressure and dimensions of the containing vessel.

In this section Schottky and free-fall diffusion models are applied to a disk-shaped, argon discharge. Physical parameters such as discharge dimensions and pressure are plotted against the predicted electron temperature required to maintain a discharge. The diffusion theories are tested against experimental measurements of electron temperature. (See Section 2.3.3.)

3.2.2 PHYSICAL ASSUMPTIONS

The objective in this theoretical development is not to devise exact models. Only qualitative information is sought to anticipate operating performance of the prototype ion source. In order to keep the models simple, a number of assumptions must be made about the discharge. First, the electrons, ions and neutral gases have a spatial uniform, Maxwellian energy distribution and thus uniform, isotropic temperatures, T_e, T_i, and T_n. Second, ion and electron densities are equal throughout the plasma volume, except within the plasma sheath. Third, all boundaries are perfectly absorbing and thus all ion/electron recombination energy is absorbed by the walls. Fourth, only single stage ionization is considered. Finally, there are no DC magnetic fields within the discharge.

Many of these assumptions oversimplify the discharge as the experimental ion source discharge is gyrotropic, anisotropic, non-Maxwellian, and is sustained by microwave electromagnetic fields. Yet, as will be shown, a comparison of experimental data with simple diffusion theories will yield information useful for design purposes.

3.2.3 SCHOTTKY DIFFUSION MODEL

Schottky diffusion in a cylindrical column is a classic problem[47] and has been discussed in detail in many texts.[48-50] In the context of microwave plasma studies, Dahimene[9] presented a special treatment of the Schottky diffusion model for a disk-shaped discharge. Rather than restate the derivation of Dahimene's model from first principles, the basic diffusion equation will be given here and then expanded. The equation for Schottky diffusion is given as

$$\nabla^2 n + \frac{\nu_i}{D_a} n = 0 \tag{3.1}$$

where ν_i is the ionization collision frequency, D_a is the Schottky diffusion constant and $n = n_e = n_i$ is the charged-particle density distribution. Equation (3.1) may be solved for a finite-length cylinder by a separation of variables to obtain

$$N(r,z) = N_o\ J_o(\beta_o r)\ \cos(\alpha z) \tag{3.2}$$

with $\alpha = \pi/l$ and $\beta_o = 2.405/r$ and

$$\frac{\nu_i}{D_a} = \left(\frac{1}{\Lambda}\right)^2 = \left(\frac{2.405}{r}\right)^2 + \left(\frac{\pi}{l}\right)^2 . \tag{3.3}$$

Here r and l are the radius and length of the discharge respectively. The separation constant, Λ, is defined as the characteristic diffusion length for Schottky diffusion in a disk discharge. The solution to the above expression assumes that the zeroth-order Bessel function adequately characterizes the radial density profile. In certain cases several orders of Bessel functions may be required in the solution to Equation (3.1).[14]

In typical low-pressure laboratory plasmas (<50 Torr), the electron temperatures are much higher than ion temperatures, $T_e \geq 10{,}000$ K and

$T_i \cong 350$ K. This allows us to simplify the expression for the diffusion coefficient D_a.

$$D_a = \frac{\mu_i D_e + \mu_e D_i}{\mu_e + \mu_i} \tag{3.4}$$

$$D_e = (k_b T_e \,/\, m_e\, \nu_{em}) \qquad\qquad D_i = (k_b T_i \,/\, M_i\, \nu_{im})$$

Above μ_i and μ_e are ion and electron mobilities, and ν_{im} and ν_{em} are the ion and electron collision frequencies for momentum transfer. The mobilities are expressed as

$$\mu_i = e/\, M_i \nu_{im} \qquad \text{and} \qquad \mu_e = e/\, m_e \nu_{em}$$

where e is the electron charge, and M_i and m_e are the ion and electron masses. With $T_e \ll T_i$, (3.4) can be reduced to

$$D_a \cong \mu_i D_e \,/\, \mu_e = (\mu_i k_b T_e)/\, e\ . \tag{3.5}$$

Combining (3.3) and (3.5), the ionization frequency can be expressed as

$$\nu_i = (\mu_i k_b T_e) \,/\, (e\ \Lambda^2)\ . \tag{3.6}$$

Equation (3.6) specifies the ionization frequency in terms of electron temperature, ion mobility and discharge geometry.

The ionization frequency can be calculated from electron collision cross sections, $\sigma_i(v_e)$, electron temperature, T_e, and neutral gas density, N.

$$\nu_i = N \cdot \langle \sigma_i(v_e) \cdot v_e \rangle \tag{3.7}$$

where v_e is the electron velocity. The ionization rate for any velocity distribution of electrons in the plasma is

$$\langle \sigma_i(v_e) \cdot v_e \rangle = \int_0^\infty \sigma_i(v_e)\ v_e\ f(v_e)\ dv_e \tag{3.8}$$

and for a Maxwellian distribution is

$$\langle \sigma_i(v_e) \cdot v_e \rangle = 4\pi \left(\frac{m_e}{2\pi k_b T_e} \right)^{3/2} \cdot \int_0^\infty \sigma_i(v_e)\ v_e^3 \exp\left(\frac{-m_e v_e}{2k_b T_e} \right) dv_e\ . \tag{3.9}$$

Substituting $v_e = (2\varepsilon/m_e)^{1/2}$ and $dv_e = d\varepsilon/(2\varepsilon m_e)^{1/2}$, the above expression may be written in terms of electron energy, ε, where ε_i is the ionization energy:

$$\langle \sigma_i(\varepsilon) \cdot v_e(\varepsilon) \rangle = 4\pi \left(\frac{m_e}{2\pi k_b T_e} \right)^{3/2} \cdot \int_{\varepsilon_i}^\infty \sigma_i(\varepsilon) \frac{1}{\sqrt{2\varepsilon m_e}} \left(\frac{2\varepsilon}{m_e} \right)^{3/2} e^{(-\varepsilon/k_b T_e)}\ d\varepsilon \tag{3.10}$$

The above expression is most convenient as empirical collision cross sections are typically expressed as a function of electron energy. The collision frequency for any collision cross section and Maxwellian electron sub-gas with electron temperature T_e is given as

$$\nu_i = N \left(\frac{2\sqrt{2}}{(\pi m_e)^{1/2} (k_b T_e)^{3/2}} \right) \int_{\varepsilon_i}^{\infty} \varepsilon \cdot \sigma_i(\varepsilon) \cdot \exp(-\varepsilon / k_b T_e) \, d\varepsilon \quad . \qquad (3.11)$$

By equating (3.7) and (3.11) and rearranging we obtain an integral equation specified by the electron temperature, empirical ionization cross section, neutral gas density, ion mobility, and discharge geometry:

$$2 \left(\frac{2}{\pi m_e} \right)^{1/2} \frac{e \cdot N \cdot \Lambda^2}{\mu_i} = \frac{(k_b T_e)^{5/2}}{\int_{\varepsilon_i}^{\infty} \varepsilon \cdot \sigma_i(\varepsilon) \cdot \exp(-\varepsilon / k_b T_e) \, d\varepsilon} \qquad (3.12)$$

Furthermore, if ion mobility is directly related to gas density, then $\mu_i \simeq \mu_o N_o / N$, where μ_o and N_o are ion mobility and neutral gas density respectively, at standard temperature and pressure. By expressing N in terms of measurable pressure, the left hand side of (3.12) can be written as a product of pressure and diffusion length:

$$(CP\Lambda)^2 = 2 \left(\frac{2}{\pi m_e} \right)^{1/2} \frac{(3.54 \times 10^{18})^2}{\mu_o N_o} \cdot P^2 \cdot \Lambda^2 \qquad (3.13)$$

Here P is in Torr, and Λ is in centimeters. C has units of

$eV^{1/4}/(cm \cdot Torr)$ and is equal to 414 $eV^{1/4}/(Torr \cdot cm^2)$ for argon. Equation (3.12) is now

$$(CP\Lambda)^2 = \frac{(k_b T_e)^{5/2}}{\displaystyle\int_{\varepsilon_i}^{\infty} \varepsilon \cdot \sigma_i(\varepsilon) \cdot \exp(-\varepsilon/k_b T_e)\, d\varepsilon} . \tag{3.14}$$

The above equation is a universal curve that directly relates discharge pressure and geometry with an electron temperature necessary to sustain the discharge in a state of Schottky diffusion. Using the empirical data of total ionization cross section for argon from Reference (51), (see Figure 3.1), Equation (3.14) can be numerically evaluated. Figure 3.2 shows the result of this calculation as a solid line. This figure also shows probe data for a variety of discharge heights with and without the four-pole samarium cobalt magnet configuration. The experimental data follows the Schottky diffusion theory at pressure diffusion products, $P\Lambda$, above .015 Torr·cm, but below this value, one does not see the dramatic increase in electron temperature predicted by the theory.

As the discharge is pushed to smaller volumes and or pressures, Schottky diffusion is no longer valid. At lower pressures and within smaller geometries, the mean free path of ions exceeds the dimensions of the bounding geometry. The charged-particle distribution becomes uniform and is no longer governed by volume collisions as assumed in Schottky diffusion theory. A new diffusion theory is necessary to describe the extreme case of a uniform, collisionless discharge.

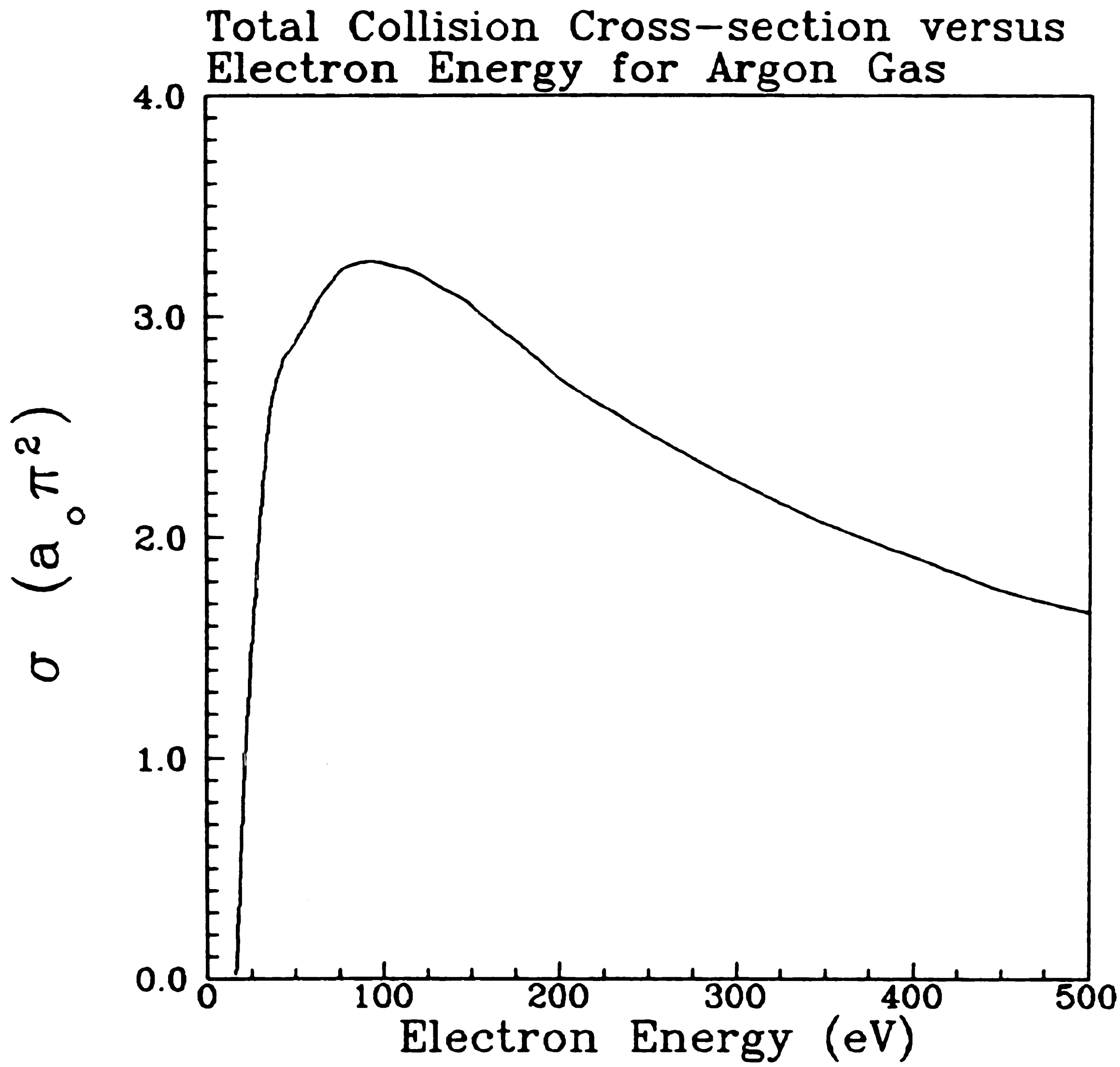

Figure 3.1 Total Collision Cross-Section versus Electron Energy for Argon

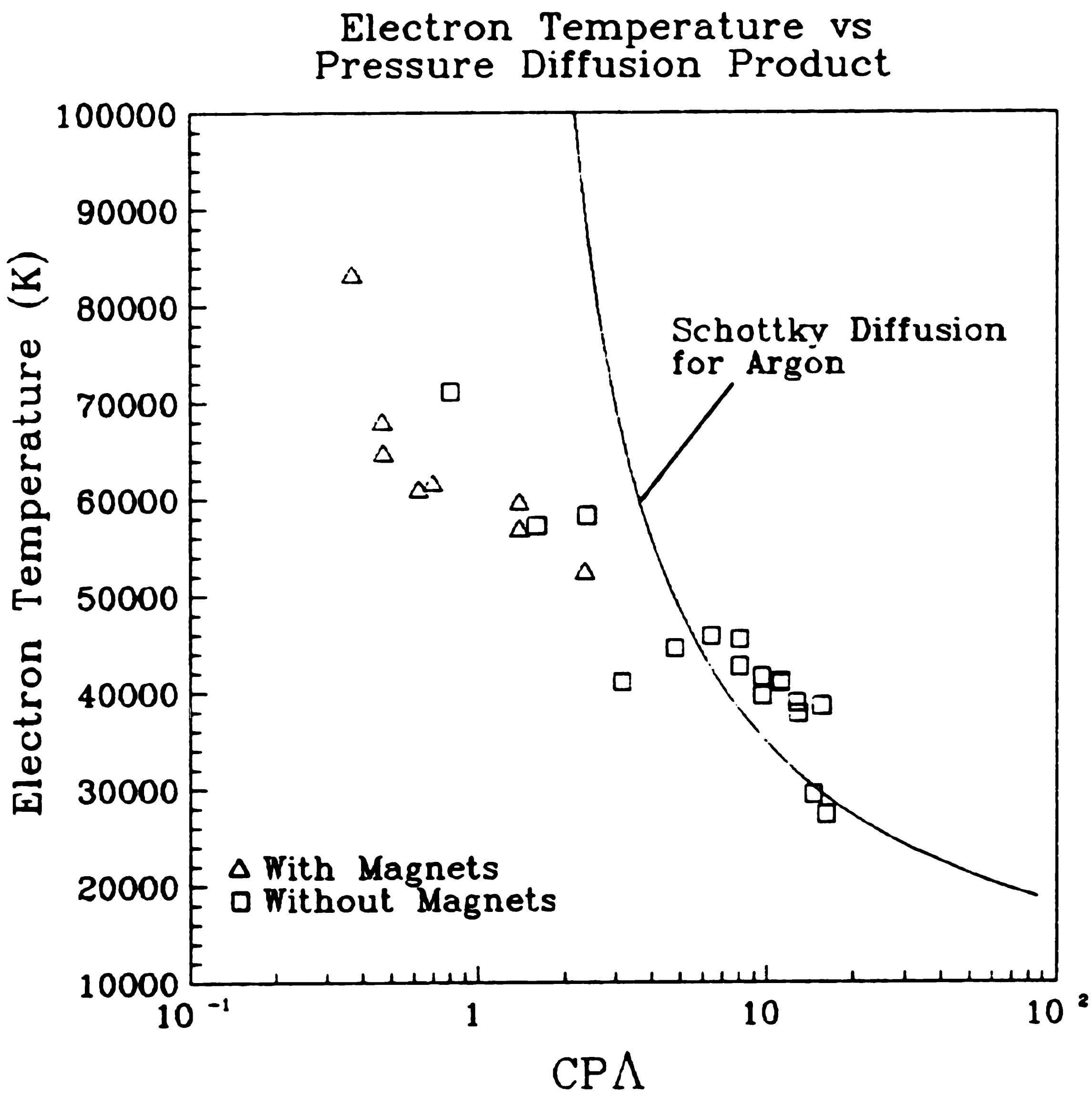

Figure 3.2 Universal Schottky Diffusion Curve for Argon

3.2.4 FREE-FALL DIFFUSION

The collisionless discharge is a classic problem and model dating back to Irving Langmuir's work[52] and initial assumptions of low-pressure, uniform discharges. The main assumptions are that the mean free path is greater than the discharge geometry and that only ionization collision terms dominate the in the transport equations. After generation the ions freely fall to the discharge walls. With the exception of the plasma sheath regions near the walls, quasi-neutrality is assumed where electron and ion densities are approximately equal, $n_e(r,z) \cong n_i(r,z)$, throughout the interior of the discharge. This is know as "free-fall" diffusion[48] and can be treated as the limiting case as the discharge density profile becomes uniform.

In the following use of free-fall diffusion, we assume that the electron and ion densities are fairly constant throughout the discharge, and significant density variations occur only near the plasma sheath. Ionization is constant throughout the discharge.

With the preceding assumptions, it is possible to derive a universal diffusion curve for this special case of free-fall diffusion, but to do so we must concentrate on the ion flux of the discharge at the sheath boundary. There are very few volume recombinations at low pressure, therefore we may assume that every ion generated in the volume of the discharge eventually recombines with an electron at the discharge boundary. Thus the number of ions impinging upon the discharge walls is equal to the number of ions generated within the volume. Assuming uniform ion flux and charged-particle density, this particle balance may be expressed as follows:

$$\Gamma_i \cdot A_{wall} = n_i \, \nu_i \, V_{discharge} \tag{3.15}$$

$$\Gamma_i \cdot 2\pi(rl + r^2) = n_{io}\nu_i \cdot \pi r^2 l \tag{3.16}$$

where Γ_i is the ion flux density, A_{wall} is the wall area, $V_{discharge}$ is the discharge volume, and n_{io} is the ion density throughout the discharge. From the Bohm sheath criterion[36-38] the ion flux to the walls is estimated as

$$\Gamma_i = 0.61 \cdot n_{eo}(k_b T_e / M_i)^{1/2} \tag{3.17}$$

with quasi-neutrality, $n_{eo} = n_{io}$, within the uniform discharge. We may now solve for ν_i.

$$\nu_i = \frac{2\,[\;0.61 \cdot (k_b T_e / M_i)^{1/2}\;]}{(\;rl / r + l\,)} \tag{3.18}$$

Equating (3.18) with (3.11) and letting $\alpha = (\;rl / r + l)$,

$$N\cdot(2\,M_i/\,\pi\,m_e)^{1/2}\cdot\alpha\,/\,0.61 = \frac{(k_bT_e)^2}{\displaystyle\int_{\varepsilon_i}^{\infty} \varepsilon\cdot\sigma_i(\varepsilon)\cdot\exp(-\varepsilon/k_bT_e)\;d\varepsilon}\,. \tag{3.19}$$

Finally, with appropriate conversion of neutral density to pressure in Torr and free-fall diffusion length, α, to centimeters, we have a universal diffusion expression for free-fall diffusion.

$$CP\alpha = \left(\frac{2M_i}{\pi m_e}\right)^{1/2}\cdot(3.54 \times 10^{18}/\,0.61)\cdot P\cdot\alpha$$

$$= \frac{(k_bT_e)^2}{\displaystyle\int_{\varepsilon_i}^{\infty} \varepsilon\cdot\sigma_i(\varepsilon)\cdot\exp(-\varepsilon/k_bT_e)\;d\varepsilon} \tag{3.20}$$

C is in $1/(cm^3 Torr)$ and is equal to $1098/(cm^3 Torr)$ for argon. As in the Schottky model, the right hand equation may be numerically evaluated to produce a $CP\alpha$ versus T_e curve. This has been done in Figure 3.3 for argon.

Consider an argon discharge of fixed radius and length. The pressure may be varied to traverse the operating point on either the $CP\Lambda$ or $CP\alpha$ curve. There is a one-to-one correspondence between the two curves, and they may be superimposed as shown in Figure 3.4. At

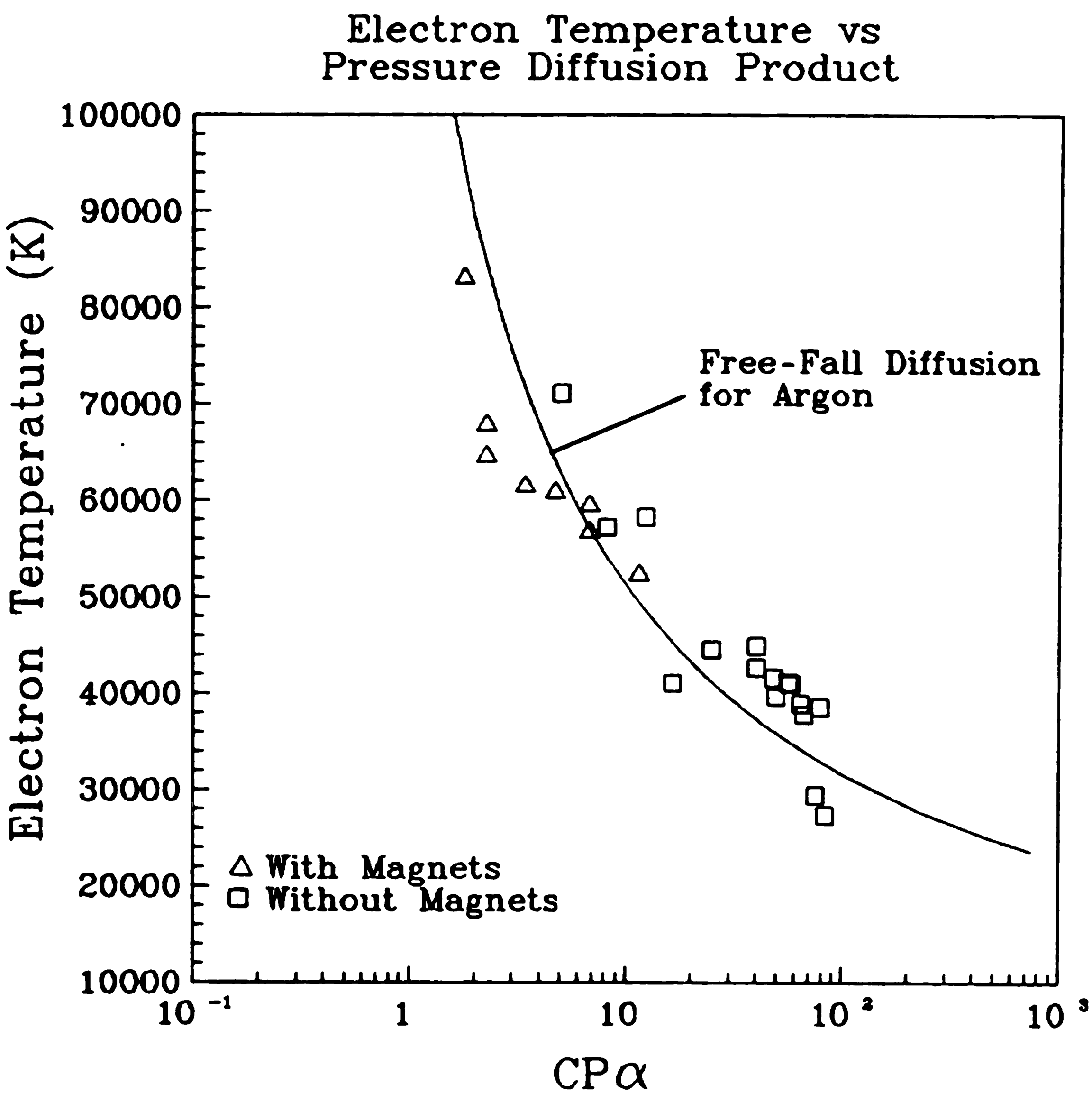

Figure 3.3 Universal Free-Fall Diffusion Curve for Argon

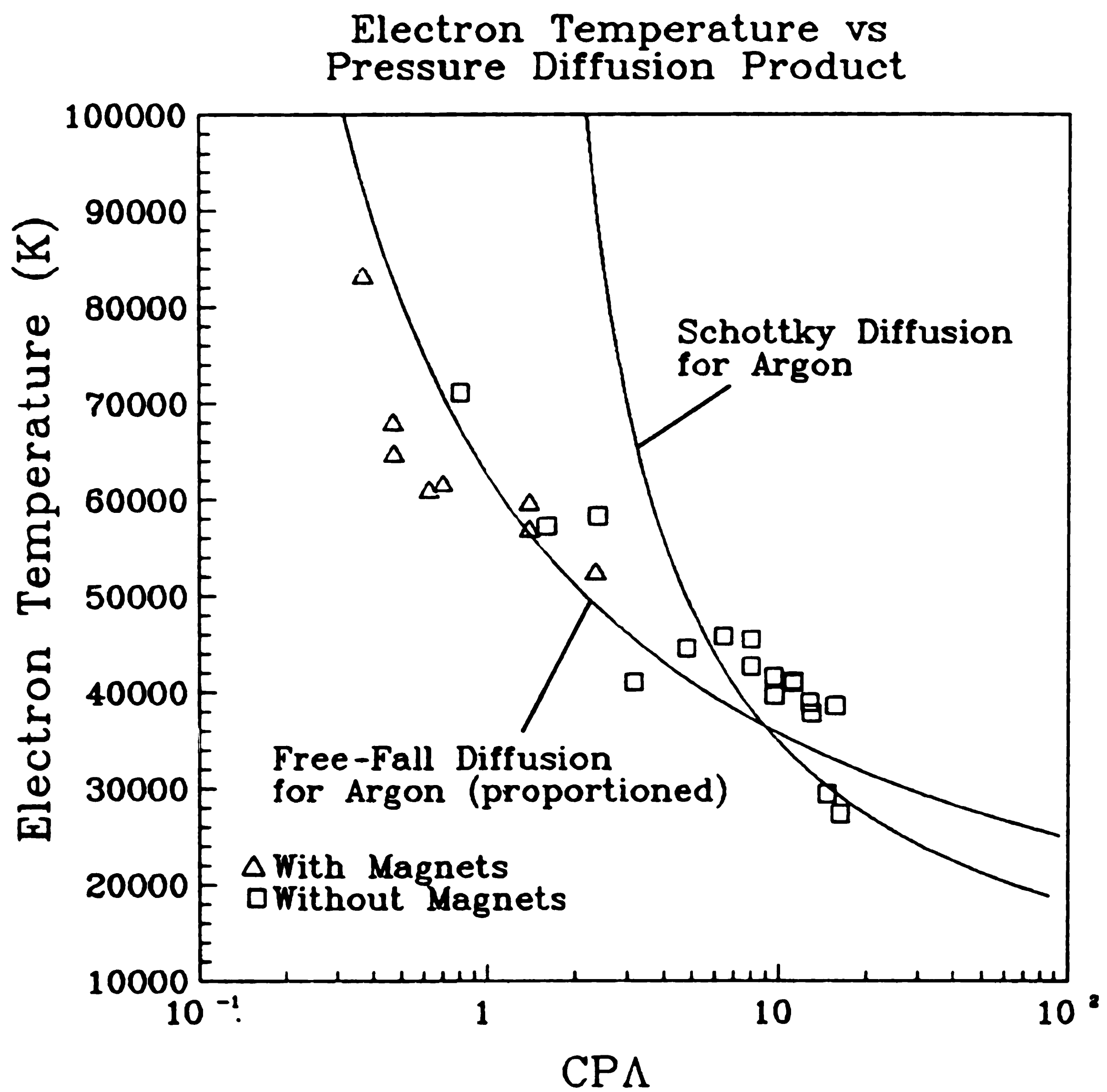

Figure 3.4 Superposition of Schottky and Free-Fall Diffusion Curves

$T_e \simeq 36{,}000$ K and $P\Lambda \simeq .015$ Torr·cm, the argon discharge makes a transition from Schottky to free-fall diffusion.

In Figure 3.4 experimental measurements with and without a magnetic field made in the first ion source prototype follow the theoretical curves and their transition. The comparison suggests that the addition of a multicusp magnetic field does not substantially change the total charged-particle diffusion and that Schottky and free-fall diffusion models can be used to approximate the diffusion processes. Equations (3.20) and (3.14) may be used as general guides for understanding the ion source discharge as pressure and geometry are changed. That is, even with the inclusion of a multicusp ECR magnetic field covering only a fraction of the discharge volume, these simple diffusion models may be used as scaling laws for the design of larger or smaller multicusp ECR ion or plasma sources.

3.3 IONIZATION POWER AND DIFFUSION MODELING

3.3.1. INTRODUCTION

One objective of this research was to build an efficient ion source that achieves high densities with less than 200 Watts of input power. Of particular interest is the power put into ionization. As discussed in Section 2.4.2, ionization power for a 5 cm diameter discharge at less than 10 mTorr is estimated to be 20% to 30% of the total microwave power coupled into the cavity. By calculating the theoretical ionization power for a particular plasma volume and charged-particle density, we may estimate the required total power necessary to operate the plasma source or choose geometries to accommodate density and power requirements.

In this section the CPΛ and CPα curves will be used in conjunction with power recombination expressions for Schottky and free-fall diffusion in a closed cylindrical geometry. Power curves will be presented for variations in pressure and discharge geometry. The curves will be used to show that the desired ion source discharge density and operating power are reasonable for given discharge pressure, height and diameter.

3.3.2 POWER ABSORPTION

Whether by DC or rf excitation, power is coupled into the discharge through the Joule heating of the electron sub-gas. See Figure 3.5. Energy coupled into the electron sub-gas is then dispersed throughout the discharge by diffusion, conduction, and elastic and inelastic collisions with neutrals and ions. The circle around the electron gas in Figure 3.5 isolates the electron gas as a closed system. Thus, a power and energy balance can be written solely in terms of electron energy transport.

In any differential volume of plasma at position $\vec{r}$, power is both absorbed and lost by electrons. In the steady state condition,

$$\langle P\rangle_{abs}(\vec{r}) = \langle P\rangle_{loss}(\vec{r}) \quad . \tag{3.21}$$

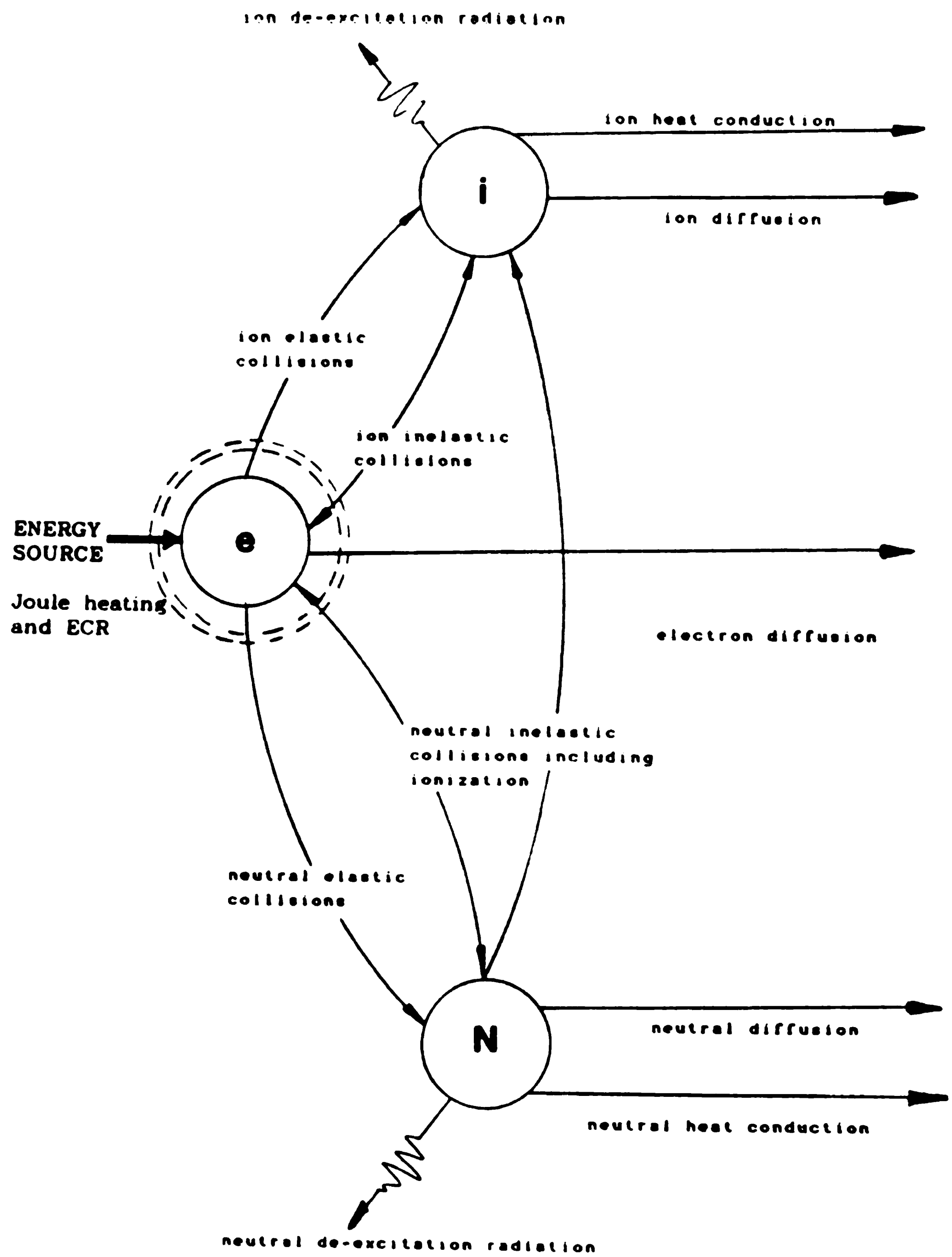

Figure 3.5 Energy Transport Paths in a Discharge

The power is absorbed by direct Joule heating of the electron gas through the electric fields. For microwave excitation the power absorption term is expressed as[50]

$$\langle P\rangle_{abs}(\vec{r}) = \frac{n_e(\vec{r})\, e^2}{2\, m_e \nu_e} \left(\frac{\nu_e^2}{\omega^2 + \nu_e^2}\right) |E(\vec{r})|^2 . \qquad (3.22)$$

n_e is the time independent electron density, ν_e is the effective electron collision frequency, ω is the microwave frequency and $|E(\vec{r})|$ is the magnitude of the exciting electric field. The collision frequency drops with neutral gas density,[25] and thus good microwave coupling depends on pressure and the microwave frequency. At low pressures ($\leq$ 100 mTorr) the effective collision frequency becomes much less than the microwave frequency and (3.22) becomes

$$\langle P\rangle_{abs}(\vec{r}) = \frac{n_e(\vec{r})\, e^2}{2\, m_e \nu_e} \left(\frac{\nu_e}{\omega}\right)^2 |E(\vec{r})|^2 . \qquad (3.23)$$

Thus at low pressure, high electric fields are required to sustain a discharge at high density. Efficient power coupling is possible at low pressures because of the high fields available within resonant microwave cavities. High electric fields with efficient power coupling give the resonant cavity structure an advantage over many other microwave approaches used to maintain low-pressure discharges.[53-56]

Static magnetic fields improve the power coupling in microwave plasmas through ECR heating of the electron sub-gas. Consider the power absorption term for an rf discharge placed in a uniform magnetic field perpendicular to the exciting electric field, $\vec{E} \perp \vec{B}_o$.[25]

$$\langle P\rangle_{abs}(\vec{r}) = \frac{n_e(\vec{r})e^2\nu_e}{2m_e}\left(\frac{1}{\nu_e^2 + (\omega - \omega_{ce})^2} + \frac{1}{\nu_e^2 + (\omega + \omega_{ce})^2}\right)|E(\vec{r})|^2 \tag{3.24}$$

As the pressure of the discharge decreases, the effective collision frequency, ν_e, decreases giving rise to a pole at those physical positions where $\omega = \omega_{ce}$. Here ω_{ce} is the electron cyclotron frequency and is given as

$$\omega_{ce} = \frac{eB}{m_e} \tag{3.25}$$

where B is the magnitude of the magnetic field, e is the electron charge and m_e is the electron mass. For f = 2.45 GHz, B = 875 Gauss. Even with moderate electric fields, good power coupling can be achieved through ECR heating in low-pressure discharges.

3.3.3 POWER LOSS

Returning to Figure 3.5, the steady-state power loss expression for a differential volume is

$$\langle P\rangle_{loss}(\vec{r}) = \left[\left(\frac{5kT_e}{2}\right) \frac{D_a}{\Lambda^2} + \nu_{men}\left(\frac{2m_e}{M_n}\right) \frac{3k}{2} \left(T_e - T_n\right) \right.$$

$$\left. + eV_i \cdot \nu_i + \sum_j eV_{exj} \cdot \nu_{exj} \right] \cdot n_e(\vec{r}) \ . \qquad (3.26)$$

Term by term, Equation (3.26) includes power losses due to diffusion (Schottky diffusion in this case), heating of the neutral gas through electron-neutral elastic collisions, ionization, and excitation. As we have assumed T_e to be uniform, heat conduction losses have been neglected.

The collision frequencies are dependent upon empirical collision cross sections, $\sigma_x(\varepsilon)$, and the electron energy distribution. The ionization frequency was given earlier in Equation (3.11). The momentum transfer and excitation frequencies are defined as

$$\nu_{men} = N\frac{2\sqrt{2}}{\sqrt{m_e \pi}}\left(\frac{1}{kT_e}\right)^{3/2} \int_o^{\infty} \sigma_{men}(\varepsilon)\cdot\varepsilon\cdot\exp(-\varepsilon/\ kT_e)\ d\varepsilon \qquad (3.27)$$

$$\nu_{exj} = N\frac{2\sqrt{2}}{\sqrt{m_e \pi}}\left(\frac{1}{kT_e}\right)^{3/2} \int_{\varepsilon_{exj}}^{\infty} \sigma_{exj}(\varepsilon)\cdot\varepsilon\cdot\exp(-\varepsilon/\ kT_e)\ d\varepsilon \qquad (3.28)$$

The power required to maintain a differential volume of plasma can then be calculated if the following information is known: electron temperature, electron density, neutral gas pressure and temperature, collision cross sections for all elastic and inelastic collision processes, and the characteristic diffusion length or discharge geometry. Finally, Equation (3.26) can be integrated over the volume of the discharge to find the total required power.

Empirical collision cross sections for argon are known, and it is possible to find exact power requirements for an argon discharge. However, for our present purposes we seek only an estimation of the total power. In Section 2.4.2, it was determined that ionization power was between 20% and 30% of the total input power with a four pole magnetic field. If we assume that the proportion of ionization power does not exceed 30% at pressures below 10 mTorr, we may use ionization power as method for estimating the total power required to operate the ion source at a density of $10^{12}/\text{cm}^3$.

There are two methods of calculating the ionization power. It was assumed for both Schottky and free-fall diffusion that the number of recombination events within the discharge volume is negligible. All power placed into ionization must then be lost in the recombination of electrons and ions at the discharge wall. Ionization power therefore may be calculated by integrating (3.26) over the volume of the discharge,

$$\int_V P_i(r)\, dv = \int_V eV_i \nu_i \, dv \qquad (3.29)$$

or by multiplying the current flux to the discharge walls by the ionization potential. From the continuity relation and charge neutrality we have

$$\nabla \cdot \vec{\Gamma} = \nu_i n_e(\vec{r}) \tag{3.30}$$

$$\vec{\Gamma}_e(\vec{r}) = \vec{\Gamma}_i(\vec{r}) = \vec{\Gamma}(\vec{r}) \tag{3.31}$$

whereby

$$\int_V eV_i \nu_i n_e(\vec{r}) dv = \int_V eV_i \nabla \cdot \vec{\Gamma}(\vec{r})\, dv = \int_S eV_i \vec{n} \cdot \vec{\Gamma}(\vec{r})\, ds \tag{3.32}$$

With the assistance of the CPΛ and CPα curves and the solution to the diffusion equation, $n_e(\vec{r})$, we may easily find the ionization power for a wide range of conditions. For this calculation it is best to evaluate the current flux to the walls and avoid recalculating ν_i for every new value of electron temperature encountered in the analysis. The current flux to the walls in a disk-shaped discharge has been given by Dahimene[9] for the case of Schottky diffusion:

$$P_{total} = V_i \mu_i k T_e\, n_o \left(2\, \frac{r^2}{l}\,(4.248) + l\,(5.002)\right) \quad . \tag{3.33}$$

n_o is the peak electron density at the center of the discharge.

Current flux in the case of free-fall diffusion is evaluated at the plasma sheath edge with the use of the Bohm sheath criterion. The

current flux is

$$\vec{\Gamma} = (0.61)\ n_o \left(\frac{kT_e}{M_e} \right)^{1/2} \vec{r}\ . \tag{3.34}$$

The total recombination power for free-fall diffusion becomes

$$P_{total} = eV_i\ 2\pi\ (rl + r^2)\ (0.61)\ n_o \left(\frac{kT_e}{M_e} \right)^{1/2} . \tag{3.35}$$

Equations (3.33) and (3.35) can be written in terms of average power density, which yields the power-per-unit-volume required to sustain the plasma.

Schottky Diffusion Power Density

$$\frac{P_A}{V_{discharge}} = V_i \mu_i kT_e\ N_o \left(\frac{2}{\pi l^2}\ (4.248) + \frac{1}{\pi r^2}\ (5.002) \right) \tag{3.36}$$

Free-Fall Diffusion Power Density

$$\frac{P_A}{V_{discharge}} = eV_i \frac{2}{\alpha}\ (0.61)\ N_o \left(\frac{kT_e}{M_e} \right)^{1/2} \tag{3.37}$$

The power density equations can be examined with the aid of the CPΛ and CPα curves as was done with the total ionization power.

Equations (3.14), (3.20), (3.33), and (3.35) have been examined over a wide range of parameters. In the compact design, the extraction area fixes the discharge diameter to 5 centimeters in diameter. The hypothetical electron density is 10^{12}. Also it is assumed that argon is the working gas and that the neutral gas temperature is 350 K. In Figures 3.6 and 3.7 ionization power has been plotted against discharge pressure for a number of fixed discharge heights. Figures 3.8 and 3.9 show power density versus pressure. In both diffusion models the required ionization power density decreases as height increases. This is generally true for any increase in Λ or α.

In Figure 3.10 the discharge geometry has been fixed and curves of power versus pressure for Schottky and free-fall diffusion have been superimposed. This figure can be compared to Figure 3.11 where electron temperature versus pressure have been plotted for the same points of analysis. In Figure 3.11 the transition between Schottky and free-fall diffusion occurs at about 36,000 K and 10 mTorr. Beam extraction is conducted at discharge pressures below 10 mTorr and thus a 2.5 cm radius discharge is best modeled by free-fall diffusion.

3.3.4 POWER REQUIRED IN A COMPACT ION SOURCE DISCHARGE

It was hoped that a simple 5 cm diameter ion source may achieve high densities with less than 200 W of total input power. However, as shown in Figure 3.7, over 75 Watts of ionization power are required to achieve a charged-particle density of $10^{12}/cm^3$ at 5 mTorr. This translates to an estimated 250 Watts of total input power. This is

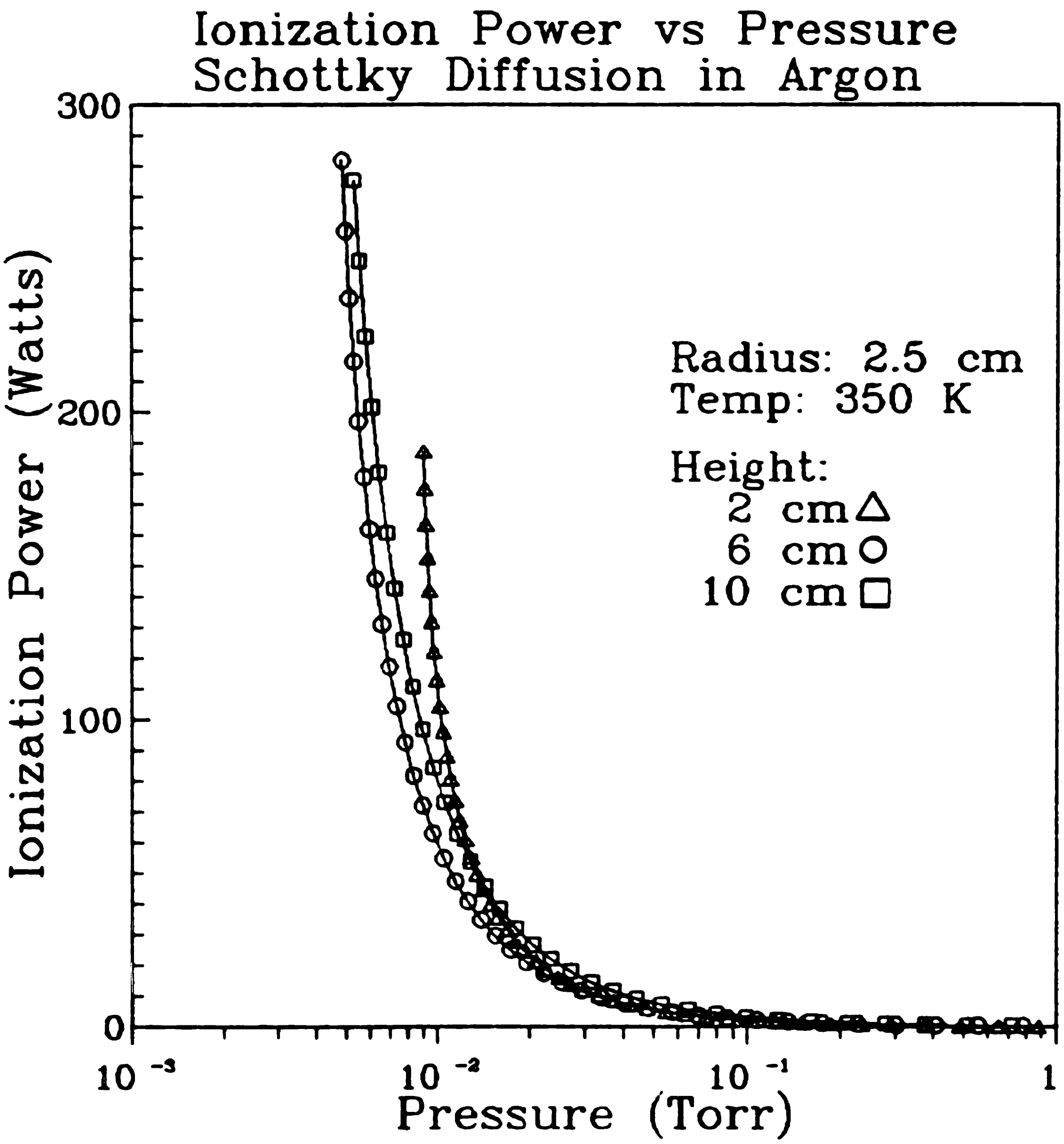

Figure 3.6 Ionization Power versus Pressure for Schottky Diffusion

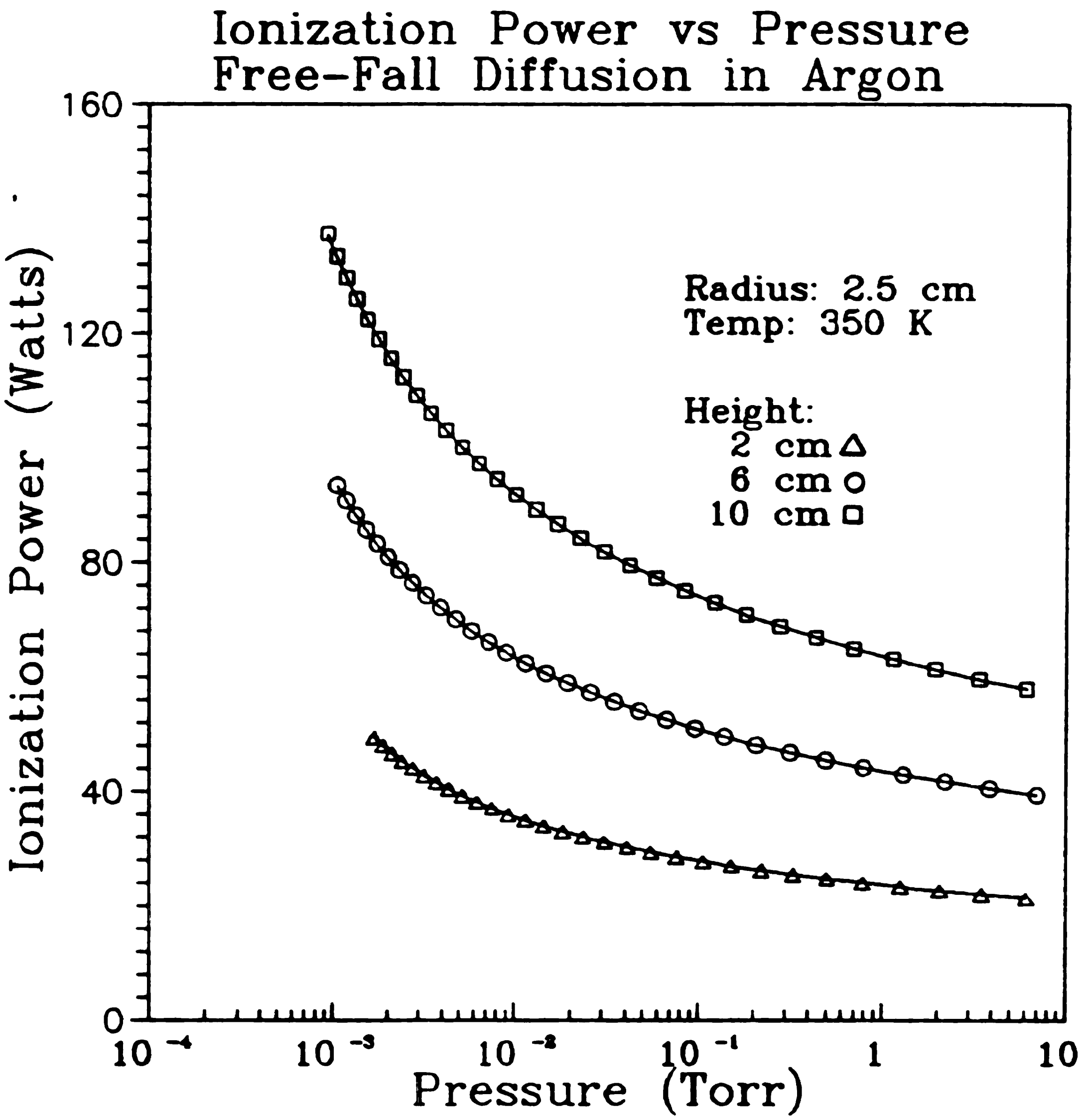

Figure 3.7 Ionization Power versus Pressure for Free-Fall Diffusion

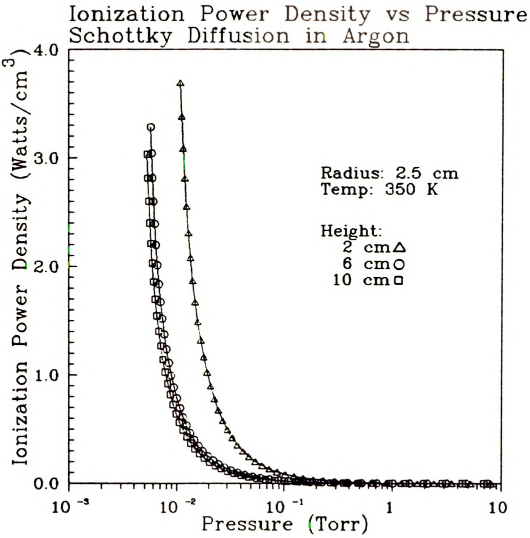

Figure 3.8 Ionization Power Density versus Pressure for Schottky Diffusion

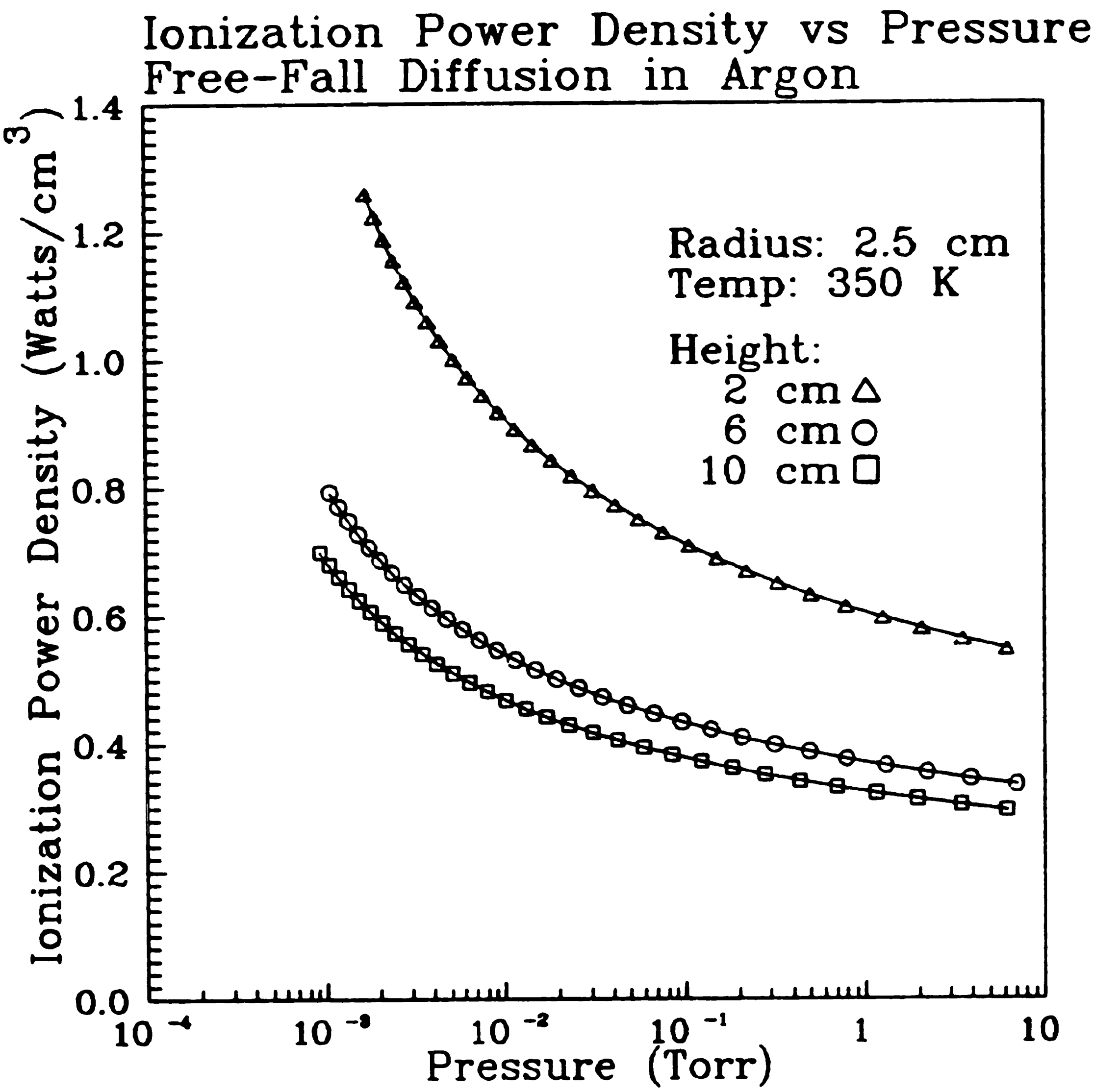

Figure 3.9 Ionization Power Density versus Pressure for Free-Fall Diffusion

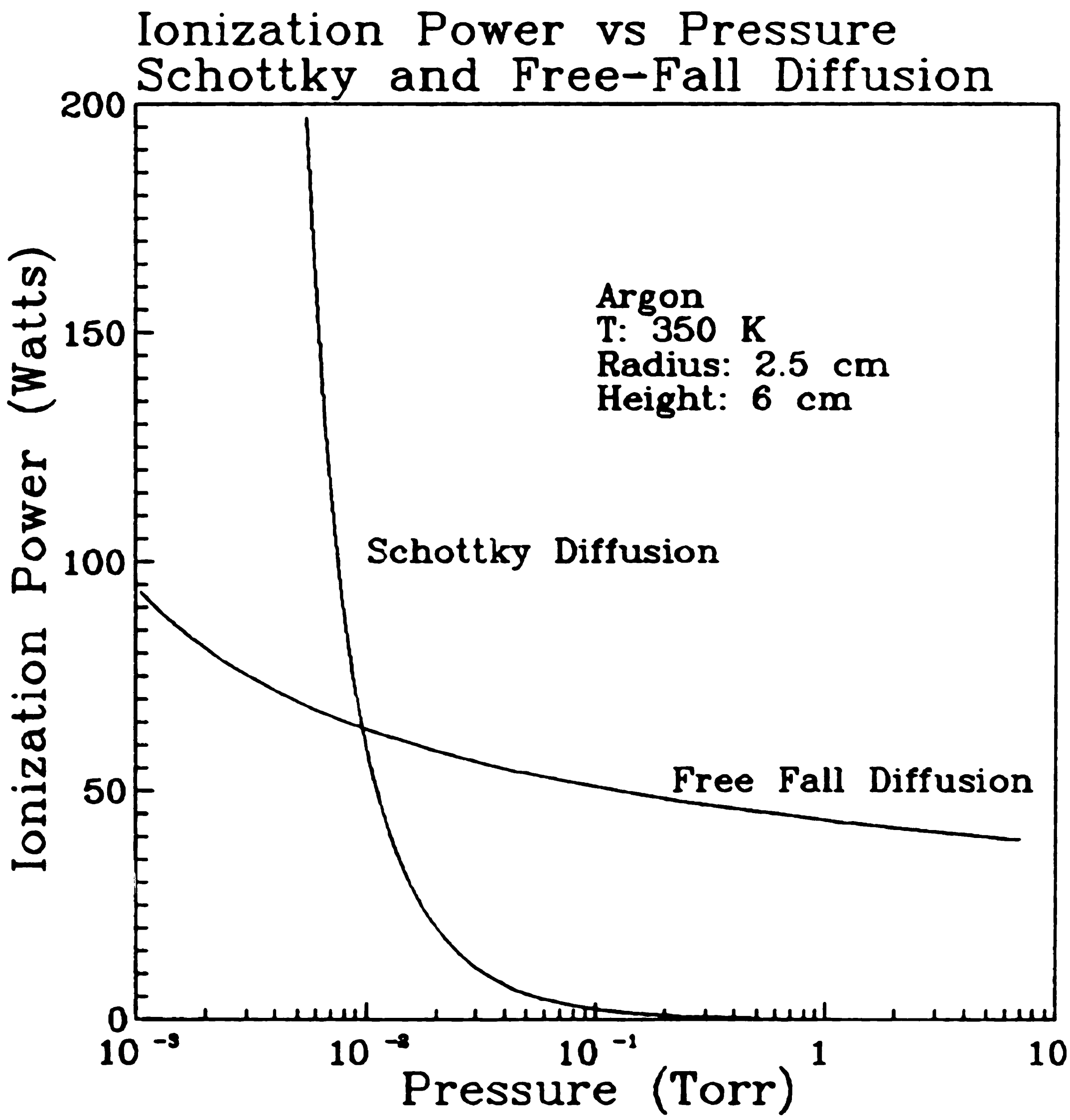

Figure 3.10 Ionization Power versus Pressure
for a 2.5 cm Diameter by 6 cm High Discharge

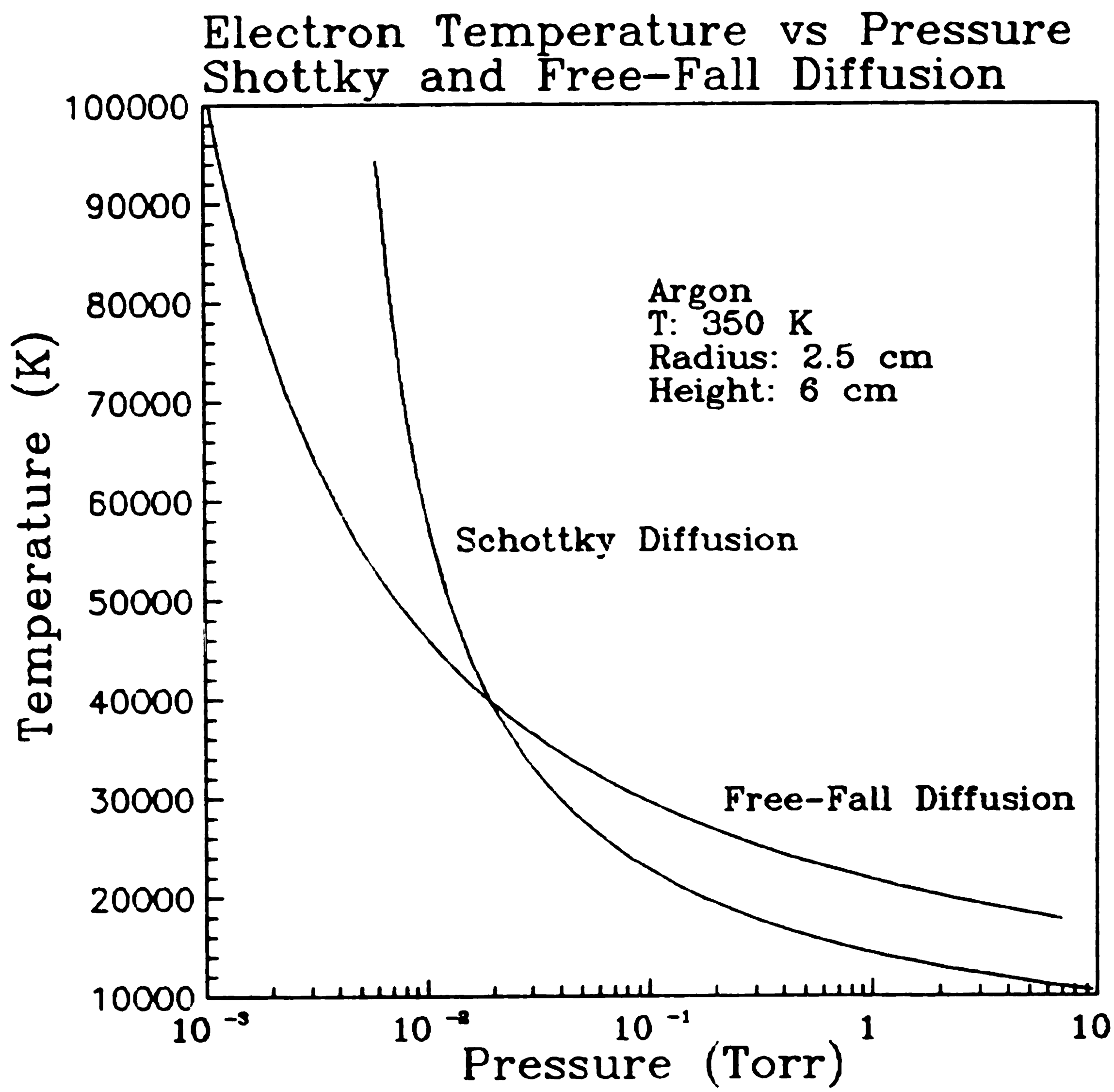

Figure 3.11 Electron Temperature versus Pressure for a 2.5 cm Diameter by 6 cm High Discharge

reasonable considering that in the data of Figure 2.18 of Chapter 2 140 Watts were required to maintain a discharge density of $5x10^{11}/cm^3$. A more accurate calculation of total power would require a complete evaluation of all power loss terms in Equation (3.26), including elastic collisions, excitation, radiation, and diffusion. Wall effects, such as sheaths, secondary electron emission, and wall currents, are not included in the differential volume expression, (3.26). These effects can greatly influence power loss and should be considered in the exact evaluation of power loss.

The above result demonstrates that, although oversimplified, the diffusion and power models are valid qualitative tools and can be used to predict the performance of a disk-shaped discharge. Furthermore the models may be used in optimizing the dimensions of a discharge. Figures 3.12 and 3.13 show ionization power versus discharge length for a number of fixed radii. Both Shottky and free-fall theories predict an optimal discharge length in terms of ionization power. This explains the observation made in Section 2.4.2, Figure 2.17 in which a 2.5 cm high discharge had a density lower than a 5 cm high discharge for equal input power.

Equations (3.36) and (3.37) can be used to investigate scaling properties of the discharge. Figure 3.14 shows ionization power density versus discharge length for free-fall diffusion. A large radius discharge operates with a lower power density than small radius discharges. This suggests that in general large discharges are more efficient than small discharges; efficiency improves as the discharge is enlarged.

It has been stated that the models presented in this chapter do not exactly describe the behavior of a discharge immersed in a multicusp magnetic field, but unfortunately the inclusion of a magnetic field presents seemingly unsurmountable difficulties to plasma modeling. The analysis of electromagnetic radiation and charged-particle motion in a gyrotropic, anisotropic medium is extremely complex. Thus the actual design of ECR microwave plasma and ion sources remains for the most part an empirical matter until more understanding about ECR microwave plasmas is gained and more sophisticated models are developed.

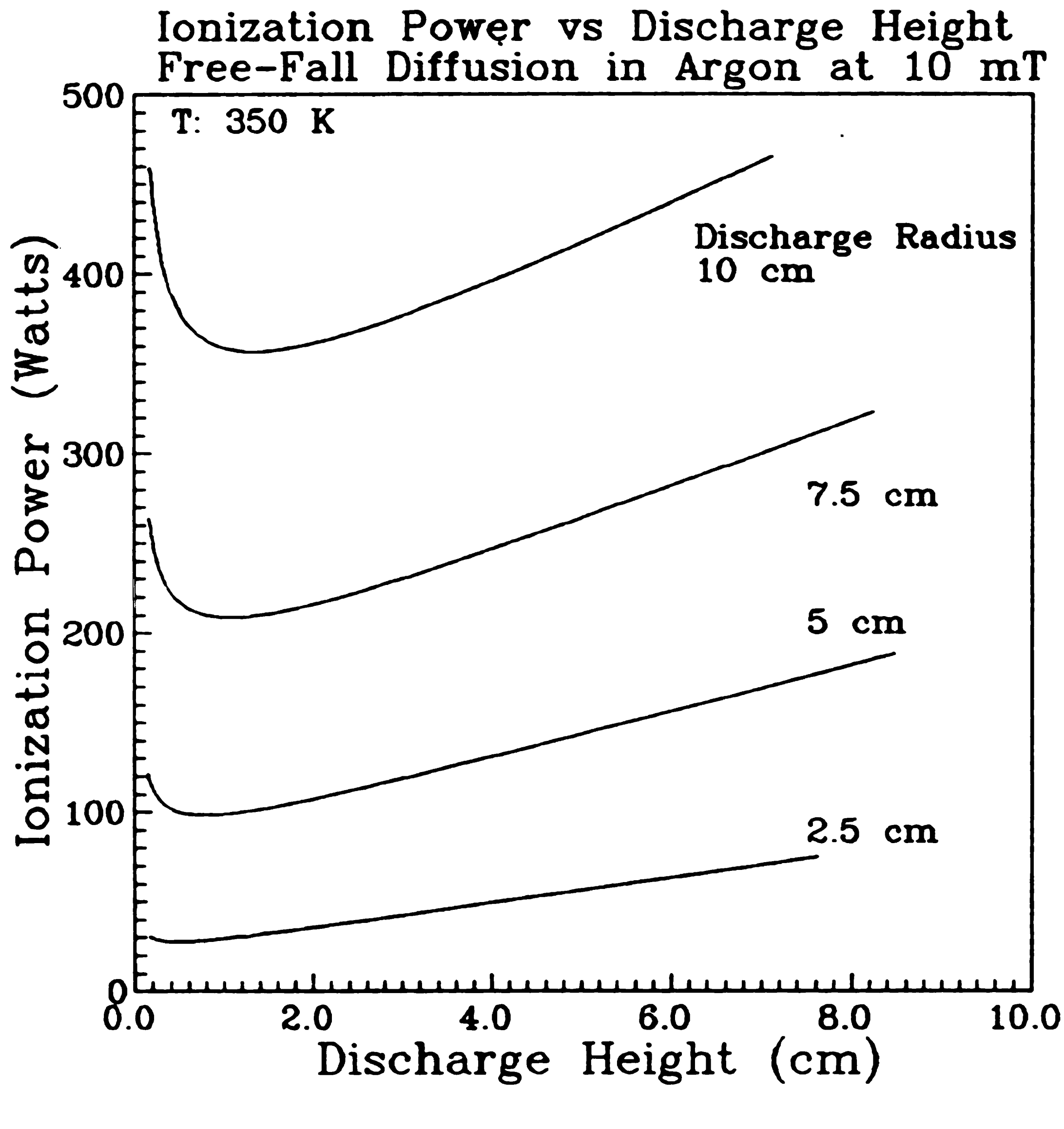

Figure 3.12 Ionization Power versus Discharge Height for Free-Fall Diffusion

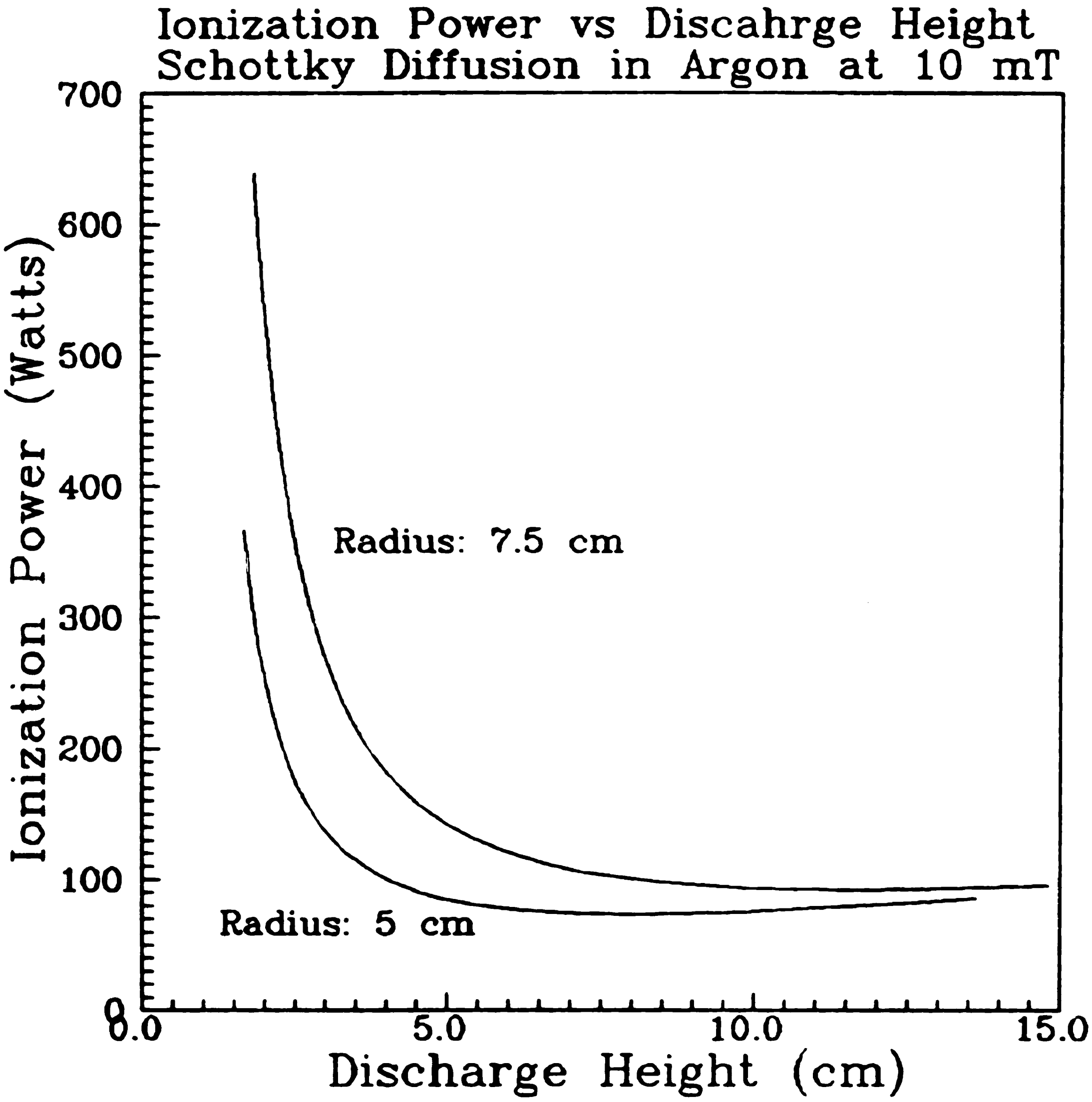

Figure 3.13 Ionization Power versus Discharge Height for Schottky Diffusion

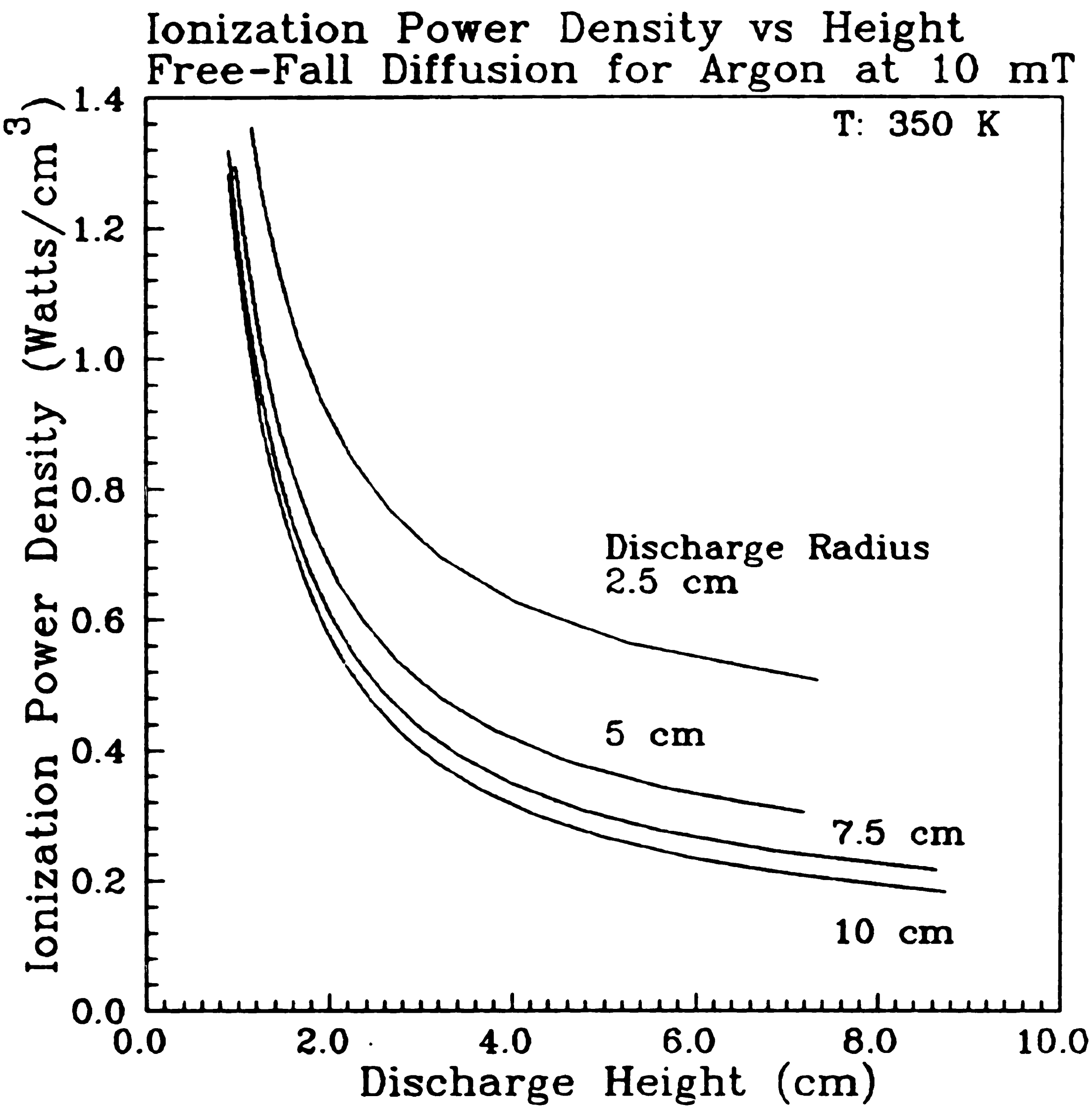

Figure 3.14 Ionization Power Density versus Discharge Height for Free-Fall Diffusion

CHAPTER 4

A REFINED COMPACT ECR MICROWAVE-CAVITY ION SOURCE: PROTOTYPE II

4.1 INTRODUCTION

The ion extraction experiments performed with the first experimental ion source prototype and presented in Chapter 2 were quite successful. High beam current densities in excess of 5 mA/cm^2 were extracted from a set of 3.2 cm diameter, 47% transparent, double-grid extraction optics. This was achieved with less than 200 Watts of input microwave power. However certain aspects of this preliminary design can be further improved to make the instrument more reliable, less expensive, and simpler to operate.

This chapter presents the design and performance of a second ion source prototype constructed upon the empirical knowledge and principles distilled from the studies of Chapter 2. The design of important aspects of the second ion source is reviewed in detail. Experimental charged-particle density measurements are used to predict the extractable beam current at low pressures. Also the results of beam extraction experiments are reported for double-grid optics, and the design of beam extraction optics as tailored to high-density discharges is discussed.

4.2 DESIGN OF A REFINED MICROWAVE-CAVITY ION SOURCE: PROTOTYPE II

4.2.1 COMPACT MICROWAVE-CAVITY ION SOURCE

This section reviews the final design of a refined compact microwave-cavity ion source. Two important changes have been made from the first prototype. The first is that the brass cavity diameter has been reduced from 17.8 cm to 8.9 cm. The second is that the permanent magnets have been imbedded in a non-magnetic stainless steel base plate as in other recent designs of ECR microwave-cavity plasma sources.[9,14,24] In the re-design of the ion source many other aspects of the instrument required attention such as water and air cooling, microwave radial chokes for DC isolation, and vacuum sealing. The final design is now presented with digressions upon specific design aspects of the instrument.

Figures 4.1 and 4.2 are mechanical drawings of the refined microwave ion source. It is similar to the earlier ion source with its brass shell (1), brass sliding short (2), non-magnetic stainless steel base plate (3), input antenna (4,5), and quartz capped discharge zone (11). Finger stock (6) provides good electric contact between moving assemblies. A screened viewing port (7) is cut into the side of the brass shell to observe the discharge. Six machine screws (8) hold the assembly together. Copper water cooling lines (9) are solder-packed into the base plate near the discharge region orifice.

Figure 4.3 shows a detailed cut-away of the discharge region. An O-ring channel and silicone O-ring (10) are used to vacuum seal the 4.9 cm i.d. x 2.8 cm high quartz cap (11) to the base plate. The

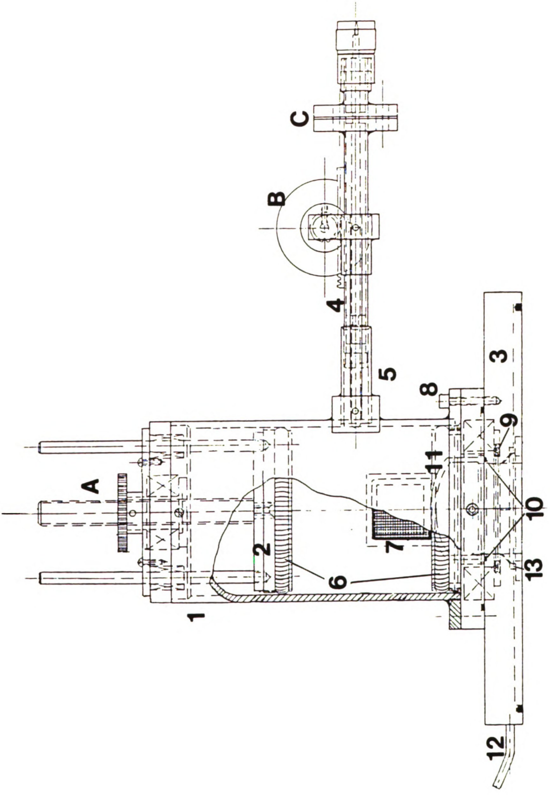

Figure 4.1 ECR Microwave-cavity Ion Source: Prototype II, Side View

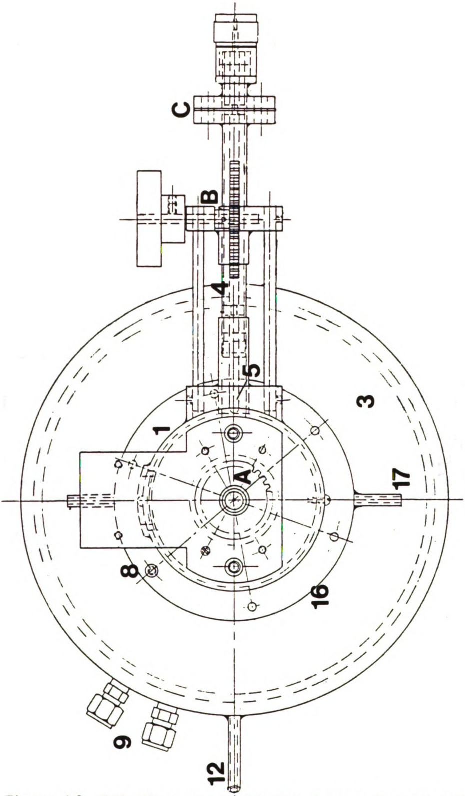

Figure 4.2 ECR Microwave-cavity Ion Source: Prototype II, Top View

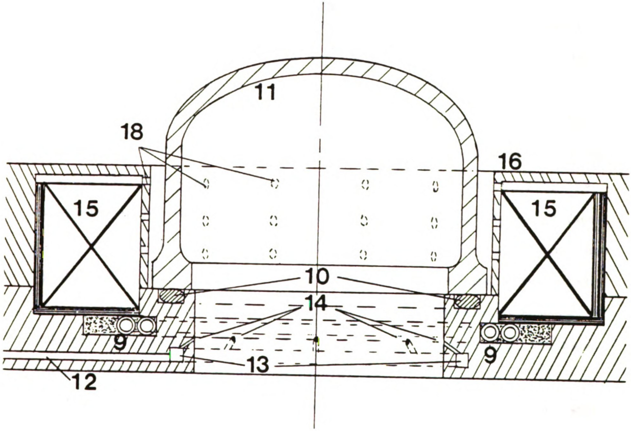

Figure 4.3 Prototype II, Detail of the Discharge Region

quartz cap (11) has a flattened edge to seat over the silicone O-ring and O-ring channel. (Note: This cap height is constant throughout the study of this second prototype ion source). As in the other prototype, gas is fed through the base plate (12) into an annular channel (13) and distributed into the discharge region by eight pin-holes (14). A total of sixteen neodymium-iron-boron magnets (15) are doubled and alternated in polarity on a soft iron magnet keeper to produce an eight-pole multicusp static magnetic field. The magnets have dimensions 1.3 cm x 1.3 cm x .5 cm and maximum field strength of .35 Tesla. The magnets are capped by a brass shield (16) which protects them from the heat of the discharge and which forms a flat conducting surface for the microwave-cavity shell. Compressed air for cooling (17) is introduced through the brass cap, circulates over the magnets, and is then directed by 30 pin holes (18) at the quartz face. The compressed air exhausts though the viewing window (7). The base plate orifice is 4.8 cm i.d. x 2.0 cm high making the discharge height 4.8 cm and the discharge volume about 90 cm^3. Screens, perforated plates, or extraction optics may be mounted to the bottom of the base plate by three screw holes (not shown).

In addition to making the ion source design compact, air and water cooling are strategically placed near the magnets and O-ring seal so the instrument can handle input powers greater than 200 Watts for extended periods of time. The short tuning mechanism (A) is simplified and the probe tuning mechanism (B) is reduced in size. The prototype can be easily disassembled for inspection and for re-configuration, i.e. magnet configuration, quartz cap height, input antenna orientation, etc.

Figures 4.4 through 4.8 are photographs of the components of the experimental instrument. Figure 4.9 shows the final assembly of the ion source.

4.2.2. MICROWAVE DESIGN ASPECTS

4.2.2.1 MICROWAVE CAVITY DIMENSIONS

Several parts of the ion source require careful microwave design. The first part is the single-mode microwave cavity. Equation 2.13 specifies the TE_{lmn} cavity mode heights as a function of microwave wavelength and cavity radius. Figure 4.10 shows cavity height versus cavity radius for the TE_{111} resonant cavity mode at 2.45 GHz. As the cavity radius becomes smaller, the lowest cavity resonant mode, TE_{111}, approaches the waveguide "cut-off". The cut-off radius establishes the smallest cavity radius that can be made and still excite the resonant mode. However, the cavity height goes to infinity as the radius approaches cut-off. In a compact single-mode design with a fixed microwave frequency, there is a compromise between cavity radius and height. In this design a brass cylinder was selected with a 3.5 inch inner diameter and a 3.75 inch outer diameter. This cylinder size can easily be adapted to common 8 inch vacuum flanges. The height for such a cavity is 10.5 cm. Additional height is included in the design to accommodate the cavity short tuning mechanism labeled (A) in Figures 4.1 and 4.2.

If a smaller cavity radius is desired, higher microwave frequencies must be used, although the use of higher frequencies presents other

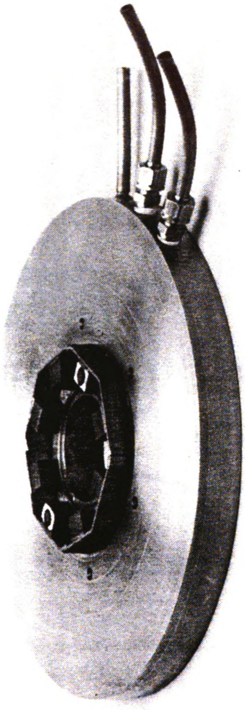

Figure 4.4 Stainless Steel Base Plate with Eight Magnets

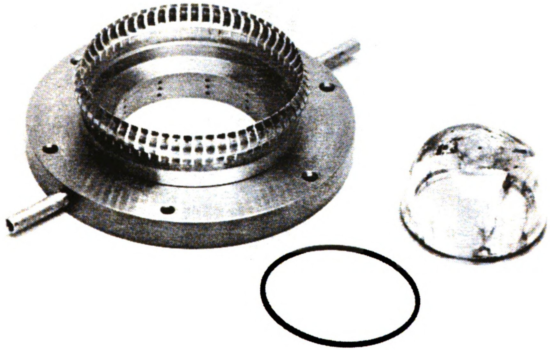

Figure 4.5 Brass Cap for Magnets, Silicone O-ring, and Quartz Cap

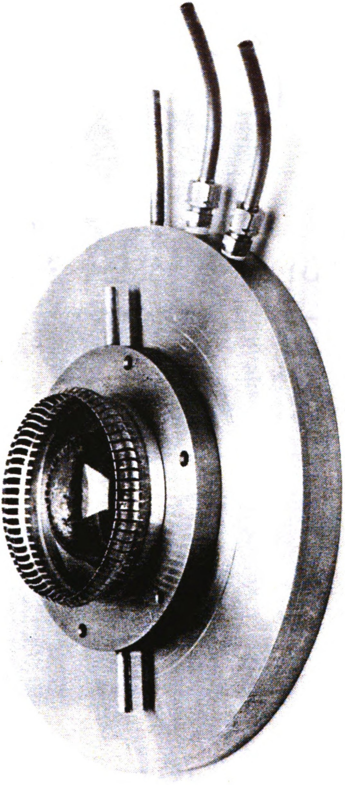

Figure 4.6 Base Plate Assembly

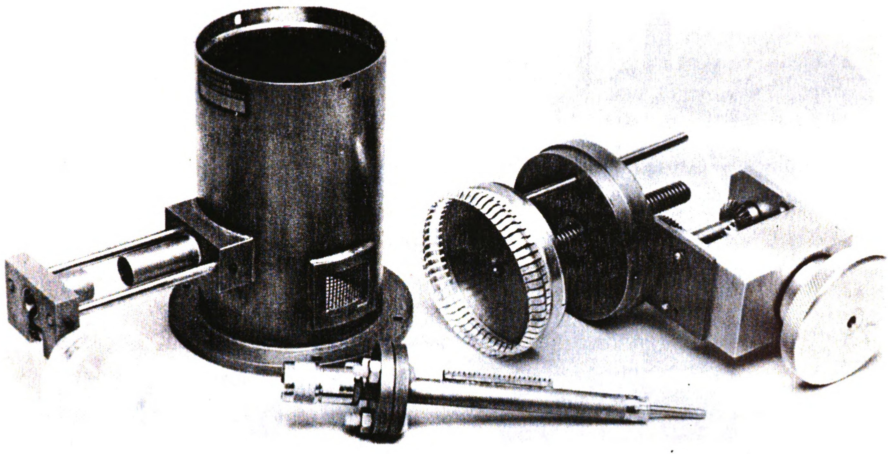

Figure 4.7 Brass Cavity, Input Probe/Antenna, and Sliding Short

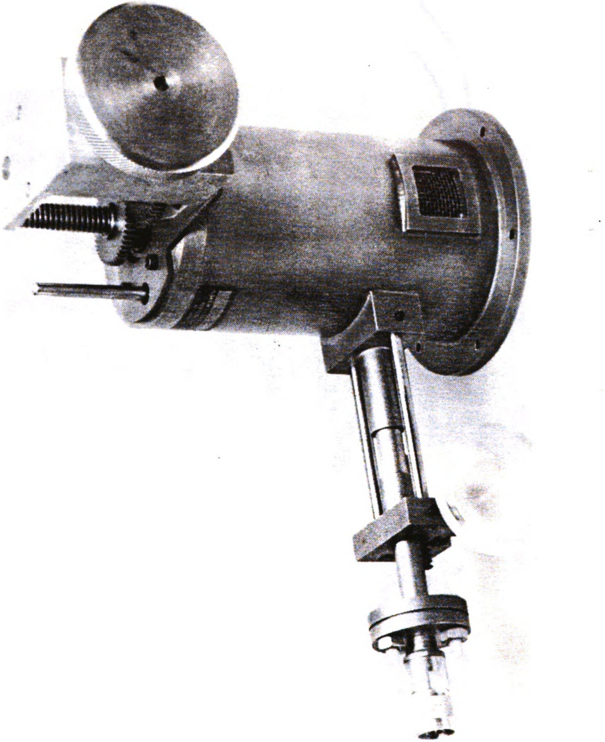

Figure 4.8 Microwave-cavity Assembly

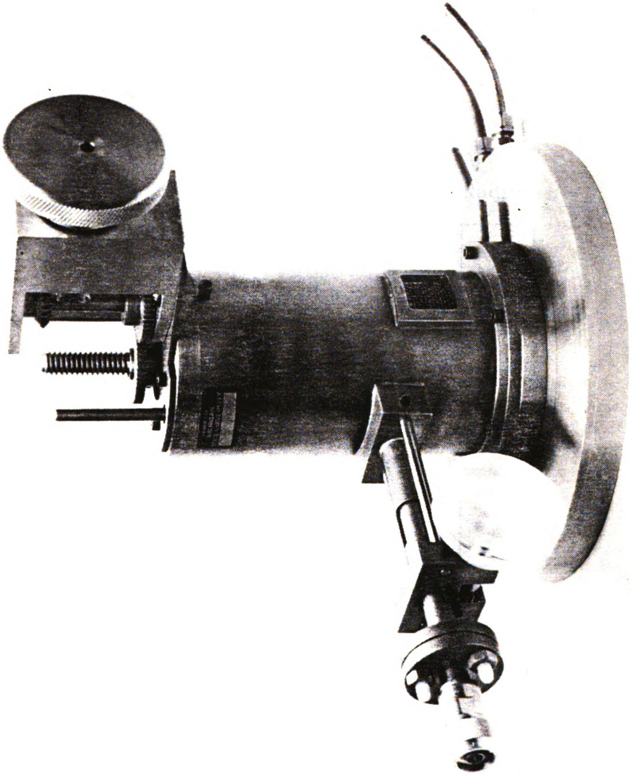

Figure 4.9 Assembly of the Microwave-cavity Ion Source: Prototype II

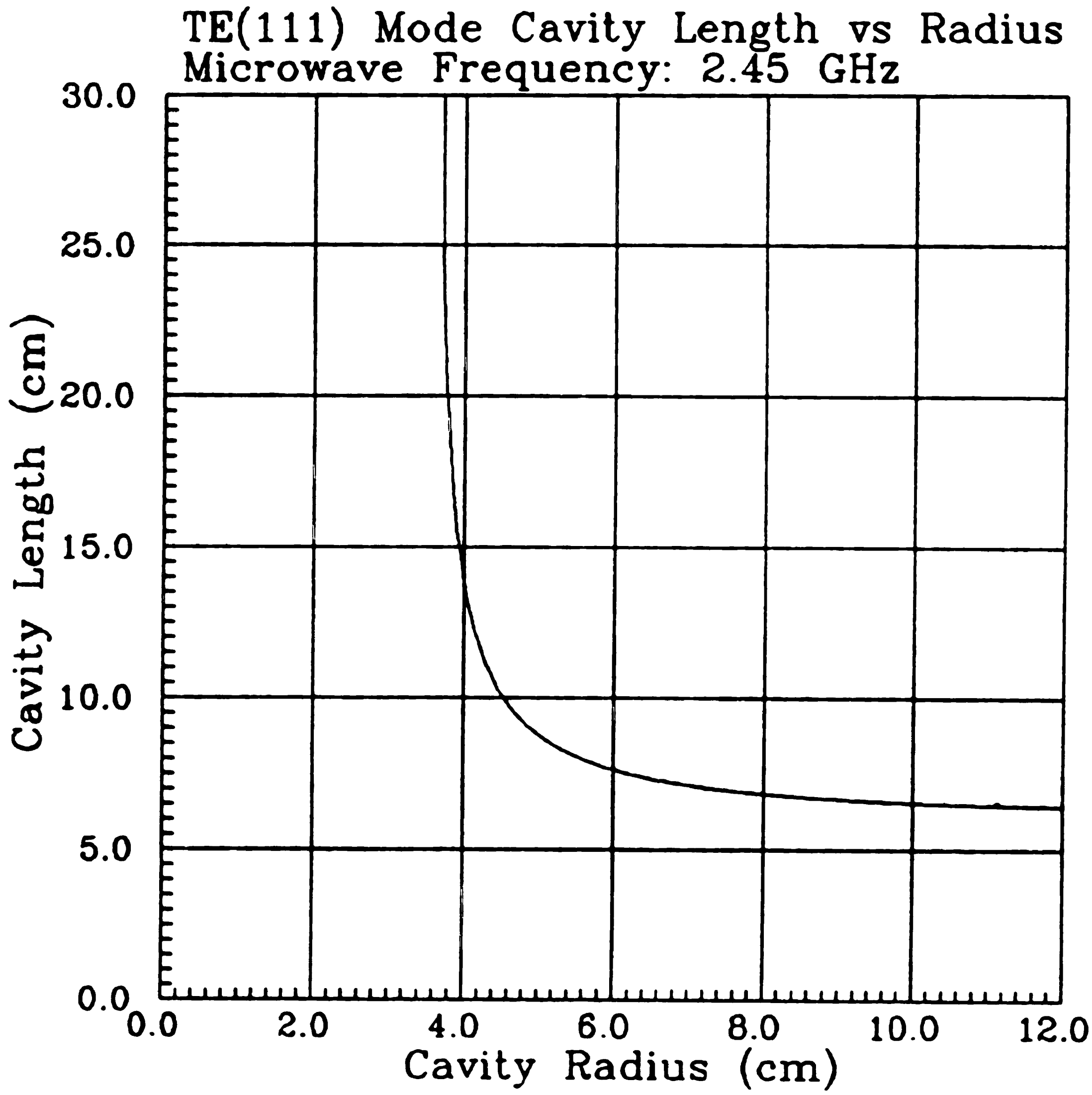

Figure 4.10 Theoretical Cavity Length versus Cavity Radius for the TE_{111} Mode at 2.45 GHz

problems. Microwave supplies at other frequencies are expensive or are not commercially available. The strength of the magnetic fields necessary for ECR increases and thus larger and/or stronger permanent magnets must be used.[56]

4.2.2.2 COAXIAL INPUT LINE

Another aspect of microwave design is the impedance of the coaxial input line. It is important to maintain a transmission line impedance, Z_o, of 50 Ohms throughout the microwave input line. In Equation (4.1) this impedance is specified by the inner conductor radius, R_1, outer conductor radius, R_o, and the dielectric permittivity, ε.

$$Z_o = \frac{1}{2\pi}\sqrt{\frac{\mu}{\varepsilon}}\ \ln\left(\frac{R_o}{R_1}\right) \tag{4.1}$$

In this refined design the coaxial input antenna is .625 inch outer diameter. The radius of the inner conductor is reduced at points where teflon spacers are used to support the inner conductor.

4.2.2.3 RADIAL CHOKES

In certain applications where the ion source is DC biased, the microwave cavity must be DC-isolated from the microwave input supply or from other biased assemblies like single-grid extraction optics.

The DC isolation can be achieved with dielectric gaps in the coaxial transmission line and dielectric gaps between the cavity base plate and grid assembly. Unfortunately these gaps can leak microwave radiation which can cause a health hazard and interfere with external, unshielded electronics. Dielectric gaps along the input coaxial line can cause discontinuities which reflect incident microwave power. Gaps between the extraction optics and base plate orifice can leak radiation, making discharge ignition difficult as microwave energy would no longer be entirely stored within the resonant cavity. Therefore, dielectric gaps must be carefully designed to both prevent radiation leaks and provide adequate DC isolation.

As an example, at the front of the coaxial input probe, a radial, teflon gap, (C in Figure 4.1) is used for DC isolation of the outer conductor and cavity shell from the microwave supply which is usually internally grounded. (See Figure 4.11.) The gap can be modeled as a radial, parallel plane transmission line which is excited by the TEM waves on the coaxial line. The electromagnetic fields in a small gap, d, have orientations E_z and H_ϕ only. The inner radius, R_1 and outer radius, R_2, of the gap boundaries can be specified for a single frequency so that input impedance, Z_i, of the radial transmission structure is approximately zero and the load impedance, Z_L, is approximately infinite. The rf radiation is thus contained by the parallel-plane radial structure. Details of the theory and numerical data for the design of parallel-plane radial waveguides and radial chokes are presented in Reference (57).

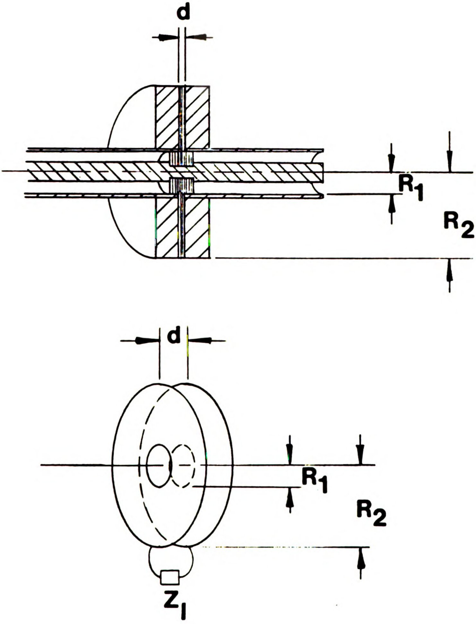

Figure 4.11 Modeling of the Radial Choke on the Coaxial Transmission Line

4.2.3 MAGNET CONFIGURATION

In the second prototype, an arrangement of neodymium-iron-boron permanent magnetics sitting on a soft iron keeper assembly is recessed into the base plate and capped by a brass cover as shown in Figure 4.3. Copper water cooling lines are placed under the magnet keeper and air is circulated around the magnets to keep them cool. The magnet faces have been set 5 mm away from the inside quartz cap face to accommodate the brass cover. Compared with the first prototype with the ten-pole multicusp magnetic field shown in Figure 2.25, the 875 Gauss ECR zones in this design are drawn out of the discharge volume. To compensate for the decreased field strength, the magnets are doubled and a 1/16 inch thick, soft iron back keeper is included to re-enforce the magnetic fields and put ECR zones back into the discharge region.

As displayed in Figure 4.12 the magnets are arranged in a special orientation with respect to the input probe antenna. In practice it is found that the discharge is most easily ignited if the probe axis intersects the gap between two magnetic pole faces. The advantage of this configuration can be explained by first considering the likely orientation of the TE_{111} electric field excited by the probe. (See Section 2.4.1.) Electron cyclotron resonance is driven by electric field components perpendicular to the static magnetic fields. It has been observed that during operation, the discharge becomes brilliant at points "A" along the TE_{111} axis indicating high excitation by ECR accelerated electrons and de-excitation. In this and other ECR microwave-cavity plasma and ion sources at Michigan State University,

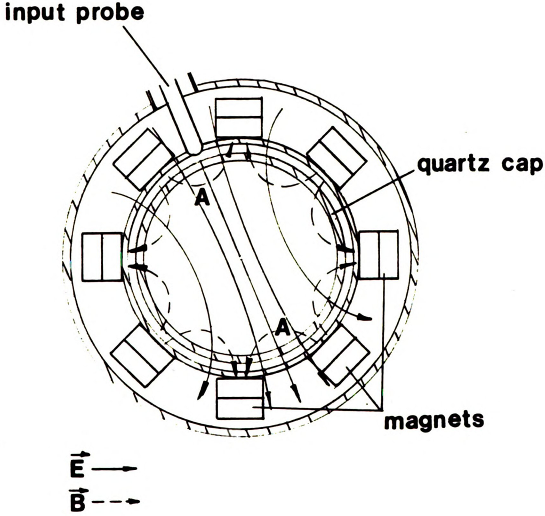

Figure 4.12 Orientation of the Static Magnetic Field with the Microwave Input Probe

the orientation of the multicusp magnetic field with respect to the modal-exciting electric fields is important for ignition and operation.[39]

4.2.4 QUARTZ CAP AND SEALING

The height of the quartz cap has been selected to produce a discharge height of 4.8 cm which is similar to that used in the earlier prototype beam extraction experiments of Chapter 2. As displayed in Figure 4.3, the edge of the cap is designed to seat over a silicone O-ring and O-ring channel (10). This protects the silicone vacuum seal material from direct exposure to the hot plasma. Generally, rubber silicone O-rings can withstand high temperature environments above 400 K, but they can be thermally damaged. Also rubber silicone will outgas in high vacuum applications. Other O-ring materials can be used, such as Viton rubber seals, but such materials may not be able to withstand the high temperature of the quartz. They can become microwave lossy when they initially heat up and then be damaged by additional microwave heating. Compressed metal gaskets or quartz-to-metal seals would be preferable to compressed rubber O-ring vacuum sealing.

4.2.5 COOLING

As mentioned earlier, both air and water cooling have been incorporated into this refined source design. Compressed air is passed through the brass shield, around the magnets, and through a series of 30 holes directed at the quartz face. The air cools the quartz wall and the interior of the cavity by convection, and exhausts out the viewing port window. As ultra-violet radiation from the discharge can produce ozone in the cavity, compressed nitrogen should be used instead of air in order to purge the cavity of oxygen. A copper water cooling line is laid in a channel below the magnets and O-ring sealing channel. The copper line is solder-packed into position and keeps the base plate cool. The air and water cooling allow the ion source to be operated continually for many hours with over 200 Watts of microwave input power and with no thermal damage to the magnets or to the silicone O-ring.

4.2.6 OPERATION OF REFINED ION SOURCE PROTOTYPE

The operation of the new compact prototype ion source is similar to that of the first prototype. The ion source is tuned to the TE_{111} resonant mode. As long as a screen or set of extraction grids electrically shields or chokes microwaves from leaking out the discharge orifice, the source can be easily ignited at discharge pressures below 10 mTorr. The discharge can be ignited with less than 5 sccm of argon gas, or about 4 mTorr discharge pressure, and with less than 100 Watts of incident input power. Other gases such as oxygen and nitrogen may require slightly higher starting pressures and powers.

After ignition, the cavity height, L_s, and input probe length, L_p, are increased until reflected power is reduced to zero. These distances are defined in Section 2.4.1. Again, it is important to have a sharp and stable microwave frequency spectrum to easily ignite and maintain the discharge at low pressure. Table 4-I gives typical tuning parameters for argon. The tuning lengths, L_s and L_p, will vary slightly with different microwave supplies, gas compositions, and operating powers and pressures. An important improvement to recognize in this refined ion source is that the discharge ignites easily at beam extraction discharge pressures without the aid of a Tesla coil or ignition filaments.

4.3 LANGMUIR PROBE EXPERIMENTS

In this section charged-particle density measurements are given for a wide range of pressures and input powers. Electron temperatures from the same data are compared with the theoretical CPΛ and CPα curves described in Chapter 3. Finally, the beam current extracted from the 3.2 cm double-grid extraction optics is predicted using the free-fall diffusion model.

The data presented in this section is reduced from double floating Langmuir probe measurements as discussed in Section 2.3. The only difference is that a new probe with larger dimensions has been constructed for these experiments. (Refer to Figure 2.5 and 2.6 for probe description and location).

probe radius:	.56 mm
probe spacing:	4 mm
probe length:	3.5 mm

TABLE 4-I. SHORT AND PROBE LENGTHS FOR THE TE_{111} OPERATING MODE IN THE COMPACT MICROWAVE ION SOURCE, PROTOTYPE II

Conditions

Gas	Argon
Flow	3.5 sccm
Discharge pressure	2 mTorr
Vacuum pressure	.04 mTorr
Incident power	80 Watts

	Cavity Height (cm): L_s	Probe Length (cm): L_p
THEORETICAL	10.5	-
IGNITION	8.6	.34
TUNED OPERATION	10.6	1.63

A larger probe radius is used to insure that the sheath width, which is approximately .05 to .1 mm, is much less than the probe radius. A probe radius that is smaller than the sheath width would result in ion orbital motion not accounted for by the Langmuir probe theory used in this thesis.

Figure 4.13 shows charged-particle density measurements versus discharge pressure at a single power of 170 Watts. Electron density measurements are similar to the densities measured for the earlier prototype of Chapter 2. (See Figure 2.18.)

Figure 4.14 shows density verses power for two flows of Argon. Refer to Figure 2.13 for the numerical relationship between gas flow and discharge pressure. An unexpected phenomena occurs in these measurements. With a constant flow and constant power, two distinct values of charged particle density can be consistently measured. The bifurcation is a result of two different settings of cavity short and probe position. Line A has a short and probe length of about 10.6 cm and 1.63 cm respectively. Line B has a short and probe length of 10.1 cm and 1.4 cm respectively. Experiments demonstrate that both tunings achieve a matched load; all incident microwave power is absorbed by the loaded cavity. Although no specific measurements have been made to extend line B to higher powers in Figure 4.14, the bifurcation has been noted to occur at these higher powers. Also it is possible to easily jump between these two operating points except at extremely low flows and pressures where the two tuning settings begin to overlap.

The two tuning settings suggest that a change in microwave cavity mode, field strength, or electric field orientation is causing the

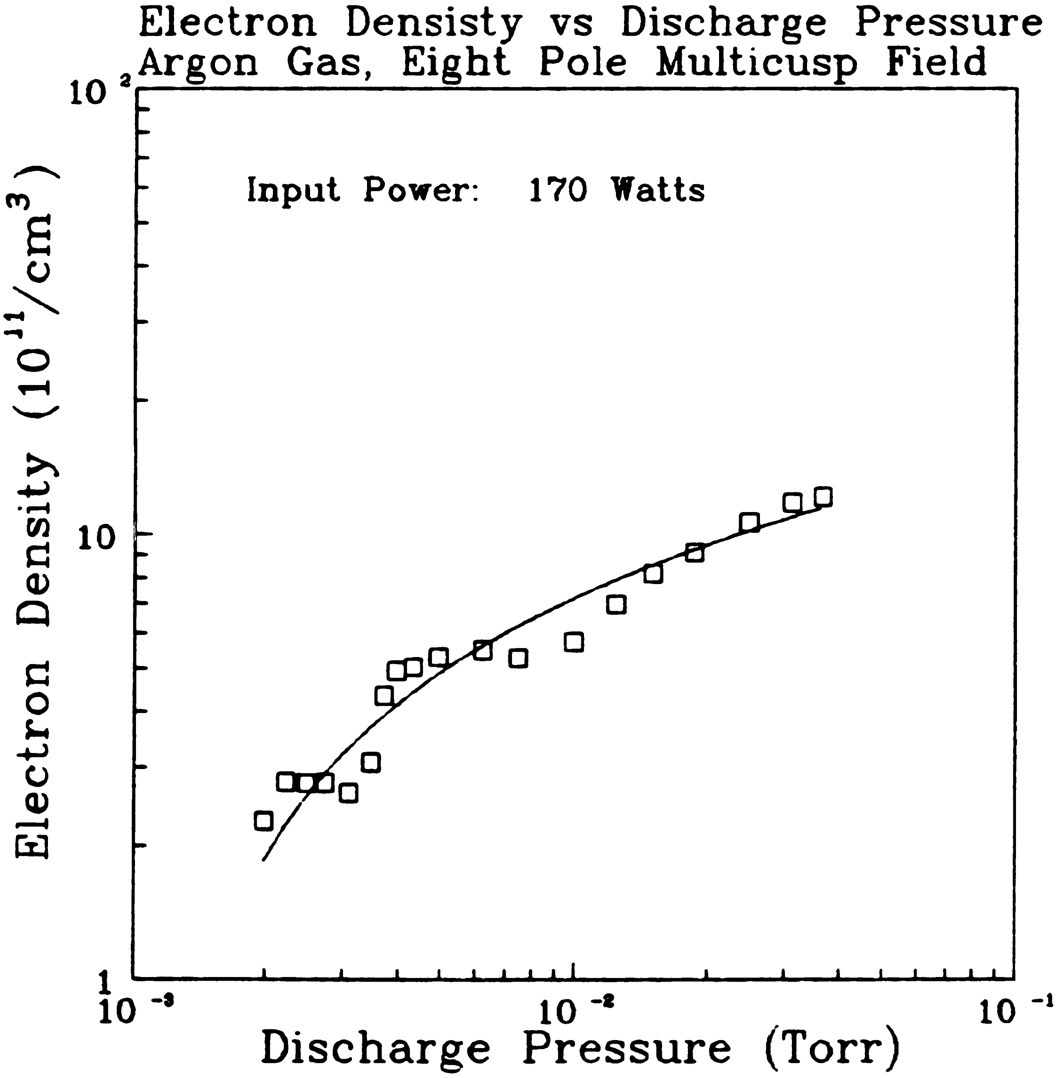

Figure 4.13 Electron Density versus Discharge Pressure for Argon

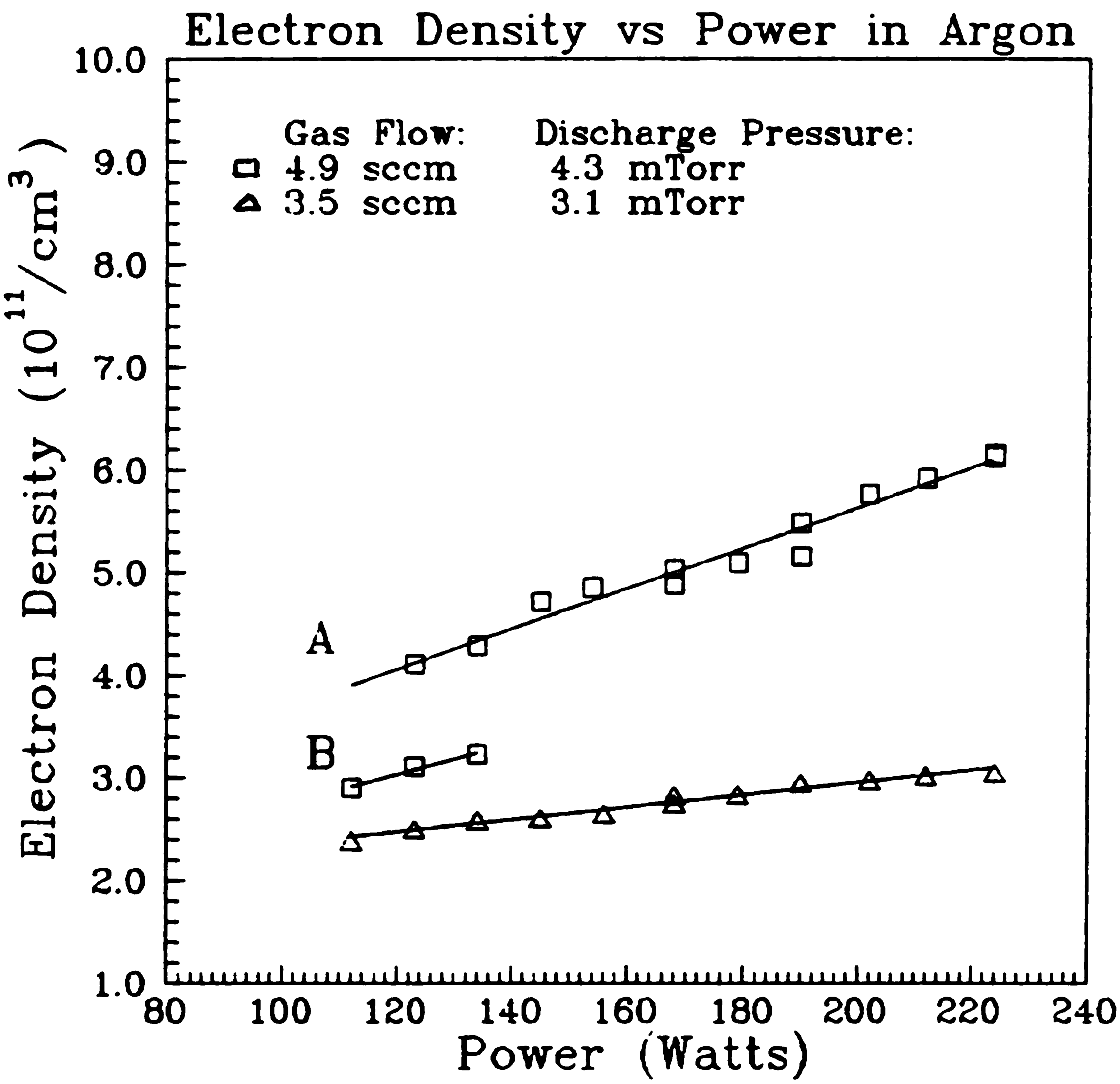

Figure 4.14 Electron Density versus Power for Various Argon Gas Flows

change in density. Input power, P_t, is split between the power absorbed by the discharge, P_a, and power absorbed by the cavity walls, P_b. With a change in the orientation of exciting fields, the input power absorbed is redistributed between the discharge and the cavity walls. Electric field diagnostic holes are not drilled into the cavity walls, so there is no method to monitor modal electric field patterns or intensities as they change with tuning. Without such diagnostic tools it is difficult to ascertain what brings about the "bifurcation" in the density readings.

In Figures 4.15 and 4.16 measured values of electron temperature in Argon are used in conjunction with Schottky and free-fall diffusion curves from Section 3.2. The electron temperatures are correlated with discharge pressures and diffusion lengths and are plotted with the CPΛ and CPα curves and with data from Figure 3.13. The new experimental data re-affirms the conclusion that at low pressure the diffusion process follows Schottky and free-fall diffusion theories, i.e the multicusp static magnetic fields do not greatly influence overall diffusion processes. Experimental data taken at discharge pressures below 4 mTorr show the discharge to follow free-fall diffusion. This suggests that the density and ion flux across the bottom of the discharge are quite uniform, a condition that is highly desirable in broad-beam extraction applications.

Assuming a uniform ion density and flux, an estimation of the beam current from the 47% transparency double-grid (Section 2.4) can be predicted. Equation (2.9b) is used to calculate the total beam flux to the 8.1 cm^2 surface, the area of the 3.2 cm diameter extraction grids. The predicted beam current is the product of the ion flux and

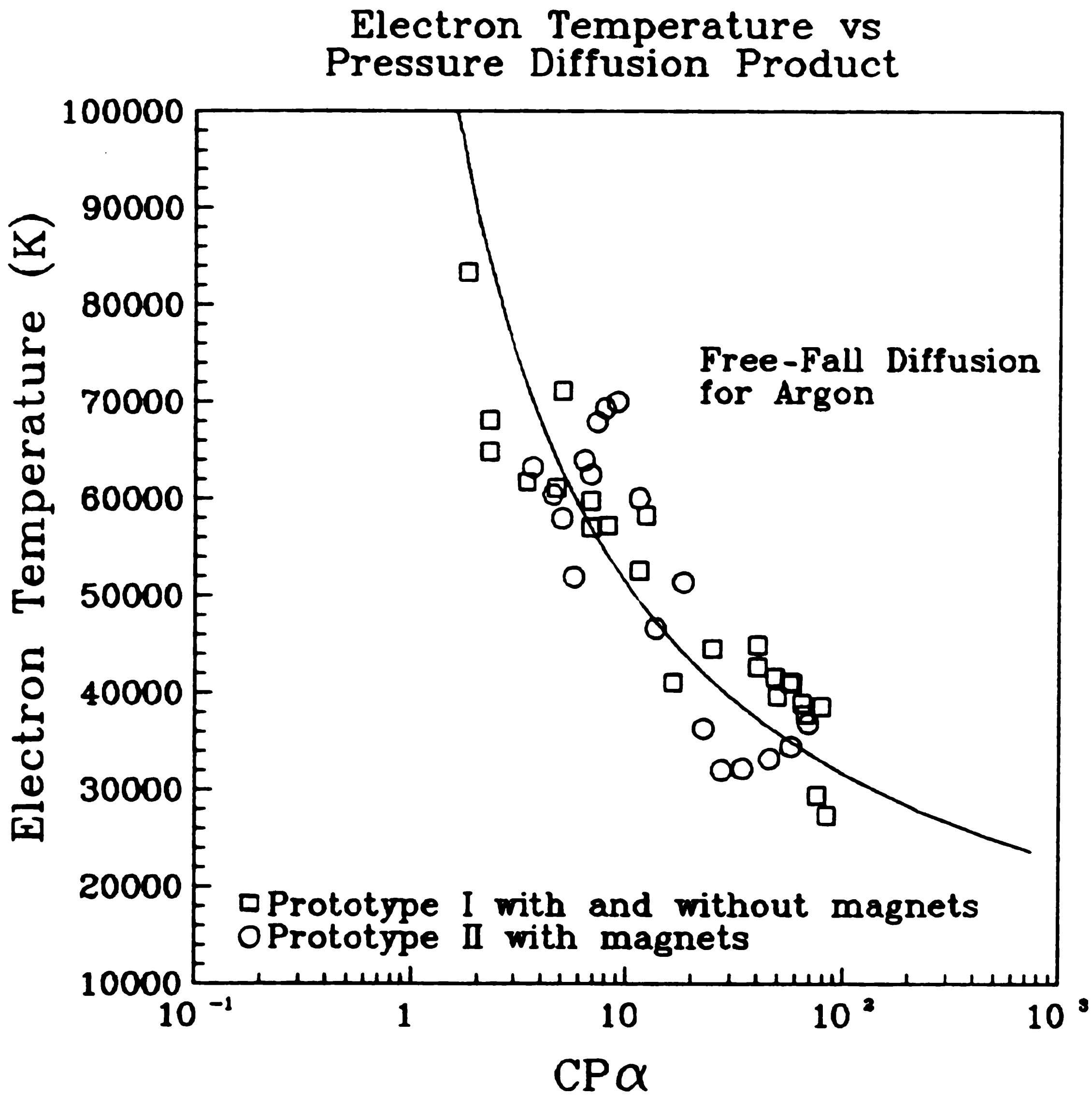

Figure 4.15 Free-fall Diffusion Curve for Prototypes I and II

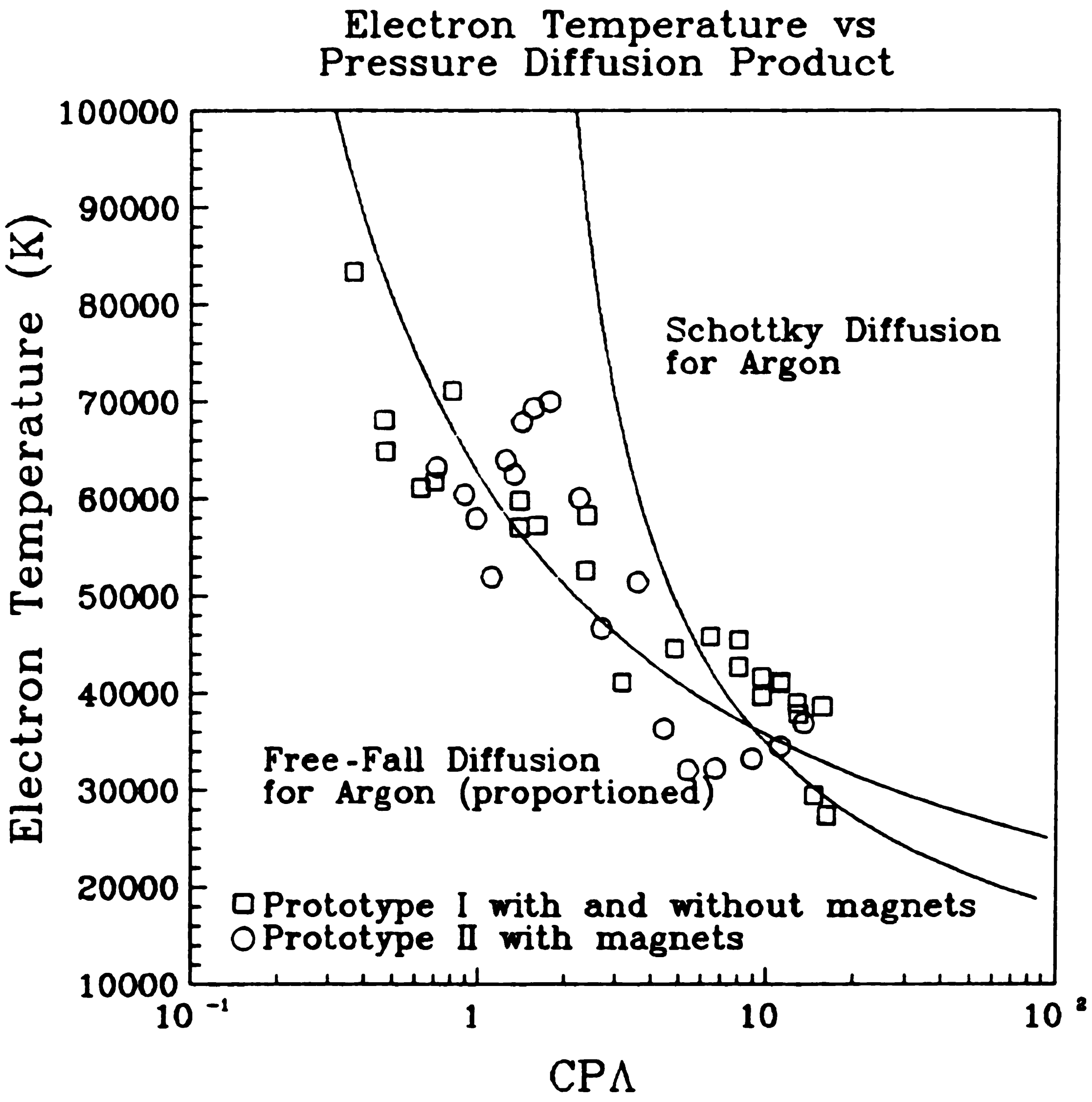

Figure 4.16 Schottky and Free-fall Diffusion Curves

for Ion Source Prototypes I and II

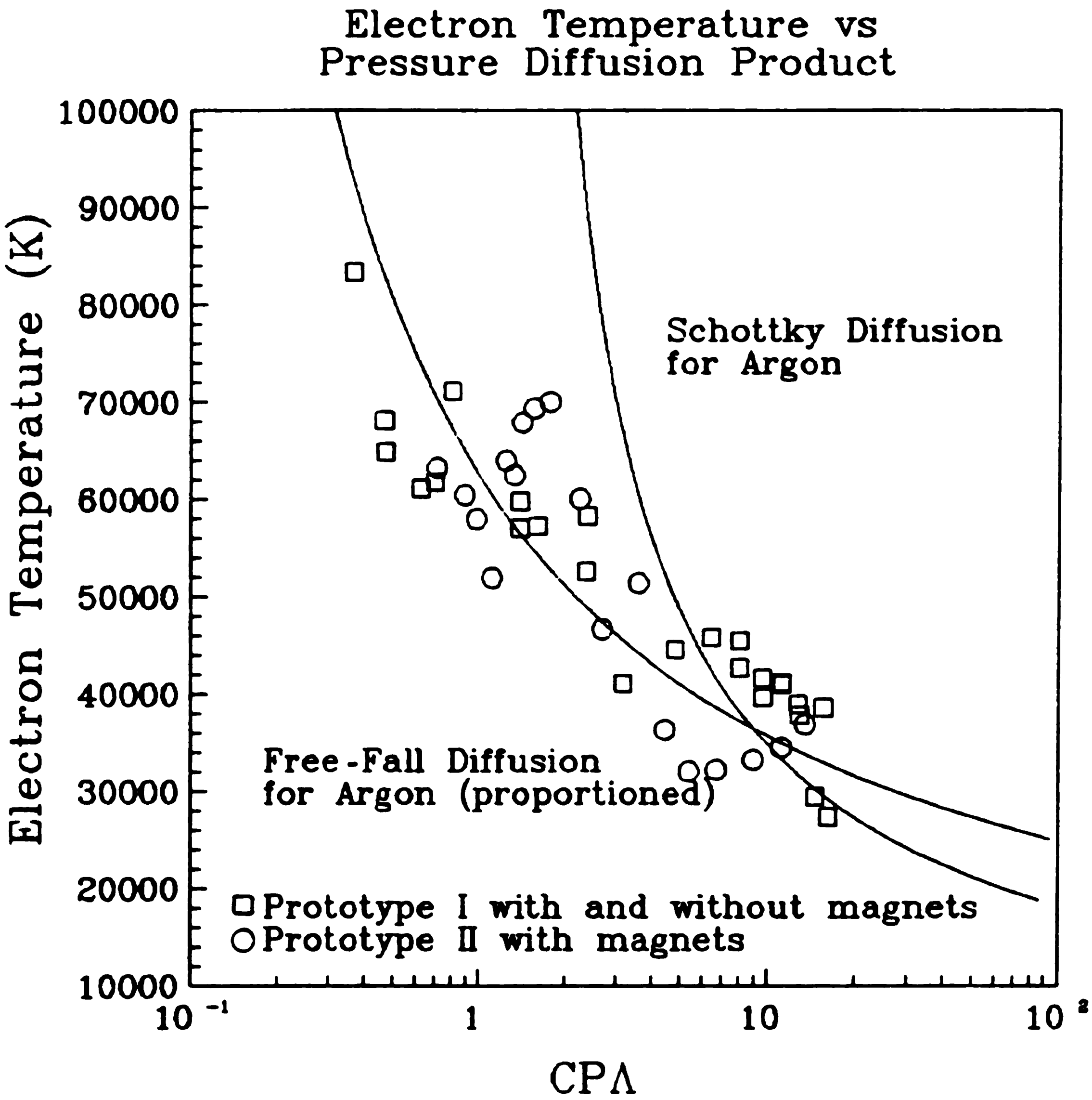

Figure 4.16 Schottky and Free-fall Diffusion Curves
for Ion Source Prototypes I and II

the transparency of the grid. For argon at 3.5 sccm, (Figures 4.13 and 4.14), electron density of 2.5×10^{11} to 3×10^{11} ions/cm^3, and electron temperature of 60,000 K, the predicted extractable beam current is 33 to 40 mA for input powers ranging from 110 to 220 Watts.

4.4. ION BEAM EXTRACTION

4.4.1 FARADAY CUP ARRAY

The extraction grids and circuit used in these studies are the same as those described in Section 2.3.4. However, a traversing, sixteen-channel, Faraday cup line array is included in the experiment to examine ion beam current profiles. The Faraday cup array and traversing mount is shown in Figure 4.17. The aluminum Faraday cups are long and narrow to geometrically suppress secondary electron emission produced by high energy ion bombardment. The cups are situated below a grounded stainless steel target plane. In the extraction experiments presented in this thesis the grounded plane is located 19.5 cm below the extraction grids of the ion source.

The circuit of the Faraday cup array is shown in Figure 4.18. The current from each cup is passed across a 10 Ohm resistor and the resulting voltage is amplified. Since the cups must be continually grounded, sixteen independent amplifying circuits are needed to monitor the beam. The sixteen channels are de-multiplexed and then sampled by a computer. Faraday cup array signals are displayed and/or recorded to monitor the beam profile while changing the operating

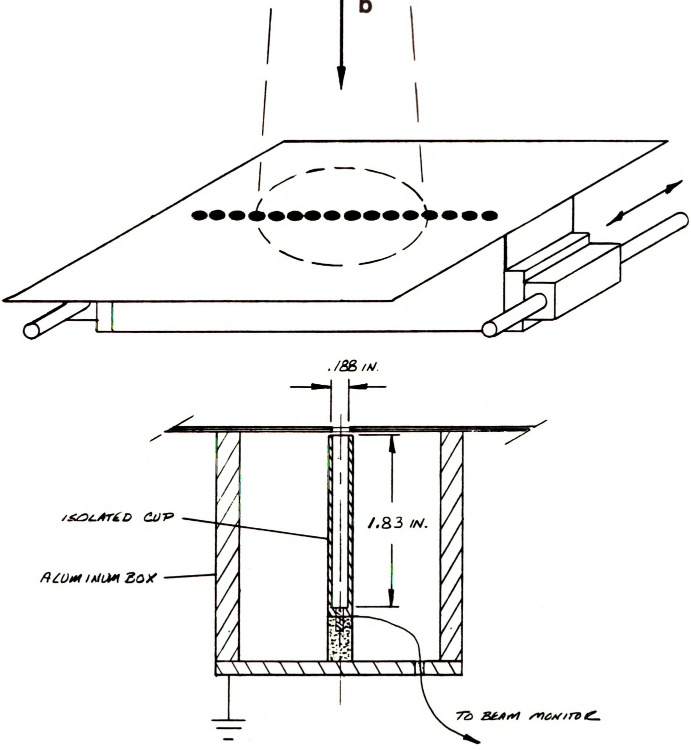

Figure 4.17 Sixteen Channel Faraday Cup Array

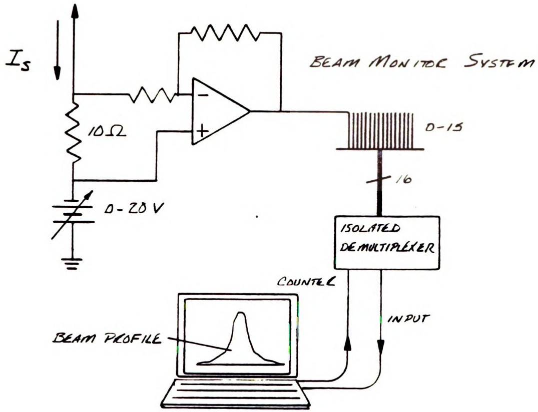

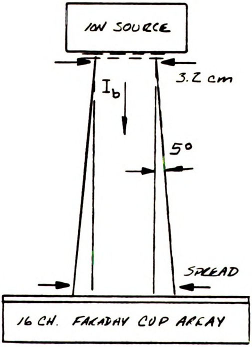

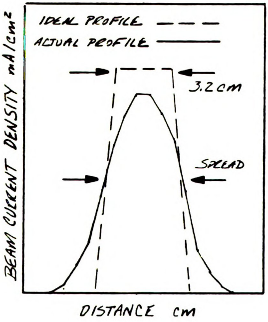

Figure 4.18 Faraday Cup Circuit and Profile Monitoring System

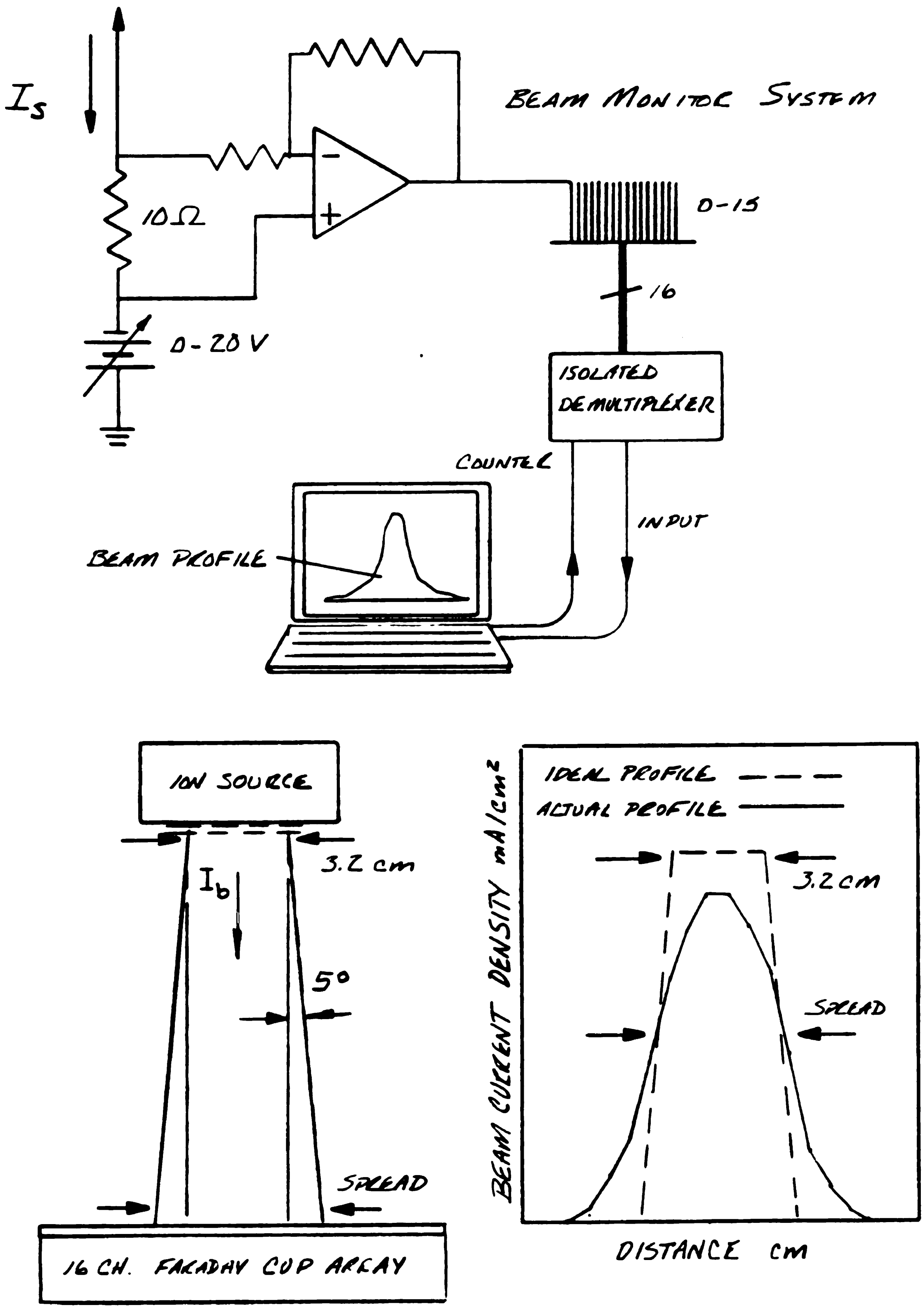

Figure 4.18 Faraday Cup Circuit and Profile Monitoring System

parameters of the ion source, i.e. extraction potential, input power, gas flow, etc. It is desirable to have a beam that has an even profile across its mid-section. (See the sample profile in Figure 4.18.) An ideal beam should have its half-peak-current density within five degrees of divergence of the vertical axis. Furthermore, the beam current profile can be integrated to calculate the total beam current[40] and thus verify the ion beam current measured by the ammeters in the extraction circuit. (See Figure 2.9.) Typically the integrated beam current is 10% less than the total beam current read from the ammeters. The discrepancy is quite accurately accounted for by charge exchange processes in the beam path.[40]

4.4.2. DOUBLE-GRID ION BEAM EXTRACTION EXPERIMENTS WITH PROTOTYPE II

Beam extraction experiments were performed in argon, oxygen and nitrogen at powers from 150 to 250 Watts and flows from 1 to 5 sccm. For these flows the vacuum environment pressures, P_{bj}, ranged from $2x10^{-2}$ to $7x10^{-2}$ mTorr. No tungsten neutralization was used in these experiments. Ion beam profiles shown in this report diverge more than usual because of the space charge effects within the unneutralized ion beam shaft. Figures 4.19 through 4.22 show the results for argon. The input power was higher than in the beam extraction studies performed in Chapter 2. Beam currents exceed 40 mA and power cost ranges between 3000 and 5000 Watts/ Beam Ampere.

Figure 4.22 shows ion beam profiles for various extraction

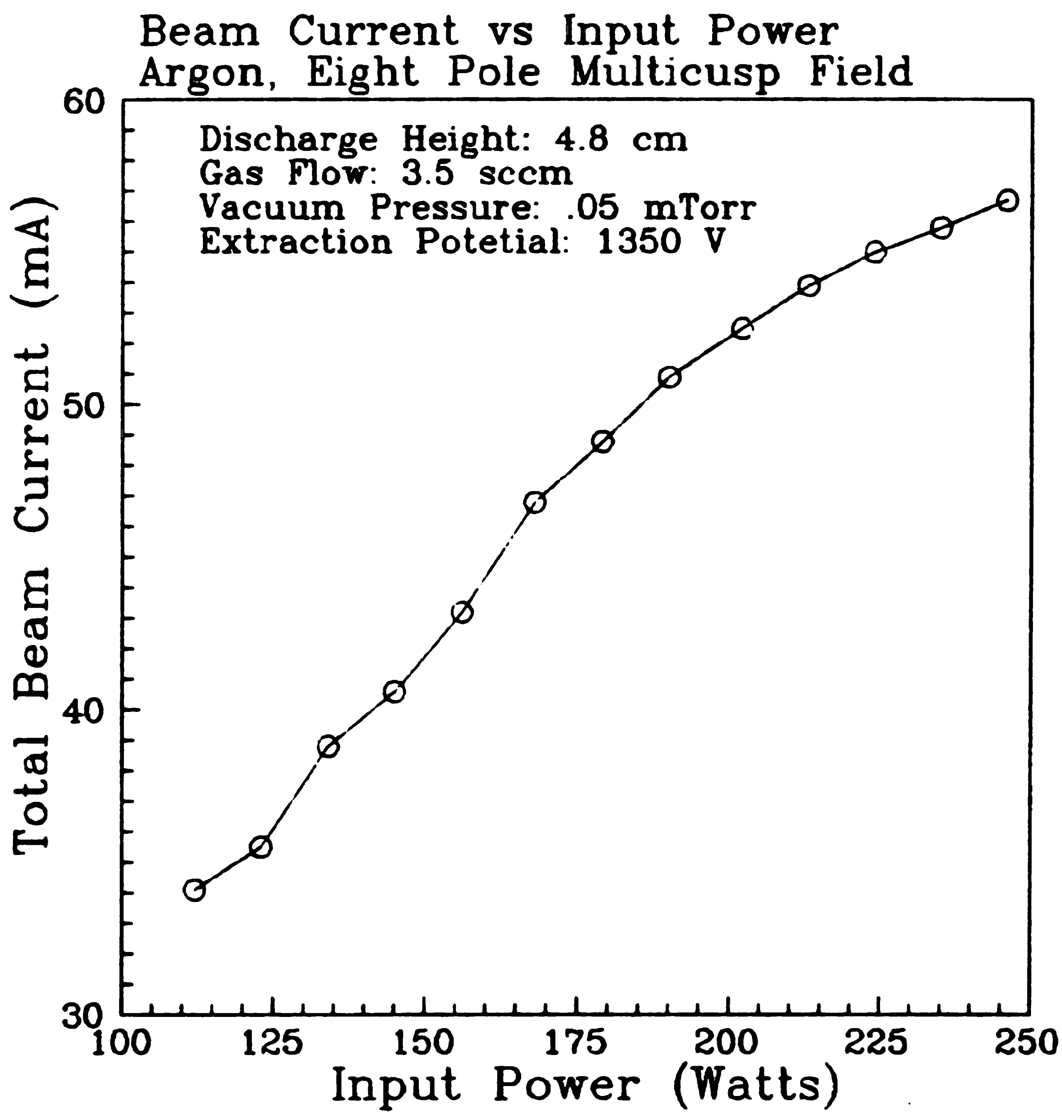

Figure 4.19 Total Beam Current versus Input Power for Argon

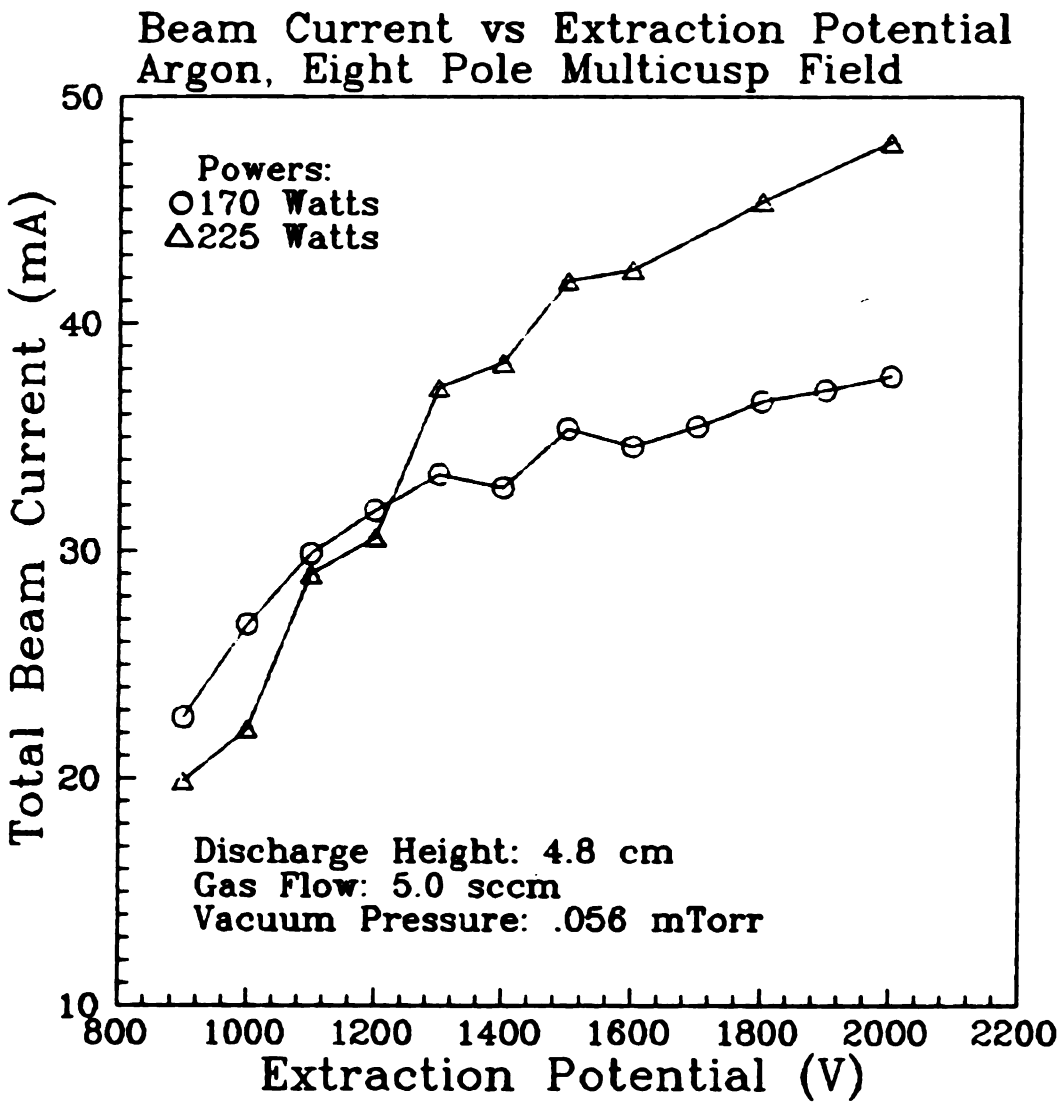

Figure 4.20 Total Beam Current versus Extraction Potential for Argon

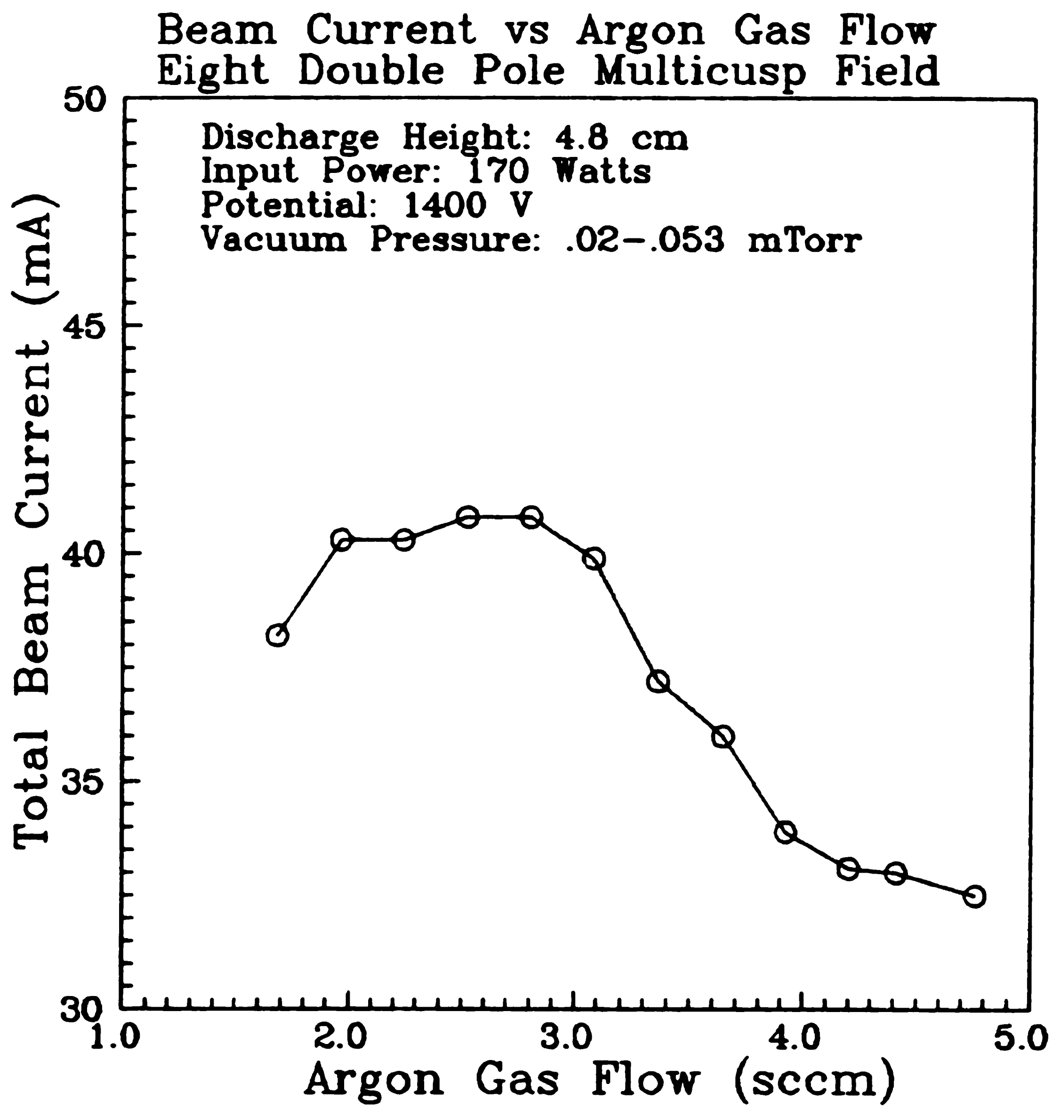

Figure 4.21 Total Beam Current versus Argon Input Gas Flow

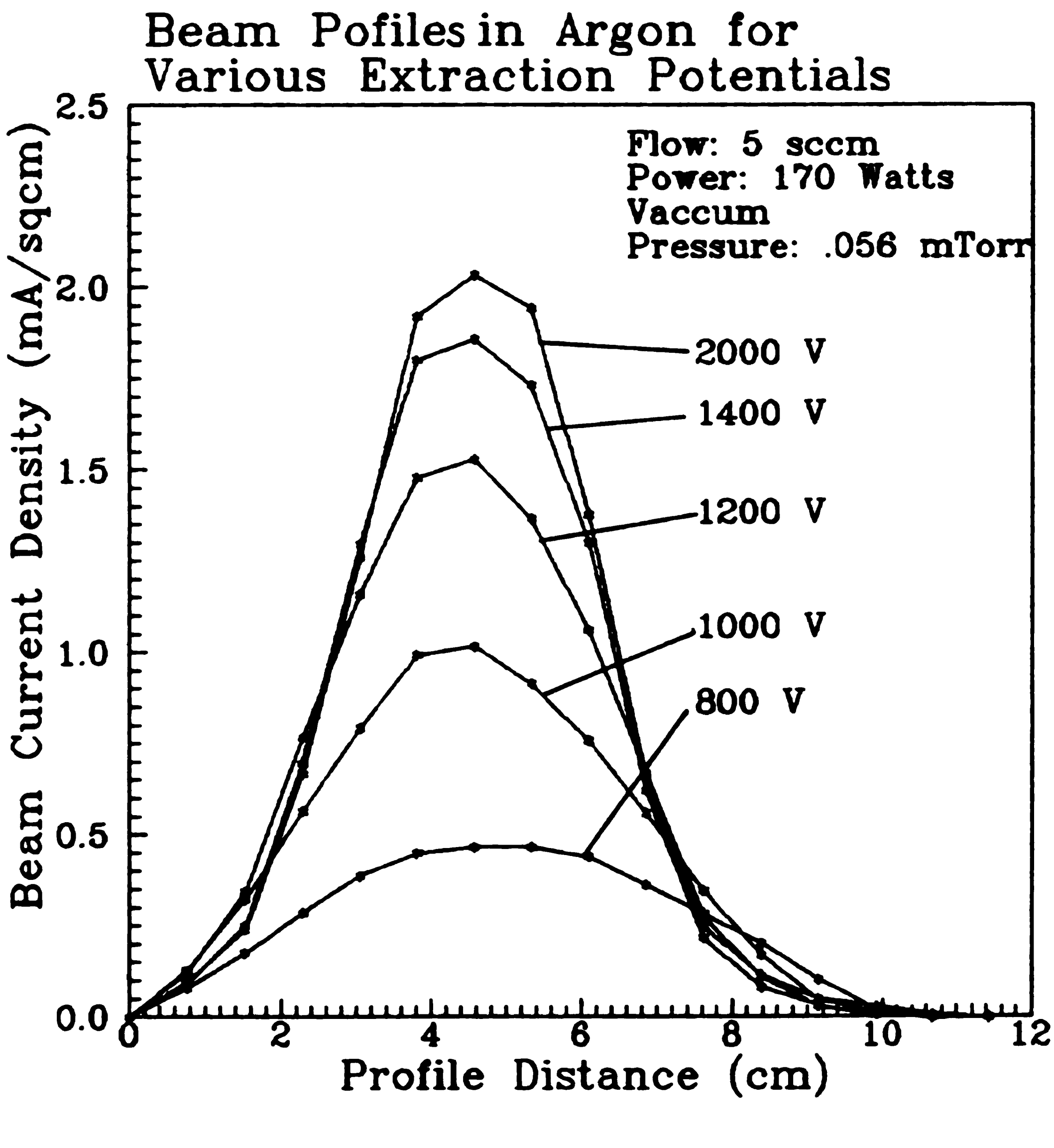

Figure 4.22 Ion Beam Current Density Profiles for Argon

energies. The profiles show that the grids are slightly misaligned and direct the beam slightly off center. The beam was focused by varying the negative acceleration potential, V_g, on the second grid. (See Figure 2.9.) These beam profiles represent the best-collimated or best-focused profile that was achieved for a given extraction potential, but do not necessarily represent the highest beam current that could have be drawn by the double-grid extraction optics.

Figures 4.23 through 4.27 show oxygen ion beam currents measured for variations in extraction potential, flow and input power. Figures 4.22 and 4.23 show total ion beam currents and beam current profiles for a number of extraction potentials. Although the ion beam current steadily rises with extraction potential, uniform beam current density degrades after 1400 V as shown in Figure 4.23. This is to be expected of double-grid extraction optics when excessive discharge ion current is available for extraction.[58]

In Figure 4.26, two sets of oxygen ion beam current measurements are given for two different acceleration potentials, $V_g = -30$, and $V_g = 0$. Beam density profiles for certain points in Figure 4.26 are shown in Figure 4.27. These figures show that the ion beams with the greatest currents do not necessarily have the most even beam current density profiles. Indeed beams with the best performance in terms of total beam current have quite divergent profiles. The grids were originally designed for an oxygen ion beam at 1000 V with 30 mA total extracted beam current. It is apparent by these experiments that the grids should be re-aligned and/or re-designed to handle ion beam current densities in excess of $10 mA/cm^2$.

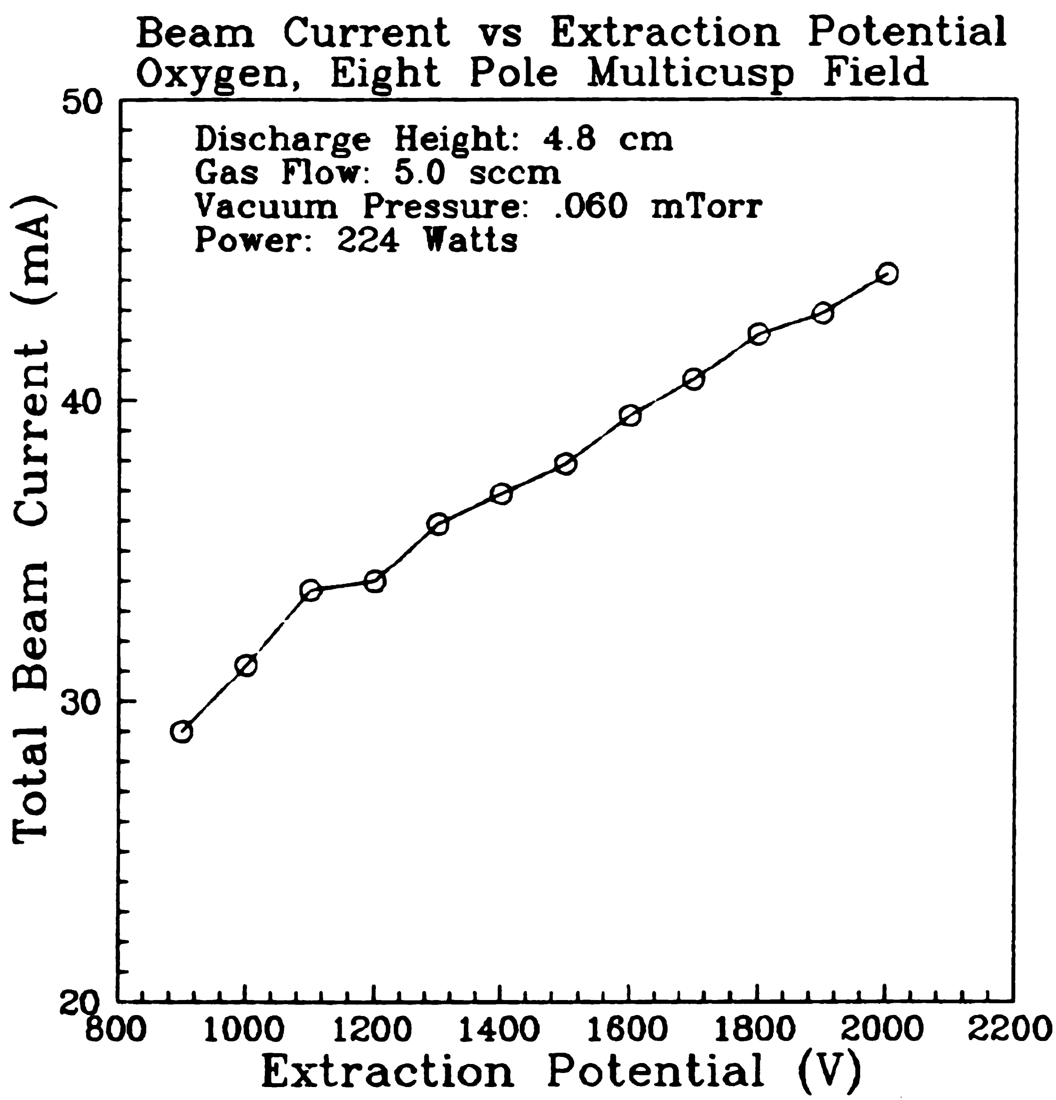

Figure 4.23 Total Beam Current versus Extraction Potential for Oxygen

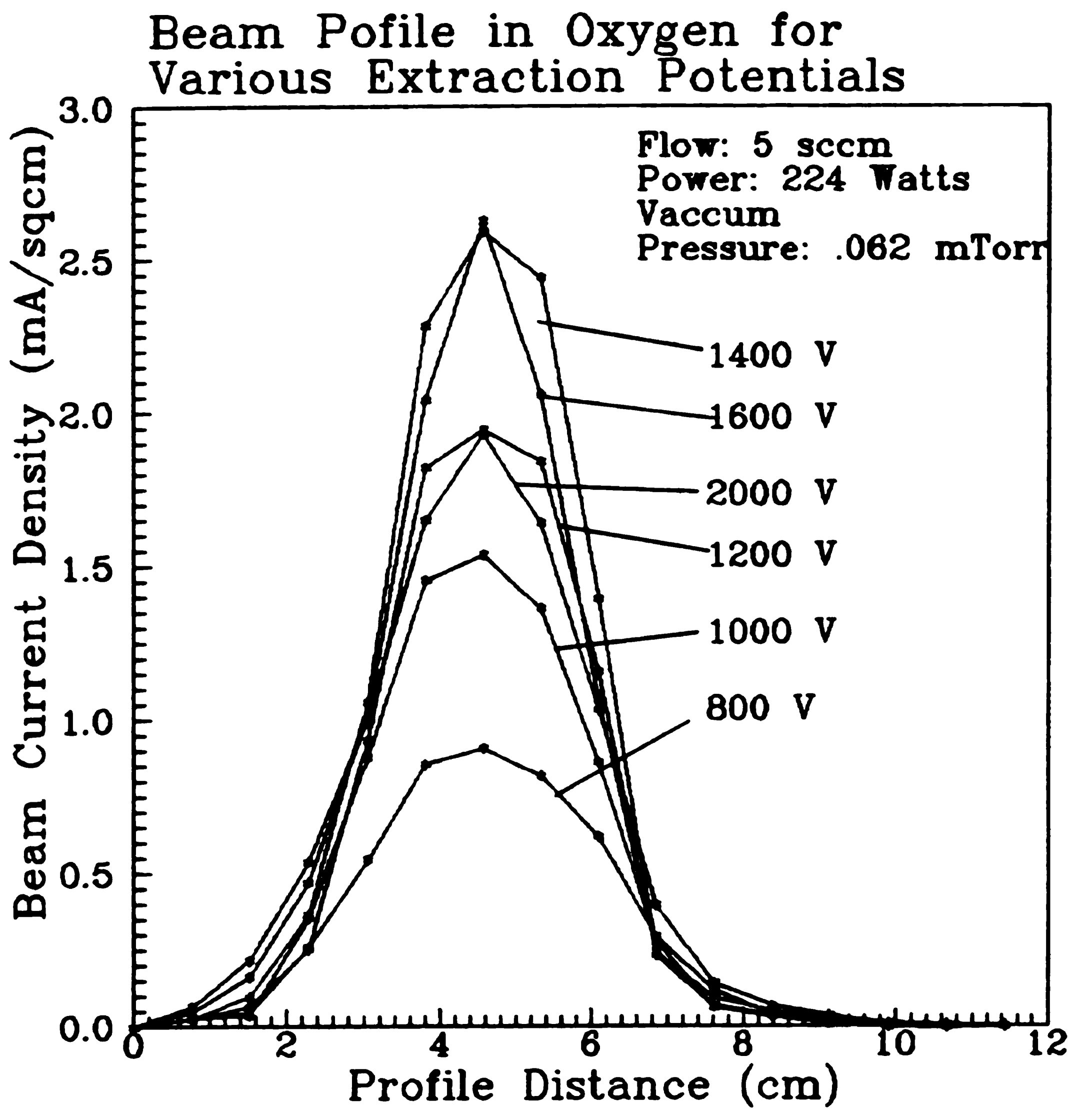

Figure 4.24 Beam Current Density Profiles for Oxygen

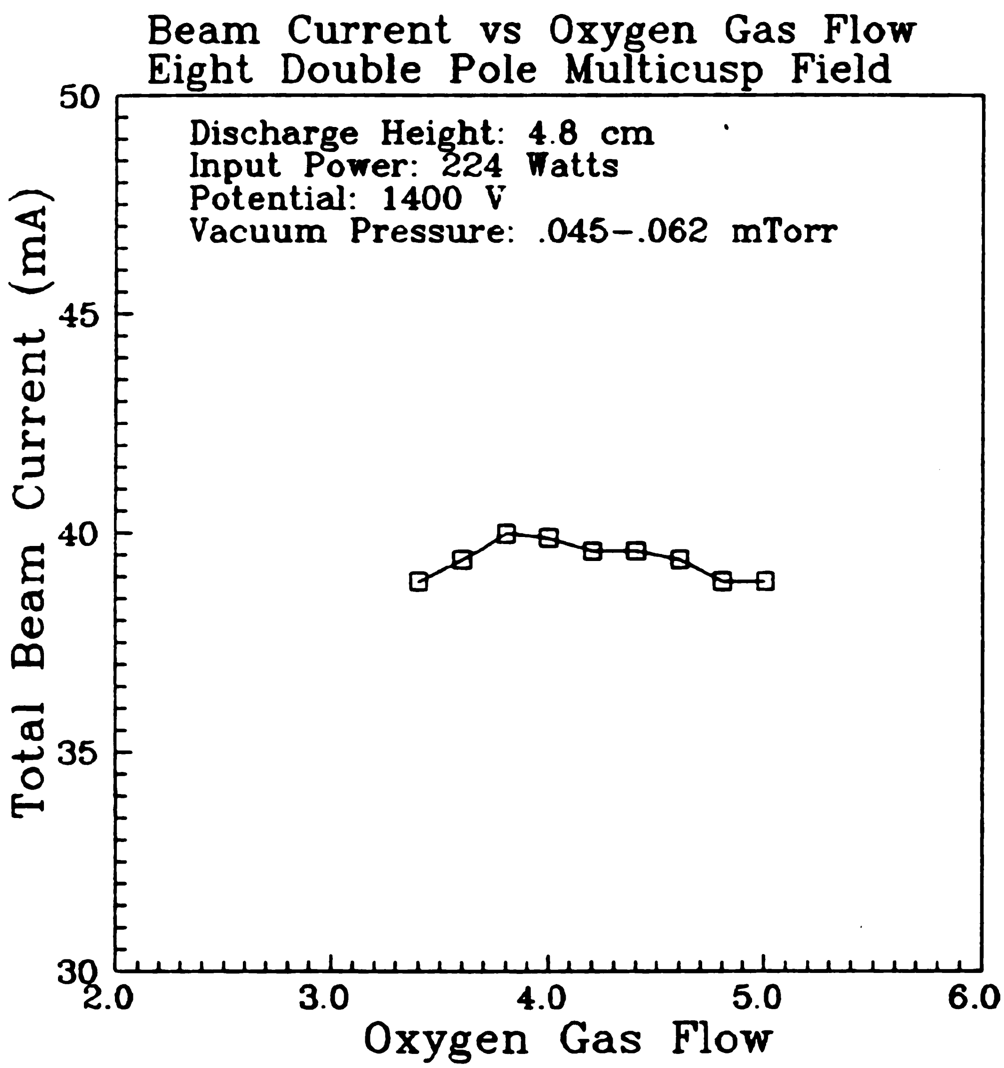

Figure 4.25 Total Beam Current versus Oxygen Input Gas Flow

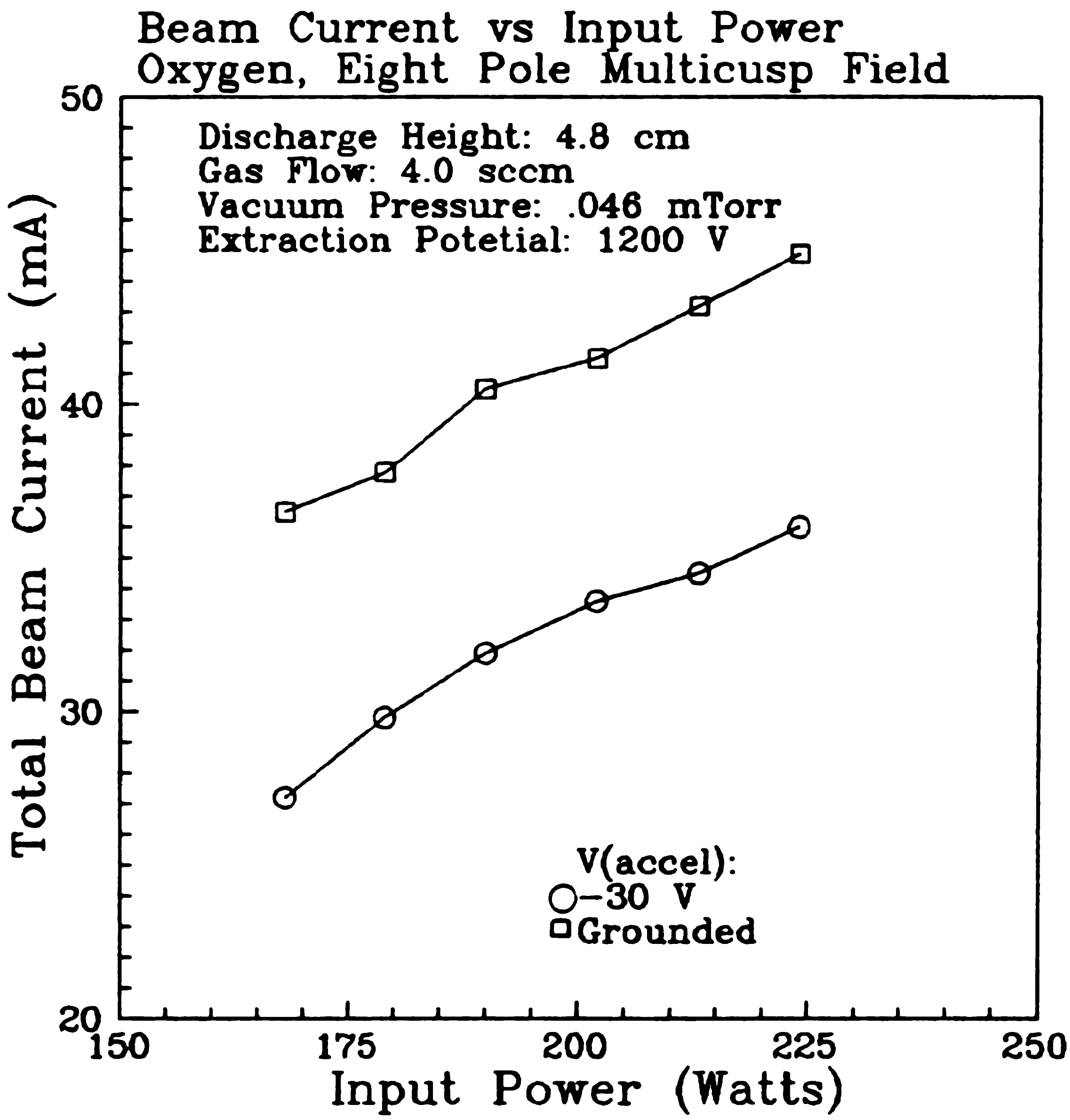

Figure 4.26 Total Beam Current versus Power for Oxygen

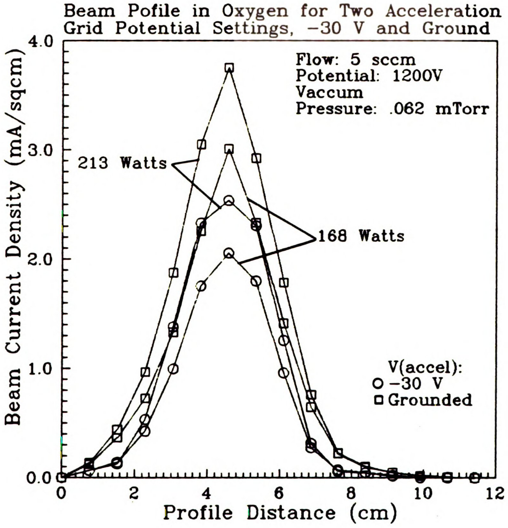

Figure 4.27 Beam Current Density Profiles for Oxygen with Two Acceleration Potentials

Finally, Figures 2.28 and 2.29 show beam extraction results for Nitrogen. The beam currents are similar to those obtained from the first ion source prototype. Again these current measurements were taken for the best collimated beam profile and do not represent the highest beam currents possible for a given set of operating conditions.

4.4.3. DESIGN CONSIDERATIONS FOR EXTRACTION OPTICS

In Section 2.4.4, it was found that the discharge was too dense to extract a well-focused ion beam from the silicon grid or other screen grids. In order to further pursue this topic, the hole size of any single-grid extraction optics must be specified for a given discharge density. In the past such specifications have been made by extensive computer modeling of accelerated ion trajectories or by empirical trial and error. Various designers of single-grid optics have given a basic design criterion for single grids: the minimum discharge sheath width adjacent to the extraction boundary should be one to two times the maximum hole size of the single-grid optics.[59] This criterion can be expressed in terms of the plasma Debye length, λ_D, since the plasma sheath width is typically several Debye lengths.[48] The Debye length is given as

$$\lambda_D = \left[\frac{kT_e\varepsilon_o}{n_e e^2}\right]^{1/2} . \qquad (4.2)$$

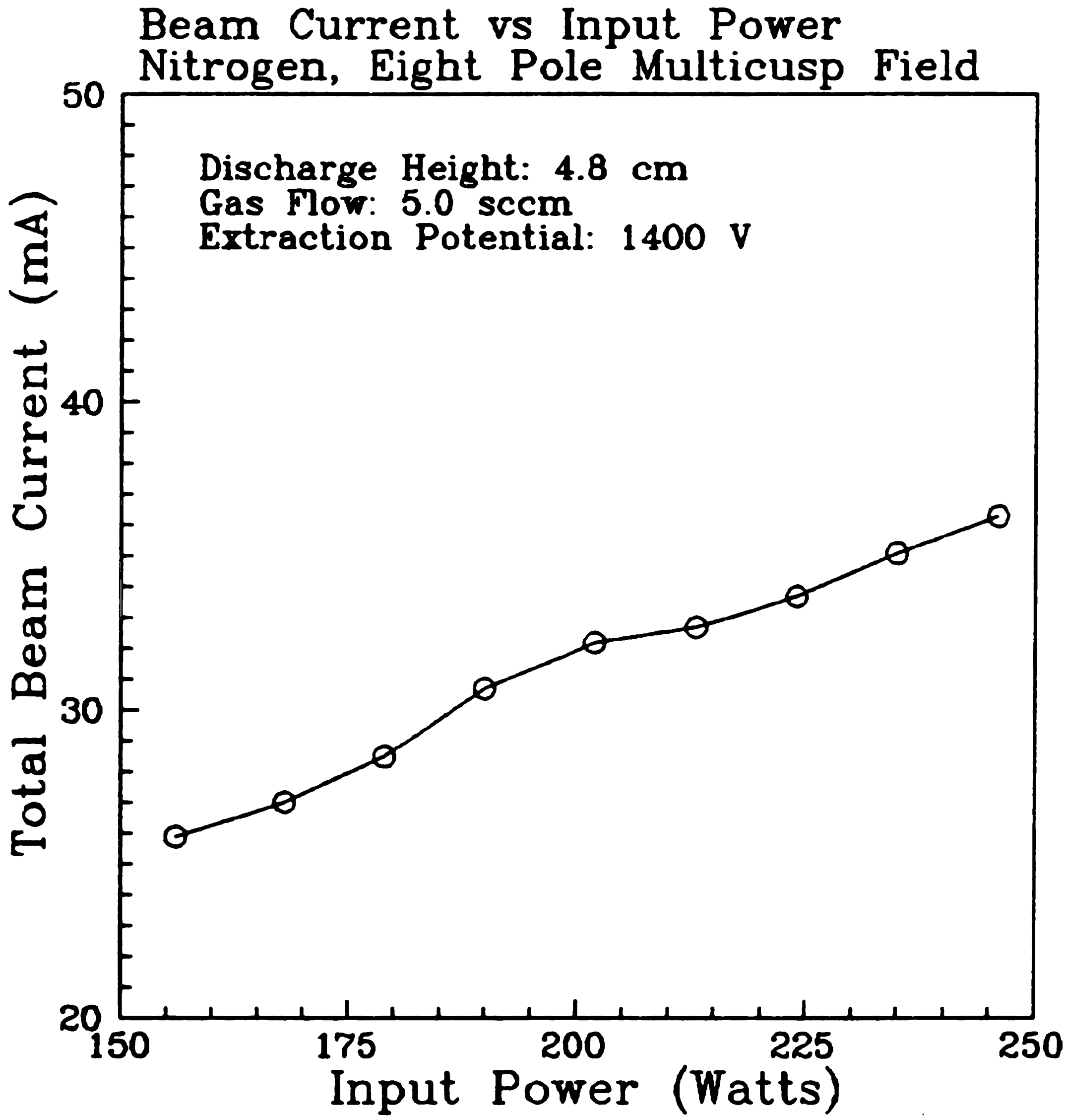

Figure 4.28 Total Beam Current versus Power for Nitrogen

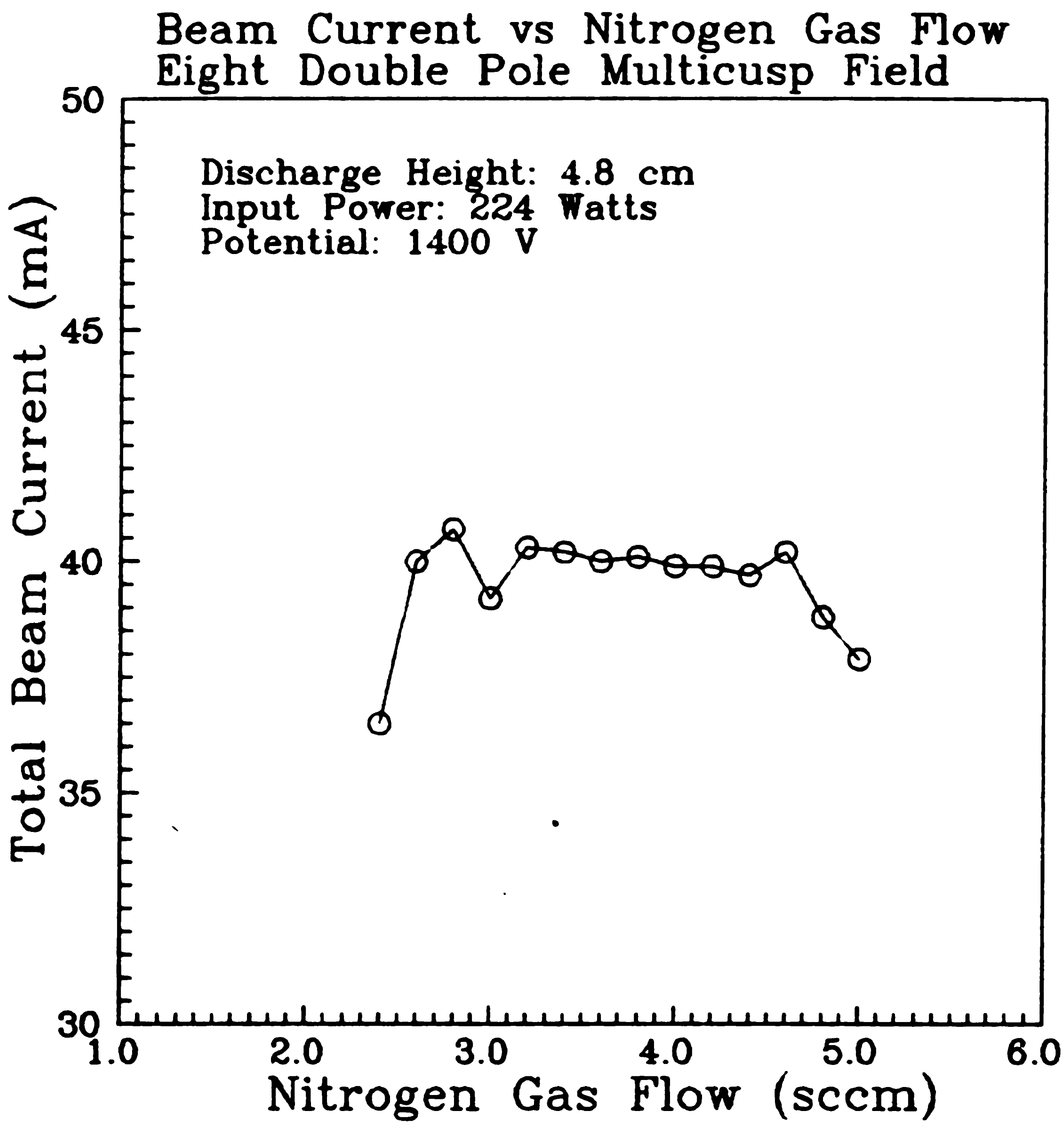

Figure 4.29 Total Beam Current versus Nitrogen Input Gas Flow

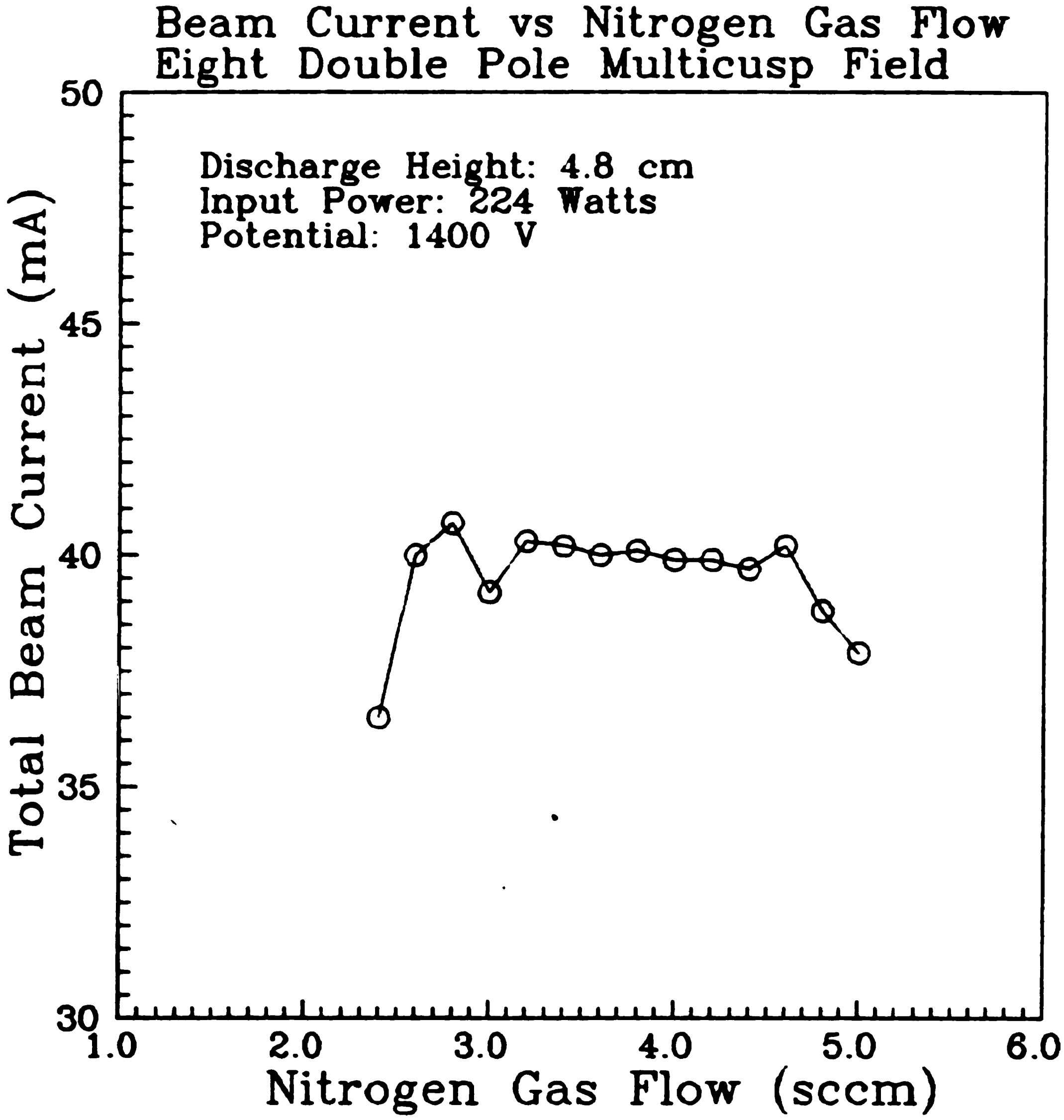

Figure 4.29 Total Beam Current versus Nitrogen Input Gas Flow

The maximum single-grid hole size should be no larger than five times the Debye length.[59,60]

For a discharge density of $4x10^{11}$ions/cm^3 and electron temperature of 60,000 K, λ_D is 0.027 mm. The diameter of extraction holes must be near .1 mm for good focusing. Thus a high transparency tungsten screen mesh of 200 x 200 lines per inch could be used to extract a well collimated beam. Ridged graphite or solid metal single grids with such small holes and high transparency may be too difficult and/or expensive to commercially manufacture.

Future broad beam ion source demonstrations with this refined compact ECR microwave-cavity ion source depend upon the development of high-transparency, small-aperture extraction optics or other novel extraction techniques (such as divergent magnetic fields).[44] In the design of conventional extraction optics, four parameters must be specified: the ion current density to the grids, the approximate plasma sheath width, the desired energy of the ion beam, and the allowed divergence of the beam. Given these parameters, the geometry and the spacing of the grid may be adjusted to accommodate a proposed application. Unfortunately there is no one grid design which will operate effectively over a wide range of beam current densities and/or energies. As the beam operating parameters are changed, new designs of extraction optics are required to optimize the performance of the ion source.[60] The reader is referred to a number of publications and texts which discuss ion extraction and grid design.[59,61-65] Invariably, future studies of ion extraction systems must concentrate on the formation of the plasma sheath around walls and grid boundaries and on computer simulations of ion trajectories through extraction apertures.

CHAPTER V

SUMMARY AND CONCLUSIONS

5.1 SUMMARY OF ION SOURCE PERFORMANCE

A compact, ECR microwave-cavity ion source operating at a frequency of 2.45 GHz, has been demonstrated to produce ion current densities in excess of 10 mA/cm^2 with less than 200 Watts of input power. Beam current densities depended on the transparency of ion extraction optics and extraction potential. Argon, oxygen, and nitrogen beam currents of over 40 mA at potentials from 1000 to 2000 V were extracted from a 3.2 cm beam-diameter, 47% transparent, double-grid extraction system. The power cost for these experiments was between 3000 and 5000 Watts/ Beam Ampere which was a two fold improvement in efficiency over Dahimene's beam extraction studies.[9] Low energy, single-grid extraction could not be demonstrated because of the unavailability of ion extraction optics with sufficiently small extraction apertures. The physical size and weight of the microwave-cavity ion source was reduced, and the operating life-time was extended to that of the extraction optics. In the final prototype design the start-up, steady operation, and power capacity of the instrument at pressures below 10 mTorr was significantly improved.

Experimental measurements of electron temperature were shown to agree with simple diffusion models. These models suggested that the multicusp magnetic field does little to change the overall diffusion multicusp magnetic field does little to change the overall diffusion processes of the discharge although diffusion may be altered locally within the discharge. With the application of Schottky and free-fall diffusion models, the power balance equation of the electron sub-gas was examined to predict the power necessary to maintain a discharge of a given volume, pressure, and density.

5.2 FUTURE RESEARCH

Topics for future research can be divided into two categories: (a) microwave discharge studies, and (b) further design improvements and applications.

(a) Spatial charged-particle density and electron energy measurements should be made to characterize the performance of the discharge and aid in the development of discharge models. Within the cavity, electric field patterns and intensities should be monitored to investigate microwave power absorption and related discharge phenomena, such as the bifurcation in charged-particle density discussed in Section 4.3. Refined discharge models should include predictions of plasma sheath formation. Characterization of the plasma sheath is important in the design of single- and multiple-grid extraction optics.

(b) Further design improvements are warranted. The microwave input probe which is mounted on the side of the cavity does not allow the ion source to be adapted to conventional vacuum ports. The input probe could be moved to the top of the ion source and placed conjunction with the sliding short assembly. Throughout these experiments the ion source is biased at high potential. It would be highly advantageous to DC-isolate the discharge, gas feed line, and extraction optics from the cavity. Extraction optics must be carefully re-designed with knowledge about the plasma sheath, extraction grid material, and the behavior of the beam-plasma. These proposed changes and studies should be incorporated into future research of the microwave ion sources.

Application defines design. Indeed the future of this compact, ECR microwave-cavity ion source depends on demonstrations and new designs directed at specific applications. Whether it be propulsion, sputtering, ion implantation, etc., knowledge of other electrical and mechanical systems and processes must be incorporated into future microwave ion source research.

LIST OF REFERENCES

LIST OF REFERENCES

1. Asmussen, J., and Root, J., "Ion Generation Apparatus and Methods for the Use of," U. S. Patent, No. 4,507,588, Mar. 26 (1985).

2. Asmussen, J., Reinhard, D., and Dahimene, M., "Improved Plasma Generating Apparatus Using Magnets and Method," U. S. Patent, No. 4,727,293 Feb. 23 (1988).

3. Asmussen, J., Root, J., "Characteristics of a Microwave Plasma Disk Ion Source," Applied Physics Letters, 44, 396, (1984).

4. Root. J., and Asmussen, J., "Recent Work on a Microwave Ion Source," presented at the JSASS/AIAA/DGLR 17th International Electric Propulsion Conference, Tokyo (1984).

5. Root, J., and Asmussen, J., "Experimental Performance of a Microwave Cavity Plasma Disk Ion Source," Review of Scientific Instruments, 56, 1511 (1985).

6. Dahimene, M., Root, J., Mahoney, L., and Asmussen J., "Characterization of a Microwave Generated Plasma," presented at the IEEE 1986 International Conference Plasma Science, Saskatoon, Canada, IEEE, 2D1, 26 (1986)

7. Dahimene, M., Mahoney, L., and Asmussen, J., "An Electron Cyclotron Resonant Multicusp Magnetic Field Microwave Plasma Source for Electric Propulsion," presented at The 19th AIAA/DGLR/JSASS International Electric Propulsion Conference, Colorado Springs, Colorado, May, 1986, AIAA-87-1015.

8. Dahimene, M., Asmussen J., "The Experimental Test of a Microwave Ion Source," presented at the 30th International Symposium on Electron, Ion and Photon Beams, Boston, Massachusetts, May (1986).

9. Dahimene, D., and Asmussen, J., "The Performance of a Microwave Ion Source Immersed in a Multicusp Static Magnetic Field," Journal of Vacuum Science and Technology, B, 5, 126 (1986).

10. Asmussen, J., and Dahimene, D., "The Experimental Test of a Microwave Ion Source in Oxygen," Journal of Vacuum Science and Technology, B, 5, 328 (1987).

11. Dahimene, M., "Development of a Microwave Ion and Plasma Source Immersed in a Multicusp Electron Cyclotron Resonant Magnetic Field," Ph.D. Dissertation, Michigan State University (1987).

12. Asmussen, J., "Development of Microwave Plasma and Ion Beam Sources for Materials Processing," presented at the IEEE International Conference on Plasma Science, Pittsburgh, Pennsylvania, June (1985).

13. Hopwood, J., Dahimene, M., Reinhard, D.K., and Asmussen, J., "Plasma Etching with a Microwave Cavity Plasma Disk Source," Presented at the 31st International Symposium on Electron, Ion and Photon Beams, California, May (1987).

14. Hopwood, J., Reinhard, D. K., and Asmussen, J., "Experimental Conditions for Uniform Anisotropic Etching of Silicon with a Microwave Electron Cyclotron Resonance Plasma System," Journal of Vacuum Science and Technology, B, 6 (1988).

15. Dahimene, M., Mahoney, L., Hopwood, J., Salbert, J., Reinhard, D., and Asmussen, J., "Comparison of Experimental Measurements and Theoretical Modeling of Low Pressure Microwave Discharges," in IEEE 1987 International Conference on Plasma Science, Arlington, Virginia, IEEE, 5C4, 90 (1987).

16. Hopwood, J., Wagner R., Reinhard, D. K., Asmussen, J., "Characterization of a Multipolar Electron Cyclotron Resonance Plasma Source," to be presented at the IEEE 1989 International Conference on Plasma Science, Buffalo, New York, May (1989).

17. Mahoney, L., Dahimene, M., and Asmussen, J., "A Low Power, Compact, 2.5 cm, Efficient Microwave Ion Source," in IEEE 1987 International Conference on Plasma Science, Arlington, Virginia, IEEE, 6Y2, 122 (1987).

18. Mahoney, L., Engemann, J., and Asmussen, J., "Performance of an Efficient, Compact 3.2 cm. ECR Broadbeam Ion Source Operating with High and Low Acceleration Potentials," International Conference on ECR Ion Sources and Their Applications, National Superconducting Cyclotron Laboratory, Michigan State University, East Lansing, Michigan, NSCL Report #MSUCP-47, 101 (1987).

19. Mahoney, L., Dahimene, M., and Asmussen, J., "Low Power, 3.2-cm, Efficient Microwave Electron Cyclotron Resonant Ion Source," Review of Scientific Instruments, 59, 448 (1988).

20. Mahoney, L., and Asmussen, J., "A Compact and Low Power Microwave ECR Broad Ion Beam Source for Low-Pressure Materials Processing," to be presented at the IEEE 1989 International Conference on Plasma Science, Buffalo, New York, May (1989).

21. Salbert, G. T., Reinhard, D. K., Asmussen, J., "Down-stream Oxidation of Silicon Using an ECR Microwave Plasma Disk Reactor," to be presented at the IEEE 1989 International Conference on Plasma Science, Buffalo, New York, May (1989).

22. Mahoney, L., Asmussen, J., "A Compact, Resonant Cavity, Five Centimeter, Multicusp, ECR Broad Beam Ion Source," presented at the International Conference on Ion Sources, University of California at Berkeley, California, July (1989), Proceedings to be published in Review of Scientific Instruments, January (1990).

23. Asmussen, J., Fritz, R., Mahoney, L., Fournier, G., Demaggio, G., "ECR Ion and Free Radical Sources for MBE Applications," to be presented at the International Conference on Ion Sources, University of California at Berkeley, California, July (1989), Proceedings to be published in Review of Scientific Instruments, January (1990).

24. Asmussen, J., Hopwood, J., Sze, F. C., "A 915 MHz/2.45 GHz ECR Plasma Source for Large Area Ion Beam and Plasma Processing," to be presented at the International Conference on Ion Sources, University of California at Berkeley, California, July (1989), Proceedings to be published in Review of Scientific Instruments, January (1990).

25. Asmussen, J. "Electron Cyclotron Resonance Microwave Discharges for Etching and Thin Film Deposition," to be published in the Journal of Vacuum Science and Technology, B, 7 (1989).

26. Musil, J., "Microwave Plasma: Its Characteristics and Applications in Thin Film Technology," Vacuum, 36, 161 (1986).

27. Tokiguchi, K., Itoh, H., Sakudo, N., Koike, H., Saitoh, T., "Non-mass Analyzed Ion Implantation Using Microwave Ion Source," Vacuum, 36, 11 (1986).

28. Roppel, T., "Anodic Oxidation of Silicon in a Microwave Plasma Disk Reactor," Ph.D. Dissertation, Michigan State University (1986).

29. Roppel, T., Reinhard, D. K., Asmussen, J., "Low Temperature Oxidation of Silicon Using a Microwave Plasma Disk Source," Journal of Vacuum Science and Technology, B, 4, 295 (1986).

30. Rogers, J., "Properties of Steady-State, High Pressure Argon Discharges," Ph.D. Dissertation, Michigan State University (1982).

31. Mallavarpu, R., " An Investigation of the Electromagnetic Behavior of a Microwave Plasma Source Over a Wide Range of Pressures and Flow Rates," Ph.D. Dissertation, Michigan State University (1976).

32. Fredericks, R., "An Experimental and Theoretical Study of a Resonantly Sustained Plasma in Microwave Cavities," Ph.D. Dissertation, Michigan State University (1971).

33. Whitehair, S., "Experimental Development of a Microwave Electrothermal Thruster," Ph.D. Dissertation, Michigan State University (1986).

34. Atta, V., Vacuum Science and Engineering, McGraw-Hill, New York (1965).

35. Johnson, E. O., and Malter, L., "A Double Floating Probe Method for Measurements in GAs Discharges," Physical Review, 80, 58 (1950).

36. Chen, F.F., Plasma Diagnostic Techniques, R. H. Huddlestone and S.L. Leonard, eds., Academic Press, New York, 113 (1965).

37. Chapman, B., Glow Discharge Processes: Sputtering and Plasma Etching, John Wiley and Sons, New York (1980).

38. Bohm, D., The Characteristics of Electrical Discharges in Magnetic Fields, A. Guthrie and R. K. Watherling, eds., McGraw-Hill, New York, Ch. 3 (1949).

39. Hopwood, J., Private Communication, Michigan State University (1989).

40. Keller, M. H., "Si-Extraktionsopik für Filamentlose Ionenquellen," Masters Thesis, Bergische Universität, GH Wuppertal (1987).

41. Korzec, D., Schmitz, K., Engemann, J., "Extraction Performance of Dual Grid Ion-optics: Simulation and Experiment," Journal of Vacuum Science and Technology, B, 6 (1988).

42. Harrington, R. F, Time Harmonic Electromagnetic Fields, McGraw-Hill, New York (1961).

43. Kaufman, H. R., Cuomo, J. J., Harper, J. M. E., "Critical Review: Technology and Application of Broad-Beam Ion Sources Used in Sputtering; Part I. Ion Source Technology," Journal of Vacuum Science and Technology, 21, 764, (1982).

44. Kaufman, H. R., and Robinson, R. S., Operation of Broad Beam Ion Sources, Common Wealth Scientific Corporation, Alexandria, Virginia (1987).

45. Van Vechten, D., Hulder, G., Donovan, E., "Characterization of a 3-cm Kaufman Ion Source with Nitrogen Feed Gas," Vacuum, 36, 841 (1986).

46. Wilbur, P., O Daniels, L., "The Development and Applications of an Ion Implanter Based on Ion Thruster Technology," Vacuum, 36, 5 (1986).

47. Schottky, W. Phys. Z., 25, 635 (1924) as cited by (48)

48. Franklin, R. N., Plasma Phemonena in Gas Discharge, Clarendon Press, Oxford (1976).

49. Brown, S. C., Introduction to Electrical Discharges in Gases, John Wiley and Sons, New York (1966).

50. Cherrington, B. E., Gaseous Electronics and Gas Lasers, Pergamon Press, New York (1979).

51. Rapp, D., and Golden, P. E., "Total Cross Sections for Ionization and Attachment in Gases by Electron Impact," Journal of Chemical Physics, 43, 1464 (1965).

52. Tonks, L., Langmuir, I., Physics Review, 34, 876 (1929) as cited by (48).

53. Walther, S. R., Leung, K. N., and Kunkel, W. B., "Characteristics of a Compact Microwave Ion Source," Review of Scientific Instruments, 57, 1531 (1986).

54. Matsuoka, M., and Ono, K., " Low-energy Ion Extraction with Small Dispersion from a Electron Cyclotron Resonance Microwave Plasma Stream," Applied Physics Letters, 50, 1864 (1984).

55. Sakudo, N., Tokiguchi, K., Koike, H., Kanomata ,I., "Microwave Ion Source," Review of Scientific Instruments, 48, 762 (1977).

56. Geller, R., Gugliermotte, F., "Process and Apparatus for Producing Highly Charged Large Ions and an Application Utilizing This Process," U. S. Patent, No. 4,417,178, Nov. 22 (1983).

57. Ramo, S.,Whinnery, J., and Van Duzer, T., Fields and Waves in Communication Electronics, John Wiley and Sons, New York, Sec. ed. (1984).

58. Freeman, J. H., Defects in Crystalline Solids: Ion Implantation, S. Amelinckx, R. Gevers and J. Nihoul, eds., Northland Holland Publishing Company, Amsterdam, Ch. 4 (1973).

59. Robinson, R. S., Journal of Vacuum Science and Technology, 15, 277 (1978) as cited by (43).

60. Engemann, J., Private Communication, Michigan State University, (1988).

61. Forrester, A. T., Large Ion Beams: Fundamentals of Generation and Propagation, John Wiley and Sons, New York (1988).

62. Harper, J., Heibulm, J., Speidell, J., and Cuomo, J., "Ion Beam Oxidation," Journal of Applied Physics, 52, 4118 (1981).

63. Ryssel, H., and Glawischnig, H., eds., Ion Implantation Techniques, Springer-Verlag Berlin Heidelberg, Federal Republic of Germany (1981).

64. Ryssel, H., and Glawischnig, H., eds., Ion Implantation: Equipment and Techniques, Springer-Verlag Berlin Heidelberg, Federal Republic of Germany (1983).

65. Brown, I., ed., The Physics and Technology of Ion Sources, John Wiley and Sons, New York (1989).

66. Kaufman, H. R., Harper, J.M.E., Cuomo, J.J., "Developments in Broad-Beam, Ion-source Technology and Application," Journal of Vacuum Science and Technology, 21, 764 (1982).